

# Aerodynamic noise of thin airfoils in turbulent flows

a detailed experimental validation  
of semi-analytical methods

*Master thesis by:*

Jelle Bastiaan Will

## **Graduation committee:**

---

Prof. dr. ir. C.H. Venner

Dr. L.D. de Santana

Dr. ir. N.P. Kruyt

Prof. dr. ir. A. Hirschberg

Dr. ir. A.P. Berkhoff

Dr. D. Ragni

*27 January 2017*

*Enschede, the Netherlands*



# Abstract

Aeroacoustic noise is increasingly becoming part of daily life for many people in today's society. Consider for instance the increased usage of drones. Another example is the expansion of wind farms close to urban centers, to meet the ever growing demand for green energy sources. Additionally turbines, pumps, and even some general purpose household appliances produce aerodynamically generated noise. All these devices and products will become more and more integrated in our daily routines in the near future.

Therefore noise reduction will become a more integral part of the design process. Usually optimizing a design to minimize noise, whilst maintaining operational efficiency, requires extensive computational power due to the relatively small time and spacial scales involved in acoustics. Therefore development of semi-analytical tools for noise prediction that can give quick and reasonably accurate results is desirable. Such models based on the Amiet theory are under development but require experimental validation. The model investigated here is developed for airfoil leading edge noise generated due to a turbulent inflow.

In order to validate the model three types of experiments are performed using newly developed setups. First turbulence grids are constructed to generate the inflow turbulence. The grids constructed generate near isotropic turbulence which can be fully described using the theoretical models. The noise production of the grids has been limited in order to obtain a reasonable signal-to-noise ratio for acoustic measurement purposes.

The resulting flow field has been fully characterized using two experimental techniques: Constant Temperature Anemometry (CTA) and Particle Image Velocimetry (PIV). Two components (axial and transverse) of the velocity field are fully characterized in the measurement region in the anechoic chamber. This results in a full description of the turbulence properties in this region consisting of turbulence intensity, integral length scale, and spectra. The generated turbulence spectrum and correlation functions have been found to match excellently with the semi-theoretical von Kármán model.

PIV is used to verify the results and to check the isotropy of the two transverse directions. The turbulence intensity results match closely between PIV and CTA measurements, the calculated integral length scales differ by a consistent factor.

An experimental acoustic setup is also developed consisting of a microphone array and different types of thin-airfoils that can be mounted in the flow. All ten wing models have been tested for all grid and velocity configurations. Background noise is subtracted from the wing signals.

Comparison of the experimental and predicted results for straight and circular airfoils show a good match in intensity levels and spectra up to a frequency  $1\text{ kHz}$ . The directionality of the signal, as a function of the observer angle, was found to be accurately predicted also. Above  $1\text{ kHz}$  an increase in upstream intensity was found, it is suggested that this is the result of trailing edge noise.

The experimental setups and techniques developed over the course of this thesis can accurately validate noise generation for simple airfoil shapes. Also small variations in wing shape can be observed from the acoustic measurement signal. This is very promising since it allows for validation of more detailed analytical tools for more specific cases, thus allowing for further development of these prediction methods which can in the long run be used in product development.

## Acknowledgements

In engineering and science no one gets anything done on their own, this also applies in this case. Therefore there are a number of people I am truly indebted to, both for their assistance in this research and for their support throughout my academic career. In this part of the report I would like to thank them.

First off Dr. Leandro de Santana, for teaching me about acoustics and being patient with someone who was new to this field. You were always available for questions and meticulous in your answers. Your work was the basis of mine and was a great inspiration and aid during all stages of this work. You motivated and pushed me to try and do as much as possible in the limited time frame of this assignment. You are new to being a teacher, but are already doing a great job.

Second I would like thank to Prof. Kees Venner and Dr. Niels Kruyt. Our work together was always really enjoyable. Our project together was my first experience with experimental research. Here I found that I really enjoy doing this type of work, even when it gets tedious at times. During this project you continually pushed me to improve and strive for the best you can do, I really appreciated this.

Next the technical staff Herman Stobbe, Steven Wanrooij, and Wouter den Breeijen. I always enjoyed the time we spent together in the lab fixing problems and building stuff. I really appreciate getting to know all of you and the conversations we shared together during coffee breaks. Additionally the support you provided in making my experimental setups a reality, was essential in getting all this done in time.

I would also like to thank Prof. Harry Hoeijmakers. Your courses on aircraft and aerodynamics were the main motivation for me to switch to Mechanical Engineering. You truly inspired me and helped me find the thing I love doing. For this I can never thank you enough.

Finally my family and friends. Your love and support were a great aid to me and motivated me to push through the harder times. Thank you all so much for this.

# Contents

Abstract . . . . .	iii
Acknowledgements . . . . .	v
List of Tables . . . . .	viii
List of Figures . . . . .	ix
<b>1 Introduction</b>	<b>1</b>
1.1 Airfoil noise generation and predictive models . . . . .	1
1.2 Thesis objectives . . . . .	2
<b>2 Introduction to the Amiet theory: airfoil leading edge noise prediction</b>	<b>4</b>
2.1 Airfoil noise radiation . . . . .	4
2.2 Airfoil aeroacoustic transfer function . . . . .	9
<b>3 Experimental setups and techniques</b>	<b>12</b>
3.1 Experimental arrangement and facility . . . . .	12
3.2 Flat wings models . . . . .	14
3.3 Turbulence grid design . . . . .	16
3.4 Measurement techniques . . . . .	17
3.4.1 Constant temperature anemometry . . . . .	17
3.4.2 Particle Image Velocimetry . . . . .	23
3.4.3 Acoustics . . . . .	29
<b>4 Inflow turbulence characterization</b>	<b>33</b>
4.1 Homogeneity of the flow field . . . . .	33
4.1.1 Flow field measurements . . . . .	34
4.1.2 Leading edge measurements . . . . .	37
4.2 Integral length scales . . . . .	39
4.3 Turbulence spectra . . . . .	42
4.4 PIV results . . . . .	44
4.4.1 Turbulence intensity . . . . .	44
4.4.2 Integral length scale . . . . .	46
4.4.3 Velocity statistics - higher order moments . . . . .	47
4.4.4 Upstream influence of thin airfoil . . . . .	48
<b>5 Acoustic far-field experimental results</b>	<b>49</b>
5.1 Background noise levels . . . . .	49
5.2 Flat plate measurements . . . . .	50

5.2.1	Acoustic signals . . . . .	50
5.2.2	Signal-to-noise ratio . . . . .	53
5.2.3	Aeroacoustic scaling . . . . .	54
5.3	SPL comparison for different wing types . . . . .	56
<b>6</b>	<b>Comparison of the Amiet model and experimental results</b>	<b>59</b>
6.1	Intensity and spectral comparison . . . . .	59
6.1.1	Circular wing . . . . .	59
6.1.2	Straight wing . . . . .	61
6.2	Comparison of the directionality . . . . .	63
6.2.1	Circular wing . . . . .	63
6.2.2	Straight wing . . . . .	65
6.2.3	Additional configurations . . . . .	67
<b>7</b>	<b>Conclusion and recommendation</b>	<b>68</b>
7.1	Turbulence generation and characterization . . . . .	68
7.2	Acoustics measurements and validation of the Amiet model . . . . .	69
7.3	Recommendations . . . . .	70
<b>A</b>	<b>List of symbols</b>	<b>72</b>
<b>B</b>	<b>Experimental process</b>	<b>74</b>
B.1	Wind tunnel - frequency velocity diagram . . . . .	74
B.2	Unfiltered turbulence spectral measurements . . . . .	75
B.3	Microphone array positions . . . . .	75
<b>C</b>	<b>Optimization of the turbulence grid design</b>	<b>76</b>
C.1	Grid types and considerations . . . . .	76
C.2	Initial design and layout . . . . .	78
C.3	Frequency analysis of the grid . . . . .	79
C.3.1	Mechanical analysis . . . . .	79
C.3.2	Vortex shedding . . . . .	81
C.3.3	Results . . . . .	82
C.4	Testing of grid acoustic properties . . . . .	82
C.5	Optimizing grid design for acoustic properties . . . . .	82
<b>D</b>	<b>Measurement results CTA: turbulence measurements</b>	<b>90</b>
D.1	Velocity and Turbulence fields . . . . .	90
D.2	Leading edge turbulence characterization . . . . .	99
D.2.1	Velocity and turbulence intensities . . . . .	99
D.2.2	Turbulence spectra . . . . .	107
D.2.3	Turbulence length scales . . . . .	109
	<b>Bibliography</b>	<b>112</b>

# List of Tables

3.1	Wing parameters. . . . .	15
3.2	Grid parameters. . . . .	16
3.3	Mean flow angles found using the PIV vector field rotation algorithm. . . . .	28
4.1	Turbulence intensities, isotropy, and Taylor length scales of the different grids at the leading edge of the airfoils $x/c_w = -0.5$ . The values are the averaged quantities of the interrogation points located on the airfoil. . . . .	42
4.2	Differences between the turbulence intensity results of the CTA and PIV measurements. The differences are percentage points differences. . . . .	45
4.3	Factor difference in the integral length scale results of the CTA and PIV measurements. . . . .	47
4.4	Averaged results based on the PIV measurements. The location in x-direction is around the leading edge of the airfoil. . . . .	47
5.1	Difference between SPL for different wing models for the specified frequency bins. For circular and straight wings this is large minus small. The SPL's are averaged over all microphones, i.e. for all observer angles. These results are for grid 2, at 30 <i>m/s</i> . . . . .	58
A.1	List of all symbols and parameters used in this report. . . . .	73
C.1	Table detailing the different design parameters of the original grids. . . . .	78

# List of Figures

2.1	Schematic representation of the flat plate airfoil. The coordinate system and dimensions of the wing are depicted as well as the incoming flow. Location vectors are shown for both positions on the wing, sources $x_s$ , and for observer positions $x_o$ . . . . .	5
2.2	Incoming turbulence modeled as waves. . . . .	9
3.1	Schematic detailing the aeroacoustic wind tunnel at the University of Twente. . . . .	12
3.2	Overview of the setup in the anechoic chamber. . . . .	13
3.3	Parameters and shapes of the flat metal plate wings used in the experiments. . . . .	15
3.4	Square grid parameters. . . . .	16
3.5	The second generation of turbulence developed in order to maximize acoustic signal-to-noise ratio. The grids have a very high solidity, they are very open. . . . .	17
3.6	Measured voltages during hot-wire calibration (black crosses). Contour plots are shown for the fitted values of $\theta$ and $  \vec{u}  $ . . . . .	19
3.7	One set of fits made during hot-wire calibration for both the magnitude of the velocity vector and the angle of the flow. Top two are the fits in the low velocity domain, where few data points are available. The bottom two figures show the high velocity fits. . . . .	20
3.8	Hot-wire probe velocity decomposition during calibration and measurements. . . . .	21
3.9	Blue crosses indicate positions of 10 second measurements duration in the $y - z$ plane and the red circles those of 40 second measurements. . . . .	22
3.10	The Dantec 2D traverse system in front on the inlet nozzle of the wind tunnel. The traverse moves the hot-wire probe in between measurements according to a specified grid. . . . .	23
3.11	Schematic overview of the PIV system. Original: <a href="http://www.dlr.de/as/en/DesktopDefault.aspx/tabid-183/251_read-12796/gallery-1/gallery_read-Image.5.1574/">http://www.dlr.de/as/en/DesktopDefault.aspx/tabid-183/251_read-12796/gallery-1/gallery_read-Image.5.1574/</a> . . . . .	24
3.12	Left: PIV setup in the wind tunnel. Right: laser sheet around the angled straight wing. . . . .	25
3.13	Light scattering relative intensity of an oil particle ( $d_p = 1 \mu m$ ), incoming light $532 nm$ . Ref. [19] page 19. . . . .	25
3.14	Camera image angle and lens corrections applied to target photo. . . . .	27
3.15	Distribution of found flow angles for grid 1. (2x2) at 30 m/s and the corresponding normal distribution fit. . . . .	28

3.16	PIV applied to leading edge of the flat airfoil single image pair results. Incoming turbulence generated by grid 1 (2x2), mean flow velocity 31.7 <i>m/s</i> . Vector field shown is with mean flow velocity subtracted. . . . .	29
3.17	Top: Swept wing mounted in the clamps which are tightened using set screws. Bottom: Circular wing mounted on the prongs, bolts are used on the inside of the wing to attach it to the prongs. . . . .	31
4.1	Left: Three dimensional view of the normalized velocity in axial direction. Right: Normalized axial velocity in the plane of the leading edge. . . . .	34
4.2	Left: Three dimensional view of the velocity in transversal direction. Right: Transverse velocity in the plane of the leading edge. . . . .	35
4.3	Left: Three dimensional view of the turbulence intensity in axial direction. Right: Axial turbulence intensity in the plane of the leading edge. . . . .	35
4.4	Left: Three dimensional view of the turbulence intensity in transverse direction. Right: Transverse turbulence intensity in the plane of the leading edge. . . . .	36
4.5	Left: Three dimensional view of the turbulence isotropy. Right: Turbulence isotropy in the plain of the airfoil leading edge. . . . .	36
4.6	Left: Normalized axial velocity profile on LE. Right: Transverse velocity profile on LE. Top: Measurements for all flat wings. Bottom: Measurements for all circular wings: unbroken line is $d_w = 250\text{ mm}$ dashes is $d_w = 180\text{ mm}$ . Crosses and circles corresponds to measurement positions and duration given in section 3.4.1 and Fig. 3.9. . . . .	37
4.7	Top left: Turbulence intensity in axial direction on leading edge. Top right: Turbulence intensity in transverse direction on leading edge. Bottom: Turbulence isotropy on leading edge. . . . .	38
4.8	Axial and transverse autocorrelation measurement data fitted according to Kármán and Liepmann correlations. . . . .	40
4.9	The integral or Taylor length scale plotted for several transverse positions on the y-axis. Upwards pointing triangle indicates von Kármán's correlation was used and a downwards pointing triangle indicates the theoretical Liepmann relation was used to determine the length scale. . . . .	41
4.10	Normalized turbulence spectrum for turbulence grid 3 (4x4) at the three measurement velocities of 15, 30, and 45 <i>m/s</i> . . . . .	44
4.11	Normalized turbulence spectrum for turbulence grid 2 (3x3) at an approximate free stream velocity of 30 <i>m/s</i> . . . . .	44
4.12	Turbulence intensities in both directions obtained using the PIV data. Resolution in <i>z</i> -direction is approximately 4 <i>mm</i> . . . . .	45
4.13	integral length scales calculated using PIV for all three turbulence grids and all three free stream velocities. The data is plotted against the vertical transverse direction <i>z</i> . Both axial and transverse components of the length scale are plotted. . . . .	46
4.14	Probability density function for the velocity fill without the wing (solid line) and with the wing (dashed line). . . . .	48

5.1	Background noise produced by the wind tunnel. For all flow velocities and grid types. . . . .	50
5.2	Example of tonal noise produced by the circular wing of at a free stream velocity of 30 $m/s$ (background subtraction is applied). . . . .	51
5.3	Example of broadband noise produced by the circular airfoil of $d_w = 250\text{ mm}$ at a free stream velocity of 30 $m/s$ (background subtraction is applied). . . . .	51
5.4	Example of broadband noise produced by the straight airfoil of $s_w = 350\text{ mm}$ at a free stream velocity of 30 $m/s$ (background subtraction is applied). . . . .	52
5.5	Directionality of the leading edge noise produced by the circular airfoil $d_w = 250\text{ mm}$ . The sound pressure levels shown in radial direction are the average SPL's over the given frequency domain. Configuration: Grid 2, 30 $m/s$ . . . . .	53
5.6	Signal-to-noise ratio for circular airfoil $d_w = 250\text{ mm}$ . Configuration: Grid 2, 30 $m/s$ . . . . .	53
5.7	Signal-to-noise ratio for straight airfoil $d_w = 250\text{ mm}$ . Configuration: Grid 2, 30 $m/s$ . . . . .	54
5.8	Collapse of acoustic spectra when scaled according to sixth power law. For the microphone at an angle of $40.7^\circ$ . . . . .	55
5.9	Collapse of acoustic spectra when scaled according to sixth power law. For the microphone at an angle of $86.9^\circ$ . . . . .	55
5.10	Collapse of acoustic spectra when scaled according to sixth power law. For the microphone at an angle of $142.4^\circ$ . . . . .	55
5.11	Comparison of the SPL's of the circular (V.) and the straight wings (I, and II). . . . .	56
5.12	Comparison of the SPL's of the straight(I.) and the swept wings (III.).	57
5.13	Comparison of the SPL's of the straight (I.) and the varying chord wings (IV.). . . . .	57
6.1	Theoretical noise predictions compared with the corresponding experimental results for three observer positions. . . . .	60
6.2	Theoretical noise predictions compared with the corresponding experimental results for three observer positions. . . . .	60
6.3	Theoretical noise predictions compared with the corresponding experimental results for three observer positions. . . . .	61
6.4	Theoretical noise predictions compared with the corresponding experimental results for three observer positions. . . . .	62
6.5	Theoretical noise predictions compared with the corresponding experimental results for three observer positions. . . . .	62
6.6	Theoretical noise predictions compared with the corresponding experimental results for three observer positions. . . . .	63
6.7	Directionality results for the circular airfoil of $d_w = 250\text{ [mm]}$ grid 2 (3x3) at approximately 15 $[m/s]$ . . . . .	64
6.8	Directionality results for the circular airfoil of $d_w = 250\text{ [mm]}$ grid 2 (3x3) at approximately 30 $m/s$ . . . . .	64

6.9	Directionality results for the circular airfoil of $d_w = 250$ [mm] grid 2 (3x3) at approximately 45 m/s. . . . .	64
6.10	Directionality results for the straight airfoil of $s_w = 350$ [mm] grid 2 (3x3) at approximately 15 m/s. . . . .	65
6.11	Directionality results for the straight airfoil of $s_w = 350$ [mm] grid 2 (3x3) at approximately 30 m/s. . . . .	65
6.12	Directionality results for the straight airfoil of $s_w = 350$ [mm] grid 2 (3x3) at approximately 45 m/s. . . . .	66
6.13	Directionality results for the circular airfoil of $d_w = 180$ mm grid 2 (3x3) at approximately 45 m/s. . . . .	67
6.14	Directionality results for the straight airfoil of $s_w = 250$ mm grid 2 (3x3) at approximately 45 m/s. . . . .	67
7.1	Possible improvement in the experimental acoustic setup. . . . .	70
B.1	Settings of the wind tunnel and the corresponding free stream velocity measured using the Pitot tube in the designated position. This position is used in all experiments to set the wind tunnel to the desired velocity in order to maintain consistent results. . . . .	74
B.2	Example of high frequency oscillations of the turbulence spectra in x- and y-directions. These measurements are for grid 2 (3x3) at 45 m/s. For each spectral direction two positions in x-direction are plotted corresponding to the position of the leading edge and just behind the trailing edge. . . . .	75
B.3	The angle in degrees around the $y$ -axis starting from the negative $x$ -axis corresponding to the microphone numbers: . . . . .	75
C.1	Proposed contraction nozzle for generation of shear layer turbulence for flat wing designs. . . . .	83
C.2	Frequency of the grid: Eigenfrequencies (1,2, and 3) as a function of diameter and the vortex shedding frequencies as a function of diameter and free stream velocity. . . . .	84
C.3	Left: One of the turbulence grid being inserted into the slot in the wind tunnel section developed for interchangeable grids. Middle: Extension constructed to magnetically mount different serration profiles to the inlet nozzle. Right: The extension construction to extend the length of the inlet nozzle in order to direct grid noise down stream instead towards the microphones. . . . .	85
C.4	Two of the temporary experimental setups used in order to study the acoustic properties of the grid. . . . .	85
C.5	Noise generated by the first generation grids. . . . .	86
C.6	Noise produced by rod for various types of helical wires. . . . .	86
C.7	Noise produced by rod for various wire spacings. . . . .	87
C.8	Influence of the wires on the acoustic performance of the grid and the resulting signal to noise ratio. . . . .	87
C.9	Signal to noise ratio of the wooden grid of 2x2 rods. . . . .	88
C.10	Signal to noise ratio of the wooden grid of 3x3 rods. . . . .	88

C.11	Signal to noise ratio of the wooden grid of 4x4 rods. . . . .	89
C.12	Signal to noise ratio of the wooden grid of 5x5 rods. . . . .	89
D.1	Normalized flow velocity for the $x$ - and $y$ -directions in the plane located at the leading edge of the airfoils. . . . .	99
D.2	Top: Turbulence intensities in $x$ - and $y$ -directions. Bottom: Turbulence isotropy parameter. Results for the plane at the airfoils leading edge. . . . .	99
D.3	Normalized flow velocity for the $x$ - and $y$ -directions in the plane located behind the airfoil. . . . .	100
D.4	Top: Turbulence intensities in $x$ - and $y$ -directions. Bottom: Turbulence isotropy parameter. Results for the plane behind the airfoils. . .	100
D.5	Normalized flow velocity for the $x$ - and $y$ -directions in the plane located at the leading edge of the airfoils. . . . .	101
D.6	Top: Turbulence intensities in $x$ - and $y$ -directions. Bottom: Turbulence isotropy parameter. Results for the plane at the airfoils leading edge. . . . .	101
D.7	Normalized flow velocity for the $x$ - and $y$ -directions in the plane located behind the airfoil. . . . .	102
D.8	Top: Turbulence intensities in $x$ - and $y$ -directions. Bottom: Turbulence isotropy parameter. Results for the plane behind the airfoils. . .	102
D.9	Normalized flow velocity for the $x$ - and $y$ -directions in the plane located at the leading edge of the airfoils. . . . .	103
D.10	Top: Turbulence intensities in $x$ - and $y$ -directions. Bottom: Turbulence isotropy parameter. Results for the plane at the airfoils leading edge. . . . .	103
D.11	Normalized flow velocity for the $x$ - and $y$ -directions in the plane located behind the airfoil. . . . .	104
D.12	Top: Turbulence intensities in $x$ - and $y$ -directions. Bottom: Turbulence isotropy parameter. Results for the plane behind the airfoils. . .	104
D.13	Normalized flow velocity for the $x$ - and $y$ -directions in the plane located at the leading edge of the airfoils. . . . .	105
D.14	Top: Turbulence intensities in $x$ - and $y$ -directions. Bottom: Turbulence isotropy parameter. Results for the plane at the airfoils leading edge. . . . .	105
D.15	Normalized flow velocity for the $x$ - and $y$ -directions in the plane located behind the airfoil. . . . .	106
D.16	Top: Turbulence intensities in $x$ - and $y$ -directions. Bottom: Turbulence isotropy parameter. Results for the plane behind the airfoils. . .	106
D.17	Normalized turbulence spectrum for turbulence grid 1 (2x2) at the three measurement velocities of 15, 30, and 45 $m/s$ . . . . .	107
D.18	Normalized turbulence spectrum for turbulence grid 2 (3x3) at the three measurement velocities of 15, 30, and 45 $m/s$ . . . . .	108
D.19	Normalized turbulence spectrum for turbulence grid 3 (4x4) at the three measurement velocities of 15, 30, and 45 $m/s$ . . . . .	108

D.20	Turbulence autocorrelations in both axial and transversal directions. Axial: one in ten data points is plotted. Transversal: one in five is shown. . . . .	109
D.21	Axial and transverse autocorrelation measurement data fitted according to Kármán and Liepmann correlations. . . . .	109
D.22	Integral length scale results plotted for positions along the airfoils leading edge. Results obtained using the von Kármán model. . . . .	109
D.23	Normalized flow velocity for the $x$ - and $y$ -directions in the plane located behind the airfoil. . . . .	110
D.24	Axial and transverse autocorrelation measurement data fitted according to von Kármán and Liepmann correlations. . . . .	110
D.25	Integral length scale results plotted for positions along the airfoils leading edge. Results obtained using the von Kármán model. . . . .	110
D.26	Normalized flow velocity for the $x$ - and $y$ -directions in the plane located behind the airfoil. . . . .	111
D.27	Axial and transverse autocorrelation measurement data fitted according to von Karman and Liepmann correlations. . . . .	111
D.28	Integral length scale results plotted for positions along the airfoils leading edge. Results obtained using the von Kármán model. . . . .	111

# Chapter 1

## Introduction

### 1.1 Airfoil noise generation and predictive models

In today's society noise pollution is an ever growing issue. One of the growing contributions is coming from aeroacoustic noise. Airplanes, fans, cooling systems, drones, wind farms, pumps, and turbines all produce noise because of fluid interaction. Excessive exposure to environmental noise has been shown to have negative effect on mental and physical well being. Therefore addressing these issues appropriately is a major issue in modern engineering. In this thesis I focus on aeroacoustic noise produced by a turbulent inflow interacting with solid wing shaped (thin) structures.

From a fluid dynamics objective acoustic noise production is an energy dissipating mechanism. If a fluid containing some degree of turbulence passes by an object, for instance an airfoil, it produces oscillating pressure differences at its surface. These pressure differences propagate as waves and radiate outwards into the far-field where they reduce in intensity. Finally this energy is to be converted into thermal energy by viscosity. Acoustic noise production thus removes energy from the flow and transmits it into the far-field where it dissipates. The energy lost in this way, which will be experienced as drag in the case of an airfoil, is completely negligible in comparison to other sources of drag.

However we humans experience these pressure waves as acoustic signals which we can hear when the frequency is in our audible range. This is very irritating, and a real nuisance when people live near, for instance, airports or wind farms. Therefore reducing the noise has become an important aspect in the design of airfoils and other objects exposed to fluid flows.

The study of aerodynamic noise is relatively new since until around mid 20<sup>th</sup> century there was no use for it. But with the invention of faster aircraft and wind turbines it became increasingly important. In this period the method for analytical prediction of leading edge noise started to develop. The method used in this thesis is based on the Amiet theory Refs. [2], [3], and [17]. The phenomenon of leading edge can be predicted using this method for thin airfoils.

A second mechanism of noise production, trailing edge noise, is also observed and

can coexist with leading edge noise. It was found that for larger turbulence intensity the pressure fluctuations in the boundary layer, causing trailing edge noise, will be small compared to those caused by inflow turbulence. Thus leading edge noise becomes the main source of aeroacoustic noise.

Currently there are very strict guidelines both national and globally pertaining to the noise allowed close to residential areas. Therefore it becomes more and more important to be able to make prediction during the design phase.

In applications where noise is a serious issue, CFD is currently often the only viable solution other than full scale tests. Because the time and spacial scales for acoustic waves are so small when compared to the flow field around an arbitrary body the required numerical model to solve this system gets very large. Therefore simulation times and cost are not something to invest in during the preliminary stages of the design.

This is exactly the type of problem that can be solved using semi-analytical models. These models are not designed to obtain exact results, but to provide an indication whether or not change to a design will significantly affect the produced noise. The computation times should be reduced from days or weeks to merely hours using these approaches.

The prediction methods however have a long way to go in their development. Only recently a resurgence of interest has been observed. To make advances in these prediction algorithms the models need to be verified.

## 1.2 Thesis objectives

The goal of this thesis is to experimentally validate semi-analytical methods for leading edge noise prediction. These noise prediction schemes are founded in theory and therefore require validation by experimental means. In order to realize this, experiments must be designed and constructed. Initially this will be done for simple airfoil shapes in order to check the setup and corroborate the noise predictions with the experimental results. However the data obtained for this setup can be used in follow up experiments for more complex cases, thus laying the groundwork for further experimental research and validation of more complex schemes.

The first step is to adapt the current setup in the Twente Wind Tunnel to produce a turbulent inflow. This turbulent inflow needs to be suited for producing leading edge noise whilst remaining quiet enough for acoustic measurements. Additionally the flow field and its characteristics must be determined in order to be able to make noise predictions. Experimental techniques and setups must be designed and constructed to realize this.

The next step is obtaining the experimental acoustics results. Also for this an experimental setup, including wing models, must be designed and constructed. The acoustic intensity produced by the setup and its directionality must be measured and recorded. These results can then be compared to the analytical solutions in order to judge how well the experimental setup performs.

The report starts off with an introduction to the analytical model, Ch. 2, in order to familiarize the reader with the concepts involved and what parameters are important in the predictive model and what is required to do the validation. Next in Ch. 3 the experimental methods and setups used in this thesis are explained. The following chapter, Ch. 4, deals with the characterization of the inflow turbulence, followed by an interpretation and analysis of the acoustic measurement results in Ch. 5. Finally in Ch. 6 the acoustic results are compared with the noise predictions made using the semi-analytical techniques. In Ch. 7 conclusions are drawn up based on the results and the process. Also recommendations are provided regarding improvements to the setup and the experimental techniques.

A list of symbols is attached in appendix A for the readers convenience.

# Chapter 2

## Introduction to the Amiet theory: airfoil leading edge noise prediction

Consider the case of a flat plate exposed to an incoming turbulent flow. This plate can be considered a simplified airfoil with a very small thickness and no camber, and will from here on out be designated as an airfoil. The free vortical motion in the inflow will be affected by the airfoil, creating small pressure fluctuations at the surface, as the air is stretched and squeezed. These fluctuations radiate outwards as an effect we perceive as noise.

The noise prediction method discussed in the current work, based on the Amiet theory, is designed to model this phenomenon and should predict the intensity and directionality of the noise thus produced. In this chapter a short overview of the method will be provided in order to familiarize the reader with the concepts involved, the requirements to make these predictions, and the experiments that need to be performed to validate the theory. In the first section the theory behind the noise radiation model and its derivation is provided. The second part explains the equation that needs to be solved and the boundary conditions involved when obtaining the aeroacoustic transfer function for a specific wing shape.

This chapter just gives an introduction to these aspects since they are not the main focus of this research. The full theoretical derivations and extensions are detailed in the work of L.D. de Santana Ref. [11]. This work provides a full derivation of the equations involved and the mathematical background to solve the system. The techniques detailed there are applied for the predictions made in this thesis.

### 2.1 Airfoil noise radiation

The theoretical model by Amiet considers an infinitely thin airfoil. The span ( $s_w$ ) of this airfoil is designated as  $2a_w$ , and its chord ( $c_w$ ) is characterized by  $2b_w$ . The center of the coordinate system is placed at the center of the wing, thus the tips are located at  $y = \pm a_w$  and the leading and trailing edge at  $x = \pm b_w$ . The  $x$ -direction on the coordinate system is parallel to the main flow direction. This is shown in Fig. 2.1.

The incoming flow is considered to be in the plane of the airfoil as is shown in the figure. This flow is considered to be turbulent because this will be the main source of leading edge noise. The turbulent inflow can be decomposed into

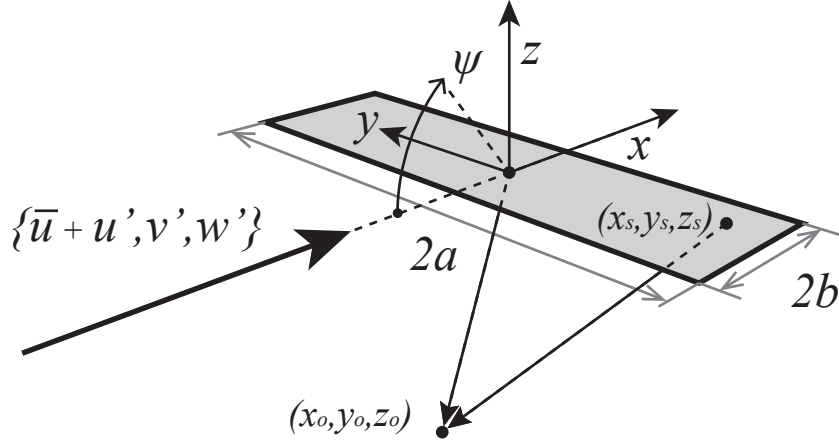


Figure 2.1: Schematic representation of the flat plate airfoil. The coordinate system and dimensions of the wing are depicted as well as the incoming flow. Location vectors are shown for both positions on the wing, sources  $x_s$ , and for observer positions  $x_o$ .

a main, time averaged component  $\{\bar{u}, 0, 0\}^T$  and fluctuating (perturbation) component  $\{u', v', w'\}^T$ . The main flow component is also referred to as  $U_\infty$ . The velocity perturbations are assumed to be small in comparison to the primary flow component:  $\sqrt{u'^2 + v'^2 + w'^2} \ll U_\infty$ . In the Amiet theory it is assumed that the noise generated by the flow interacting with the airfoil can be modeled by dipole type sources. According to N. Curle's analogy [10] the acoustic pressure for a dipole can be expressed as:

$$p(\vec{x}_o, \omega, \vec{x}_s) = \frac{ik\vec{x}_t \cdot \hat{\mathbf{F}}(\vec{x}_s, \omega)}{4\pi\sigma_s^2} e^{-ik\sigma_t} \left(1 + \frac{1}{ik\sigma_s}\right) \quad (2.1)$$

In this equation  $\hat{\mathbf{F}}$  is the surface forcing vector generating the dipole as a function of the frequency. The hat over this term indicates a temporal Fourier transform according to:

$$\hat{f}(\omega) = \frac{1}{2\pi} \int_{-\infty}^{\infty} f(t) e^{-i\omega t} dt$$

Since the airfoil is considered infinitely thin and only the pressure perpendicular to the airfoil will result in noise production, the forcing vector  $\hat{\mathbf{F}}(x_s, \omega)$  can be replaced by the local lift component  $\hat{l}(x_s, \omega)$  and  $\vec{x}_t$  is replaced by  $z$ . The following definitions apply:

- $\vec{x}_o = \{x_o, y_o, z_o\}$  is the vector containing the coordinates of the observer, in experiments this is the microphone.
- $\vec{x}_s = \{x_s, y_s, z_s\}$  vector indicating positions on the airfoil surface.
- $\vec{x}_t = \{((x_o - x_s) - M\sigma_s)/\beta^2, y_o - y_s, z\}$  the relative position vector between the source and the observer corrected for compressibility effects.

- $\sigma_s = \sqrt{(x_o - x_s)^2 + \beta^2 [(y_o - y_s)^2 + (z_o - z_s)^2]}$  the distance between source and observer considering compressibility.
- $\sigma_t = (\sigma_s - M(x_o - x_s)) / \beta^2$  wave propagation distance.

The term in brackets in Eq. 2.1 contains  $1/(ik\sigma_s)$ , this corresponds to the near-field effects of the dipole and will become negligible for increasing  $\sigma_s$  in the far-field. When considering distances one order of magnitude of the acoustic wavelength away this term will become negligible.

Because we are interested in the the noise produced over the entire wing we can assume these dipoles to be continuously distributed over its surface. Time resolved solutions are not of interest since the turbulence passing the wing is stochastic in nature. The power of this method lies in its statistical prediction of aeroacoustic noise. This is represented by a Power Spectral Density (PSD) function for the acoustic Sound Pressure Level (SPL):

$$S_{pp}(\vec{x}_o, \omega) = \lim_{T \rightarrow +\infty} \left\{ \frac{\pi}{T} \text{E} [p(\vec{x}_o, \omega, \vec{x}_s) p^*(\vec{x}_o, \omega, \vec{x}_s)] \right\} \quad (2.2)$$

Here E represents the expected value operator and the star indicates the complex conjugate for the complex acoustic pressure radiated by the dipole. Substituting in these dipole solutions 2.1 we obtain:

$$S_{pp}(\vec{x}_o, \omega) = \int_S \int_{S'} \left( \frac{kz}{4\pi} \right)^2 \frac{1}{\sigma_s^2 \sigma_s'^2} \left( 1 + \frac{1}{ik\sigma_s} \right) \left( 1 + \frac{1}{ik\sigma_s'} \right)^* S_{ll}(\vec{x}_s, \vec{x}_s', \omega) e^{-ik(\sigma_t - \sigma_t')} dS dS' \quad (2.3)$$

Here  $S_{ll}$  is the cross power spectral density of the lift fluctuation function and is defined as:

$$S_{ll}(\vec{x}_s, \vec{x}_s', \omega) = \lim_{T \rightarrow +\infty} \left\{ \frac{\pi}{T} \text{E} \left[ \hat{l}(x_o, y_o, \omega) \hat{l}^*(x'_o, y'_o, \omega) \right] \right\} \quad (2.4)$$

The term  $\hat{l}$  is directly related to the pressure jump induced by the airfoil. We can consider the incoming turbulence as incoming pressure waves with different wave numbers. These waves will be related to the gust velocity in the direction perpendicular to the airfoils surface. Mathematically these gusts are expressed as:

$$w(\vec{x}_s, t) = \hat{w}(k_x, k_y) e^{i(k_x(U_\infty t - x_s) - k_y y_s)} \quad (2.5)$$

The double hat  $\hat{w}$  indicates a double spacial Fourier transform of the incident perturbation velocity. Using Eq. 2.5 we can express the the pressure jump as:

$$\tilde{l}(\vec{x}_s, \omega) = 2\pi\rho U_\infty \hat{w}(k_x, k_y) g(\vec{x}_s, k_x, k_y) e^{i(k_x U_\infty t - k_y y_s)} \quad (2.6)$$

Where  $g$  is a transfer function between the spectral power of the turbulence and the spectral intensity of the sound generated by the airfoil shape. This transfer function will be discussed in the next section 2.2.

By integrating Eq. 2.6 over all wave numbers in both directions the contributions of

all gusts is obtained. This is the local lift in the time domain:

$$l(\vec{x}_s) = 2\pi\rho U_\infty \int_{-\infty}^{\infty} \int_{-\infty}^{\infty} \hat{w}(k_x, k_y) g(\vec{x}_s, k_x, k_y) e^{i(k_x U_\infty t - k_y y_s)} dk_x dk_y \quad (2.7)$$

Applying the Fourier transforms to equation 2.7 in order to convert it to the frequency domain:

$$\hat{l}(\vec{x}_s, \omega) = 2\pi\rho \int_{-\infty}^{\infty} \int_{-\infty}^{\infty} \hat{w}(k_x, k_y) g(\vec{x}_s, k_x, k_y) e^{-ik_y y_s} \left( \frac{U}{2\pi} \int_{-\infty}^{\infty} e^{i(k_x U_\infty - \omega)t} dt \right) dk_x dk_y \quad (2.8)$$

The term in parenthesis is the Fourier transform of the Dirac delta function. Applying its properties to perform the integration on equation 2.8 the local lift density can be expressed as:

$$\hat{l}(\vec{x}_s, \omega) = 2\pi\rho \int_{-\infty}^{\infty} \hat{w}(k_x, k_y) g(\vec{x}_s, K_x, k_y) e^{-k_y y_s} dk_y \quad (2.9)$$

Where  $K_x$  is the chordwise wave number defined as  $K_x = \omega/U$ . This relation describes the local lift density.

To obtain the statistical representation the cross power spectral density formulation of Eq. 2.4 is used:

$$S_{ll}(\vec{x}_s, \vec{x}'_s, \omega) = (2\pi\rho)^2 \int_{-\infty}^{\infty} \int_{-\infty}^{\infty} \hat{w}(K_x, k_y) \hat{w}^*(K_x, k_y) g(\vec{x}_s, K_x, k_y) g^*(\vec{x}'_s, K_x, k_y) dk_y dk'_y \quad (2.10)$$

Following the procedure by R.K. Amiet [1] and [2] we make the assumption that the incoming turbulence field is isotropic in nature i.e. invariant under rotations and reflections. Making use of the isotropy assumption the statistical orthogonality of the turbulence wave vectors can be expressed as follows:

$$\hat{w}(K_x, k_y) \hat{w}^*(K_x, k_y) = U_\infty \delta(k_y - k'_y) \Phi_{ww}(K_x, k_y) \quad (2.11)$$

In this equation  $\Phi_{ww}$  is the turbulence spectrum in the direction perpendicular to the wings surface. Eq. 2.11 makes it possible to rewrite Eq. 2.10 to:

$$S_{ll}(\vec{x}_s, \vec{x}'_s, \omega) = (2\pi\rho)^2 U_\infty \int_{-\infty}^{\infty} \int_{-\infty}^{\infty} \Phi_{ww}(K_x, k_y) e^{-ik_y(y_s - y'_s)} g(\vec{x}_s, K_x, k_y) g^*(\vec{x}'_s, K_x, k_y) dk_y \quad (2.12)$$

Now an expression for  $S_{ll}$  is obtained, this relation can be substituted into Eq. 2.3. In this way we obtain an expression for the PSD of the noise radiated by the airfoil:

$$S_{pp}(\vec{x}_o, \omega) = \int_{S_y} \int_{S'_y} \left( \frac{\rho k z}{s} \right)^2 U_\infty \frac{1}{\sigma_s^2 \sigma'_s} \left( 1 + \frac{1}{ik\sigma_s} \right) \left( 1 + \frac{1}{ik\sigma'_s} \right)^* e^{-ik(\sigma_t - \sigma'_t)} \int_{-\infty}^{\infty} \Phi_{ww}(K_x, k_y) e^{-ik_y(y_s - y'_s)} g(\vec{x}_s, K_x, k_y) g^*(\vec{x}_s, K_x, k_y) dk_y dS_y dS'_y \quad (2.13)$$

By using two assumptions this equation can be significantly reduced in complexity. The first assumption is that the observers are placed in the *acoustic far-field*, this implies that the observers are far removed from the source of the noise generations. Mathematically it means that the distance  $|\vec{x}_t|$  is much larger than the acoustic wavelength  $\lambda$ : i.e.  $|\vec{x}_t| \gg \lambda$ . Due to this assumption the terms  $(1/ik\sigma_s)$  drop out. The second assumption is called the *geometric far-field* assumption. This assumption is valid if the observer is located far away with respect to the airfoil span i.e.  $|\vec{x}_t| \gg s_w$ . This assumption results in the simplification that:  $(y_o - y_s) \approx y_o$ . and by extension:

$$\frac{1}{\sigma_s^2} \approx \frac{1}{\sigma_o^2} \quad (2.14)$$

$\sigma_o$  Is introduced when applying the acoustic far-field assumption and is defined as:  $\sigma_o^2 = x_o^2 + \beta^2(y_o^2 + z_o^2)$

By applying these assumptions to Eq.2.13 the following simplified formulation is obtained:

$$S_{pp}(\vec{x}_o, \omega) = \left( \frac{\rho k z b_w}{\sigma_o^2} \right)^2 \pi U_\infty a_w \Phi_{ww}(K_x, K_y) |\mathcal{L}(\vec{x}_o, K_x, K_y)|^2 \quad (2.15)$$

Where  $\mathcal{L}$  is the complete aeroacoustic transfer function, the combination of the  $g$  terms.

This simplified relation will be used for the calculation of all theoretical results in the present work. It contains three distinct contributions:

- A number of geometry, frequency, and flow dependent constants are found on the left of the equation.
- $\Phi_{ww}$  Contains the information on the turbulence spectrum interacting with the flat plate airfoil.
- $\mathcal{L}$  The aeroacoustic transfer function related to wing geometry, this converts the turbulence energy into acoustic energy which is radiated outwards.

To validate this model we need to be able to compute all the terms in Eq. 2.15. The sound pressure levels on the left hand side are obtained by doing acoustic measurements on airfoils in the flow presented in Ch. 5. In order to predict these values using the Amiet model the right hand side terms are required. The constant terms are easily obtained. To obtain the term  $\Phi_{ww}$  a reconstruction of the inflow turbulence in the wind tunnel is required. Therefore experimental characterization of the flow field and turbulence spectra is necessary, which is performed in Ch. 4. The final

term ( $\mathcal{L}$ ) is the acoustic transfer function which is determined semi-analytically, the process for which is described in the next section.

## 2.2 Airfoil aeroacoustic transfer function

In order to obtain solutions based on the model derived in the previous section we need to find expressions for the aeroacoustic transfer function  $\mathcal{L}(\vec{x}_o, K_x, k_y)$ . This function is based on the source distribution given by the transfer function  $g(\vec{x}_o, k_x, k_y)$ . The method used to obtain these functions will be briefly discussed here. The full approach is provided in appendix A of the work by de Santana [11]. By considering the problem as envisioned by Amiet we have a wing subjected to an incoming wave as is depicted in Fig.2.2. Two component of the wave will interact with the flat surface of the wing, making it possible to mathematically model the incoming wave as:  $(U_\infty \cos(\theta), U_\infty \sin(\theta), 0)$ . This is the model for a skewed velocity for a single frequency. Because a thin airfoil is considered at no (or a small) angle of attack the lift dipole is assumed to be much larger than the drag dipole. Therefore only the incident gusts perpendicular to the airfoil are considered in the far-field noise generation.

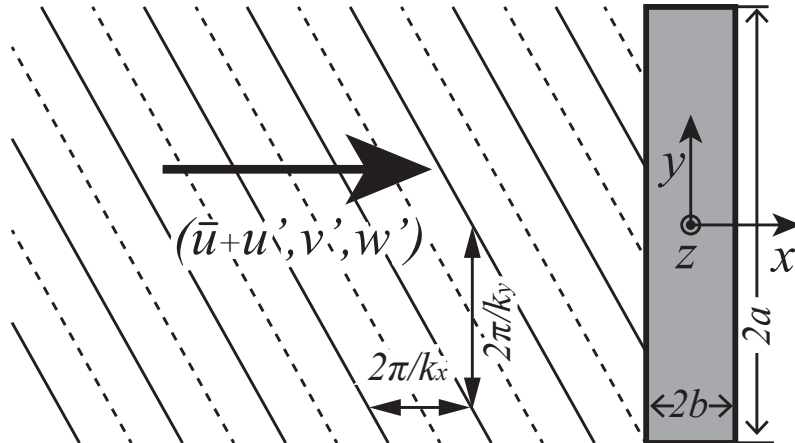


Figure 2.2: Incoming turbulence modeled as waves.

To solve this system linear compressible potential flow is assumed. The velocity potential is defined based on the fluctuation potential obtained from the equations of small disturbances Chu and Kovásznyai [7]. Because the solutions in potential flow are linear, the solutions for different boundary conditions and wavenumbers can be superimposed, resulting in a solution for the full problem. Potential flow theory assumes an irrotational inviscid flow, which appears strange since it is used to model a turbulent flow. However by considering multiple wavenumbers and adding the solutions an approximation of the full turbulence spectrum can be achieved.

The potential function  $\Psi$  is derived on the basis of the fluctuating flow component  $\vec{u}'$  close to the airfoil surface, i.e. the scattered component. Using this potential function the Amiet problem is solved by applying the following boundary conditions as employed by Amiet [3]:

- $\Psi(x, 0, t) = 0$  at  $x/b \leq -1$  - Zero fluctuating potential upstream of the airfoil.
- $\frac{\partial \Psi(x, 0, t)}{\partial z} = -w$  at  $-1 < x/b \leq 1$  - Normal velocity on airfoil surface must be equal to zero because of the normal surface condition. Therefore the fluctuating potential must compensate for the the incoming gust function  $w$ .
- $\frac{D\Psi(x, 0, t)}{Dt} = 0$  at  $x/b > 1$  - Zero pressure jump at the airfoil trailing edge and downstream of the wing, i.e. the Kutta condition.

Where the total derivative operator is defined as:

$$\frac{D}{Dt} = \frac{\partial}{\partial t} + U_\infty \frac{\partial}{\partial \bar{x}} \quad (2.16)$$

By assuming the main flow component to be directed in the  $x$ - $y$  plane, i.e. no time averaged flow component normal to the airfoil surface, the scattered potential flow model simplifies to:

$$\left[ \nabla^2 - \frac{1}{c_0^2} \frac{D^2}{Dt^2} \right] \Psi(x, y, t) = 0 \quad (2.17)$$

By assuming the velocity potential to be a harmonic function and applying a Fourier transform in the span direction along the wing we obtain:

$$\Psi(x, y, z, t) = \phi(x, z) e^{i\gamma x} e^{-ik_y y} e^{i\omega t} \quad (2.18)$$

Where  $\gamma = kM/\beta^2$ . Substituting this relation into Eq. 2.17:

$$\beta^2 \frac{\partial^2 \phi}{\partial x^2} + \left( \frac{k^2}{\beta^2} - k_y^2 \right) \phi + \frac{\partial^2 \phi}{\partial z^2} = 0 \quad (2.19)$$

Using the following definitions to make the Cartesian coordinates dimensionless:

$$\bar{x} = \frac{x}{b}, \quad \bar{y} = \frac{\beta y}{b}, \quad \bar{z} = \frac{\beta z}{b} \quad (2.20)$$

Adopting the following wavenumber definitions:

$$k_x = \frac{\omega}{U_\infty}, \quad k = \frac{\omega}{c_0} = k_x M, \quad \bar{k}_i = k_i b \quad (2.21)$$

Using both these sets of definitions Eq. 2.19 reverts to a canonical Helmholtz equation of the form:

$$\frac{\partial^2 \phi}{\partial \bar{x}^2} + \frac{\partial^2 \phi}{\partial \bar{z}^2} + \kappa^2 \phi = 0 \quad (2.22)$$

where:

$$\kappa^2 = \mu^2 - \frac{\bar{k}_y}{\beta^2}, \quad \mu = \frac{\bar{k}_x M}{\beta^2} \quad (2.23)$$

The transformed boundary conditions for this problem are:

$$\phi(\bar{x}, 0) = 0 \quad \bar{x} \leq -1 \quad (2.24)$$

$$\frac{\partial}{\partial \bar{z}} \phi(\bar{x}, 0) - \frac{-w_0 b}{\beta} e^{-i\bar{k}_x / \beta^2 \bar{x}} \quad -1 < \bar{x} \leq 1 \quad (2.25)$$

$$\left( i \frac{\bar{k}}{\beta^2} + \frac{\partial}{\partial \bar{x}} \right) \phi(\bar{x}, 0) \quad \bar{x} > 1 \quad (2.26)$$

The character of this partial differential system depends on the value of  $\kappa^2$ :

- if  $\kappa^2 > 0$ , i.e.  $\bar{k}_y < \frac{\bar{k}_x^2 M^2}{\beta^2}$ , than the Helmholtz equation is hyperbolic and will behave like a wave equation. The incoming gusts are in this case called supercritical.
- if  $\kappa^2 < 0$ , i.e.  $\bar{k}_y > \frac{\bar{k}_x^2 M^2}{\beta^2}$ , than the Helmholtz equation is elliptic and will behave like Poisson's equation. The incoming gusts are in this case called subcritical.
- if  $\kappa^2 = 0$ , i.e.  $\bar{k}_y = \frac{\bar{k}_x^2 M^2}{\beta^2}$ , than the Helmholtz equation is elliptic and will behave like Laplace's equation. The incoming gusts are in this case called critical.

Solving these equations for the sub- and supercritical case, satisfying all boundary conditions, allows for the computation of the aeroacoustic transfer functions of the wing. The method employed to solve the system relies on the Schwarzschild theorem [23] and will not be covered in this work. For an extensive treatise on this again is referred to the work of L.D. de Santana [11].

This approach is valid for non-compact airfoils. The work of S.W. Rienstra and A. Hirschberg [20] section 2.2.3 defines a compact acoustic source based on its Helmholtz number ( $He$ ). A source or region is said to be compact when:  $He \ll 1$ . The Helmholtz number is defined as:

$$He = \frac{2\pi f}{c_0} = \frac{2\pi c_w}{\lambda} \quad (2.27)$$

In the present work the Helmholtz number at  $f = 100 \text{ Hz}$  is approximately equal to 0.11, which is small but the assumption is still viable.

# Chapter 3

## Experimental setups and techniques

### 3.1 Experimental arrangement and facility

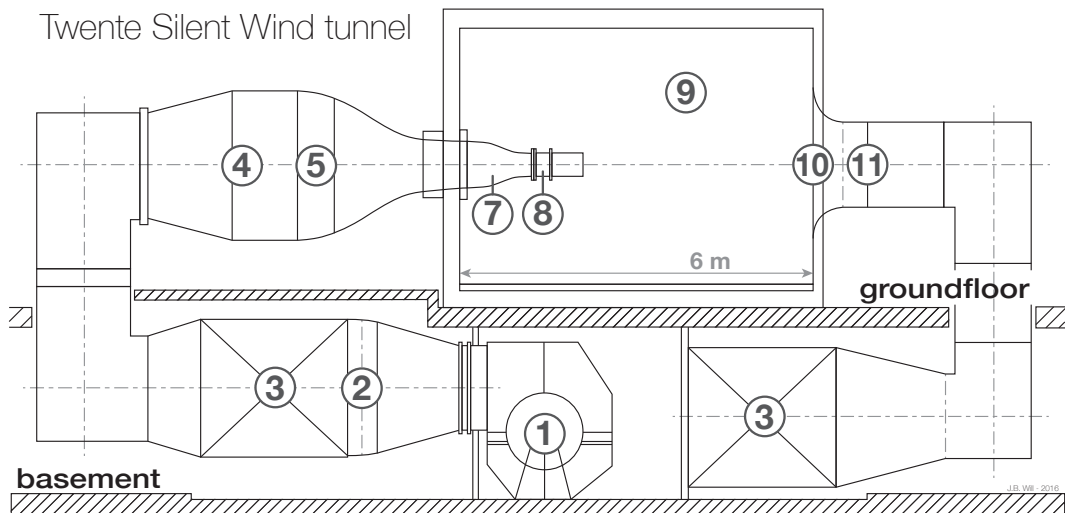


Figure 3.1: Schematic detailing the aeroacoustic wind tunnel at the University of Twente.

All experiments and tests were performed in the Twente Wind Tunnel at the University of Twente in Enschede, the Netherlands. A schematic layout of the facility is shown in Fig. 3.1. The facility is a low noise, laminar, open-jet, closed-circuit wind tunnel. The system is powered by a 130 kW electrical engine connected to two large radial turbines indicated in the figure by (1). The temperature can be manually regulated using a valve connected to a water cooled heat exchanger (2). Propagation of noise generated by the turbines and the tubes of the heat exchanger to the measurement area is minimized by acoustic dampening panels (3) placed up- and downstream. Upstream of the measurement section the flow is made laminar by passing through a settling chamber (4) and a number of anti-turbulence grids

⑤). The air passes through two contractions ⑦ to reach the desired velocity range and outlet size. The flow is made turbulent by interchangeable turbulence grids ⑧ and exits the nozzle into the anechoic room ⑨ where measurements are performed in the open jet. The air is then collected ⑩ and a closed system is formed. The collector also has acoustic dampening material installed ⑪ in order to reduce the acoustic reflections and noise generated at the corner vanes.

The open measurement section of the wind tunnel is located inside of a large anechoic chamber ⑨ specifically designed for aeroacoustic measurements. Models placed inside the jet generate noise which propagates throughout the chamber into the quiescent region in which microphones can be placed for acoustic measurements. The walls of the chamber are a modern type of acoustic material made of metal perforated plates with close behind them acoustic foam. This provides an anechoic test environment for broadband noise of a frequency of approximately 200 Hz and higher. Shear layer effects on the acoustic signal will be neglected in the interpretation of the acoustic signals. In Fig. 3.2 the experimental setup for all acoustic measurements is

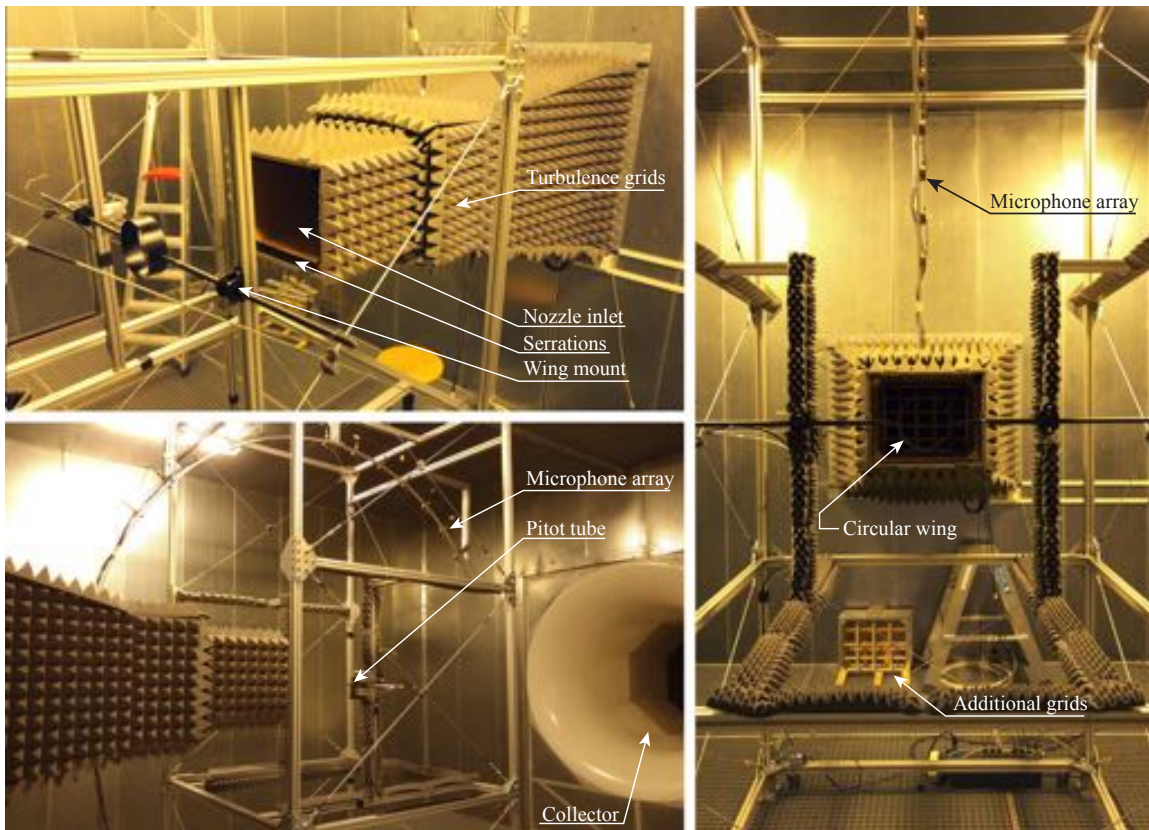


Figure 3.2: Overview of the setup in the anechoic chamber.

depicted. We can see the inlet nozzle, through which the flow enters the chamber. The dimensions of the opening are  $351\text{ mm}$  height and  $450\text{ mm}$  width. The corners have triangular pieces in them in order to make the flow more uniform. The nozzle edge allows serrations to be magnetically attached. These serrations are to prevent acoustic feedback from the wing to induce a vortex shedding mode at the nozzle lip as was documented by M. Roger [22]. This phenomenon caused tonal noise which

contaminated the acoustic signal from the wing. Leading to bad signal-to-noise ratio for this frequency range. In the present work this phenomenon was not encountered during any of the experiments. The serrations however were always in present during measurements since no negative effects were observed.

The nozzle was also covered with a double layer of acoustic foam. This was done to prevent vibroacoustic noise from the contraction and the grids affecting the measurements and also to prevent any reflection of noise this large uncovered surface might cause. Portions of the frame in which the wings are mounted were also covered to prevent reflections in the direction of the microphone array.

The distance from the turbulence grids to the leading edge of the wing was kept at  $1.2\text{ m}$  for all experiments. In case of swept wings or wings with a varying chord this is the mean distance to the leading edge. The edge of the inlet to the turbulence grids is  $0.7\text{ m}$  to shield the microphones from the direct noise generated by the grids.

## 3.2 Flat wings models

In the experiments all wing are flat plates with a negligible thickness. Four different types of wing are used, shown in Fig. 3.3, additionally one parameter of each type is varied to study its effects. Wing types I and II are straight flat wings, III are swept wings, IV are wings with a varying chord length, and V are circular wings.

Wings I, III, and IV all have a span of  $350\text{ mm}$  and a thickness of  $2\text{ mm}$ . Wing II is different in this regard, it has a span of only  $250\text{ mm}$  and a thickness of  $1\text{ mm}$ . Reduction of the span allows to check for effects from the shear layer from the nozzle inlet hitting the edges of the wings.

The wings of type III have a swept profile, i.e. the leading edge is angled with respect to the plane normal to the free stream direction. This is indicated in the figure and the angle is designated as  $\delta$ . Three wings were produced with  $\delta = 2^\circ, 4^\circ$ , and  $6.56^\circ$ .

The same angles are also used for wing type IV; the wings with varying chord. Here both the leading and trailing edge have the same angles only with a different sign. A additional parameter is introduced here: the initial, i.e. the smallest, chord length of the wing. This parameter  $e$  is respectively  $50\text{ mm}$ ,  $40\text{ mm}$ , and  $40\text{ mm}$  for increasing values of  $\delta$ .

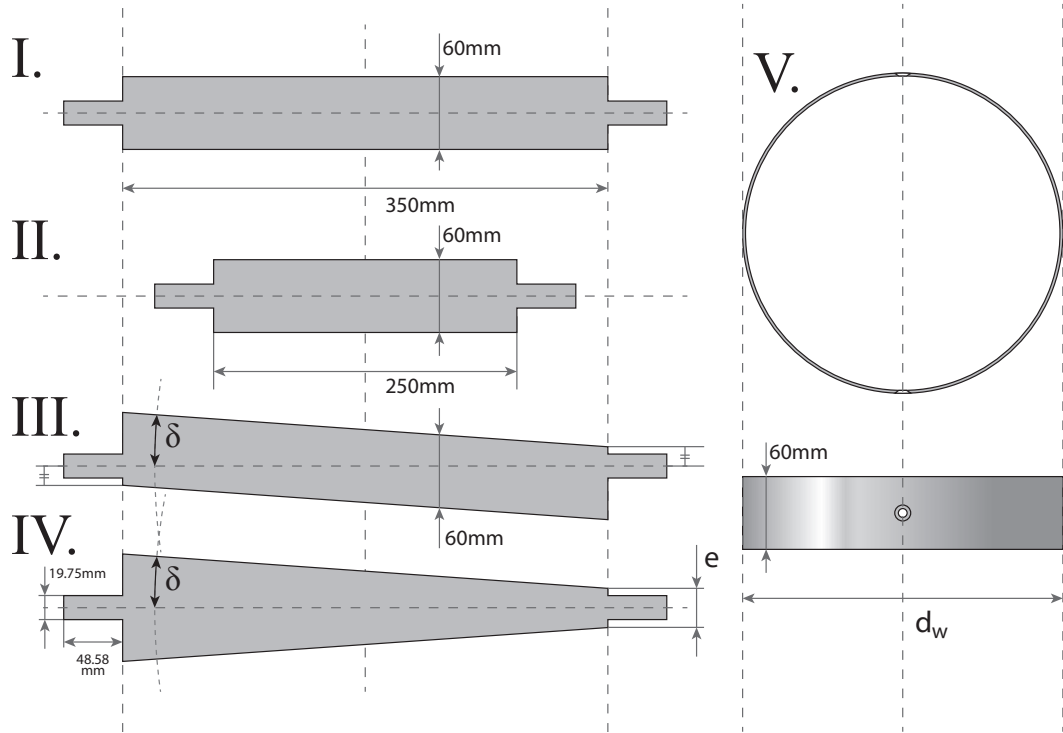


Figure 3.3: Parameters and shapes of the flat metal plate wings used in the experiments.

Wing type:	Chord $c_w$ [mm]	Span $s_w$ [mm]	Thickness $t_w$ [mm]	In. Chord $e$ [mm]	Sweep $\delta$ [°]	Diameter $d_w$ [mm]
straight	60	350	2	-	0	-
	60	250	1	-	0	-
swept	60	350	2	-	2	-
	60	350	2	-	4	-
	60	350	2	-	6.56	-
var. chord	62.2	350	2	50	2	-
	64.5	350	2	40	4	-
	80.2	350	2	40	6.56	-
circ. wing	60	-	2	-	0	180
	60	-	2	-	0	250

Table 3.1: Wing parameters.

### 3.3 Turbulence grid design

The wind tunnel at the University of Twente is a silent and low turbulence intensity facility. For measurements on leading edge airfoil noise a turbulent flow is, however, a prerequisite. Therefore the inlet into the anechoic testing chamber must be modified to obtain a homogeneous isotropic outflow. The full design process is discussed in appendix C.

It was decided to generate the turbulence using passive grids. The main advantage being the low complexity. The downsides are that the turbulence is hard to regulate and the fact that the turbulent energy is extracted from the flow, causing the velocity to drop. To combat this final problem a contraction was used in front of the grids. A wind tunnel section was designed and built that could house interchangeable grids, this is shown in Fig.C.3.

The grids themselves are characterized by means of the spacing between the rods ( $M_h, M_v$ ), the rod diameter  $d_r$  and the solidity of the grid  $\sigma^*$  which is defined as the ratio of "open" to total cross sectional area. The parameters are shown in Fig. 3.4. Initial designs for the grids were based on the turbulence characteristics and grids. Grids of a low solidity were developed using aluminum rods, in order to produce turbulence as close as possible to theoretical turbulence. However this turned out to be unworkable from an acoustics perspective. Therefore a second generation of grids was built and tested based on designs used by R.W. Paterson and R.K. Amiet Ref. [17] and L.D. de Santana Ref. [11].

The resulting grids are shown in Fig.3.5. Comparatively these grids are much more open, and have a solidity of  $\sigma^* > 0.5$  which is not ideal for the produced turbulence but worked very well for noise production based on initial testing. This process is fully described in appendix C. The grid parameters are given in Tab. 3.2. The dimensions of the rods used in these grids are  $16.3 \text{ mm}$  in axial and  $20.5 \text{ mm}$  in transverse direction.

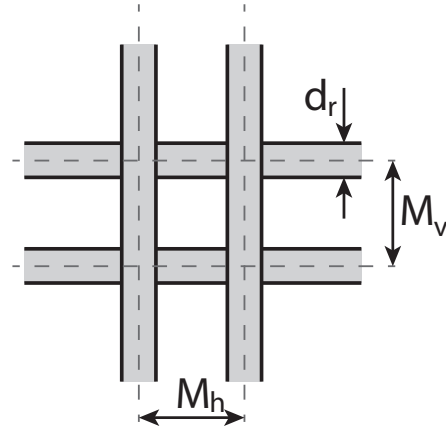


Figure 3.4: Square grid parameters.

Grid no.	Rod diameter $d_r$ [mm]	Mesh spacing $M_h$ [mm]	Mesh spacing $M_v$ [mm]	Solidity $\sigma^*$ [-]
1. (2x2)	20.5	150	117.9	0.7986
2. (3x3)	20.5	112.5	87.8	0.7061
3. (4x4)	20.5	90	70.2	0.6190

Table 3.2: Grid parameters.

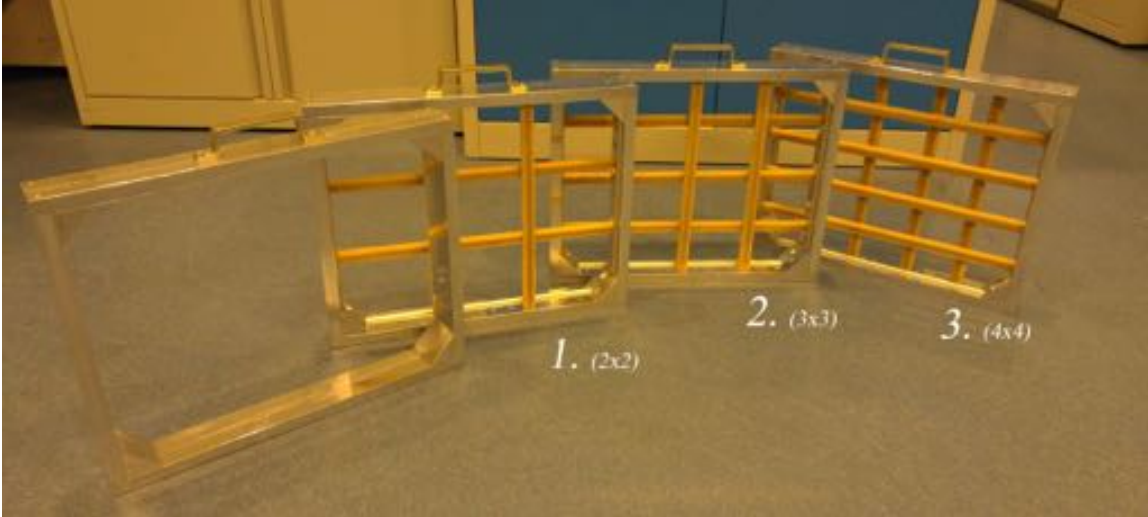


Figure 3.5: The second generation of turbulence developed in order to maximize acoustic signal-to-noise ratio. The grids have a very high solidity, they are very open.

## 3.4 Measurement techniques

### 3.4.1 Constant temperature anemometry

In order to obtain a high resolution model of the flow field near the inlet nozzle (the location of the thin-airfoil), Constant-Temperature (hot-wire) Anemometry (CTA) has been employed. This technique is based on the (convective) heat transfer from an infinitesimally thin wire ( $5 \mu m$ ). The assumption is that the heat transfer is purely a function of the temperature difference ( $\Delta T$ ) between the wire and the surrounding fluid, and the liquids flow speed  $||\vec{u}||$ .

The instrumentation used is a *Dantec Streamline 90N10 frame* and a two-wire probe (55P51) for synchronous two velocity component measurements. The streamline frame system consists of two channels each of which has a Wheatstone bridge. The system was operated in constant temperature mode, since this results in the shortest system response times (See Ref. [6] *section 2.3.3.*). Therefore the bridge balances the applied voltage to the wire with respect to a set overheat ratio and reference state, effectively keeping the average wire temperature constant. Thus based on the voltage applied an instantaneous velocity can be obtained. The frequency resolution of this technique extends beyond  $10^5 Hz$ , which is well beyond the desired frequency range for acoustic purposes.

#### Temperature correction

A temperature correction has been employed to compensate for swings in the ambient temperature induced by operation of the wind tunnel. The method employed is a first order method which is commonly used when temperature swings between calibration and measurement do not exceed approximately two to three Kelvin in either direction. This method assumes the flow properties to remain constant and only corrects for the

direct difference in ambient temperature. See Ref. [6] *section 7.2.3*, on the method applied. The relation relating the wire-voltages is given as follows:

$$E_w = E_{w,r} \left[ \frac{T_w - T_r}{T_w - T_a} \right]^{1/2} \quad (3.1)$$

Where  $E_{w,r}$  is the value read using the system and  $E_w$  the corrected value. Also  $T_w$  is the set wire temperature,  $T_a$  is the current ambient temperature, and finally  $T_{a,r}$  is the reference temperature set during the initialization of the probe. This correction is applied to both the calibration data and the measurements.

The temperatures used in the correction scheme is obtained by synchronous measurements with the CTA measurements. The temperature probe corresponding to the Streamline system of Dantec was placed in the corner of the nozzle in order to obtain an accurate reading of the free stream temperature. It should be noted that this temperature can differ significantly from that of the stationary air in the anechoic chamber. Therefore all measurements in the shear layer (mixing layer) should be regarded as inaccurate with an additional inaccuracy factor of 2%. This corresponds to the maximum correction factor encountered based on temperature differences between room and free stream.

### Calibration procedure

At the start of the measurements the hot-wire setup was calibrated according to the following procedure. The hot-wire was placed at the center of the upper quadrant of the outlet closest to the opening. A Pitot-tube connected to the frame was placed in the lower left quadrant. For this tube a polynomial fit was used based on the specifications provided by the supplier. Simultaneous measurements on both devices were performed at ten logarithmically scaled velocities ( $U_\infty = \{3, 4.2, 5.9, 8.3, 11.4, 15.8, 21.7, 29.6, 40.4, 55\}$  *m/s*) and at fifteen angles ranging from  $-35^\circ$  to  $35^\circ$  in  $5^\circ$  increments. The lower velocity limit was decided because of the limits of the Pitot-tube.

It is assumed, and corroborated by later experiments, that the flow in these measurement points is both homogeneous and directed in exclusively axial direction: thus the measured velocity is equal to  $||\vec{u}||$ . In addition five measurements are made for zero velocity, which corresponds to the case of purely natural convection.

The measured Voltages  $E_1$ , and  $E_2$  of the respective wires can now be plotted against both the angle and the magnitude of the velocity vector. This is shown in Fig. 3.6 as the black crosses. Bruun Ref. [6] describes a number of methods that can be used to analyze data based on the calibration measurements. In this case it was decided to use a fourth order polynomial surface fit to fit the data to both angle ( $\theta$ ), and velocity  $U_\infty$ . These fits are shown at the bottom in Fig. 3.7. They are made excluding the zero velocity measurements and give very good results. For  $||\vec{u}||$  r-squared norm gives  $\approx 0.9996$  and a rmse of  $\approx 0.36$  *m/s*. For  $\theta$  the r-square norm is  $\approx 0.9997$  and the rmse is  $\approx 0.41$  [°]. The error in the velocity is mainly attributed to the range around 29.6 *m/s*. Here it was found the wind tunnel operates at either a higher or a lower velocity. The fitted contours are also plotted in Fig. 3.6, this

phenomenon is clearly visible here.

In addition to the normal fit a fit for low velocities was made based on the measurements at  $U_\infty = 3 \text{ m/s}$  and the zero velocity measurements. These are shown in the top portion of Fig. 3.7. It should be noted that the fit for theta was not used since the slope in  $\theta$  for  $U_\infty \rightarrow 0$  is undefined and the “torsion” is better approximated by the normal fit. For the velocities this was successfully implemented and resulted in elimination of negative velocities. It should be noted that for the present work this range of the measurement data is of at best secondary importance. The region exhibiting these velocities is well outside of the boundary layer and with that outside the area of interest. Therefore no attempt was made to make a smooth fit between the high- and low-velocity fits.

The system was always operated in the high accuracy mode where the voltage range is limited to  $0 - 5 \text{ V}$ , this results in 8 significant digits in the voltage signal. During calibration the device is set to make maximum use of this range, leaving around  $0.5 \text{ V}$  unused as margins. i.e  $0.5 \text{ V}$  corresponds to zero velocity and  $4.5 \text{ V}$  gives  $55 \text{ m/s}$ . Thus using  $4 \text{ Volt}$  as the range of the system corresponding to a velocity shift of  $55 \text{ m/s}$ . This range has  $3 \cdot 10^7$  discrete digital values. Thus giving us a theoretical velocity resolution of  $\approx 2 \cdot 10^{-6} \text{ m/s}$  and a similar quantization error, which is completely negligible in comparison to other system errors.

### High frequency response

In order to capture transient phenomenon the response time of the CTA system is another important factor, this becomes relevant for determining the turbulence spectra and integral length scales. A square-wave response test is performed on the hot-wire in order to check the response time and stability of the system. It was found that for the normal wire settings the systems response time was in the order of  $f_r \approx 1 \text{ kHz}$ , which is very low. By increasing amplifier gain and tuning the amplifier filter it was possible to obtain a system response of around  $f_r \approx 10 \text{ kHz}$ . Increasing the settings beyond this resulted in undesirable high frequency oscillations in the feedback system.

It was found during analysis of the data that there is still some instability beyond this frequency, causing oscillations in the output data far below the Nyquist frequency ( $f_n = 51 \text{ kHz}$ ) and the analog low-pass filter ( $f_{lp} = 30 \text{ kHz}$ ). They begin to influence the results beyond  $f \approx 10 \text{ kHz}$ , however they do not contaminate the signal at lower

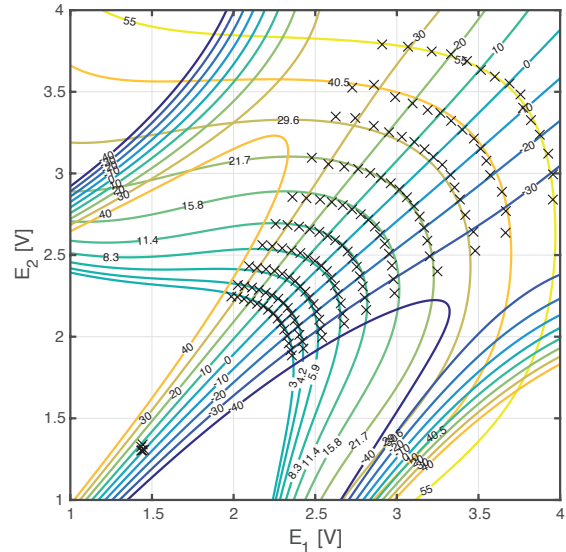


Figure 3.6: Measured voltages during hot-wire calibration (black crosses). Contour plots are shown for the fitted values of  $\theta$  and  $||\vec{u}||$ .

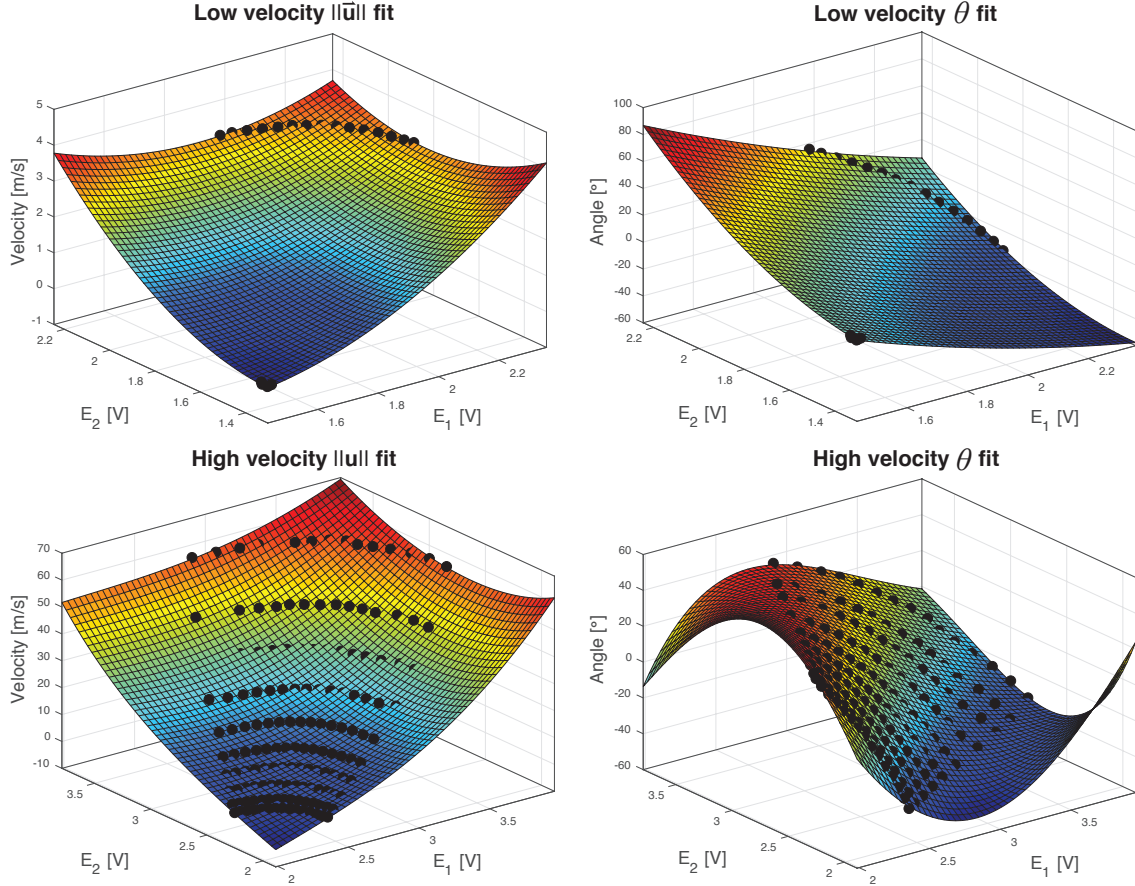


Figure 3.7: One set of fits made during hot-wire calibration for both the magnitude of the velocity vector and the angle of the flow. Top two are the fits in the low velocity domain, where few data points are available. The bottom two figures show the high velocity fits.

frequencies because they are actual fluctuations in the data signal. Therefore we can simply apply a digital low-pass filter and filter out this region, which is required to determine the integral length scale.

This procedure obviously results in a large portion of the turbulence spectrum containing the smaller eddies. However these losses are negligible in terms of their energy content, so the statistical properties such as flow velocity, and turbulence intensity will remain unaffected. However from this data we are no longer able to determine things like the Kolmogorov length scale, at which the inertial range of the energy cascade stops and viscous dissipation becomes dominant. For the purposes of this report this will not affect the results since this range of the turbulence spectrum will not affect the input parameters for the noise prediction model.

### Velocity decomposition

The probe is geometrically aligned with the main flow direction. Based on later flow measurements in the main channel this is confirmed to be within  $0.5^\circ$  for all grids and velocities. This gives a deviation of the order  $10^{-2} m/s$  to both velocities. Therefore

the velocity field in all measurements can simply be decomposed in a flow component parallel to the probe and a transversal one and will be a good approximation of the  $u$  and  $v$  velocities in the theoretical flow field. These velocity components are shown in the bottom part of Fig. 3.8.

During calibration the probe is rotated with respect to the main flow angle as is

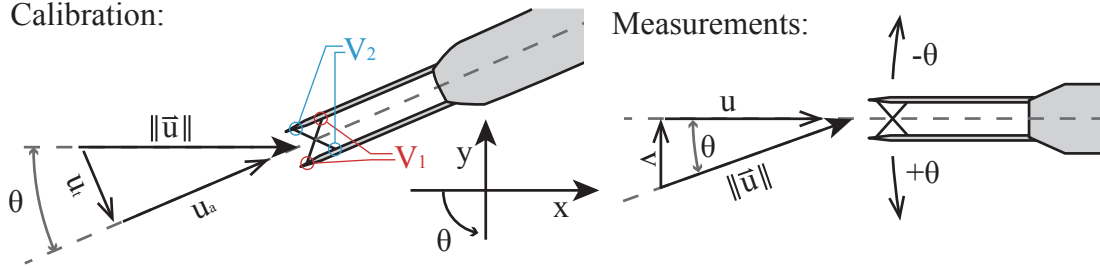


Figure 3.8: Hot-wire probe velocity decomposition during calibration and measurements.

shown in the top of Fig. 3.8. This results in the  $V$ - $\theta$  calibration map. Based on the definitions in the figure we obtain the axial ( $u$ ) and transverse ( $v$ ) flow components according to:

$$u(\vec{x}, t) = U_{\infty}(\vec{x}, t) \cos(\theta(\vec{x}, t)) \quad (3.2)$$

$$v(\vec{x}, t) = -U_{\infty}(\vec{x}, t) \sin(\theta(\vec{x}, t)) \quad (3.3)$$

### Flow characterization procedure

In order to characterize the flow field in front of the inlet nozzle point measurements are performed using the hot-wire probe. The positioning of the probe is accomplished using a high-accuracy ( $\ll 1 \text{ mm}$ ) traverse system from Dantec. Using this system it is possible to scan the area in front of the nozzle in four planes in the  $x$ -direction, resulting in cross sections of the flow field and all of its derivative parameters. The experimental setup is depicted in Fig. 3.10. The purpose of these measurements is to get statistics on the flow field and testing uniformity and isotropy in order to determine the ideal location of the airfoils.

The area scanned in this way is the outlet size  $450 \text{ mm} \times 350 \text{ mm}$  plus a  $5 \text{ mm}$  offset in all directions in order to capture the shear layers indicated by the blue line in the figure. In this area the spacial resolution of the measurement points was  $25 \text{ mm}$  in both  $y$ - and  $z$ - directions. For each point the timing is as follows: I) probe moves to target position. II) probe is waiting for three second to stop vibrations due to movement. III) probe reads signal for 2 seconds. IV) Probe start moving. This procedure is repeated for all points in the grid. It was noted that when the traverse system moves in horizontal direction vibrations are worse due to the added mass of the vertical arm moving also. Therefore the grid is scanned vertically making sure the worst vibrations of the rig are confined to the outer edges of the top and bottom shear layers.

The relatively short measurement duration was found to give enough statistics to determine both local mean velocities and local mean turbulence intensities. There was no signal drift over the durations of these measurements. This was also corroborated by the longer CTA measurements, which gave identical results for both parameters. Here a sampling frequency of  $25600\text{ Hz}$  was chosen with a low-pass filter at  $10\text{ kHz}$ . Additionally longer duration measurements were also performed in order to determine the spectral characteristics of the turbulence. Two sets of these measurements were performed, the duration of these measurements lasted 10 and 40 seconds respectively. Both were analyzed using the same algorithms and no significant differences in results were found.

Resulting in the conclusion that 10 seconds is enough of a sample time to capture the turbulence spectra. The x-positions of these measurements are in the exact position of the leading edge ( $x/c_w = -0.5$ ) of the airfoil and slightly behind the trailing edge location ( $x/c_w = -2.83$ ). In the  $y - z$  plane the leading edge of the airfoil is followed for both the straight wing and the circular wing. This is depicted in Fig. 3.9. The red and blue points (corresponding to the different measurement durations) were carried out on different days, the results being identical therefore lends credence to the assumed consistency of the measurements. This consistency is shown in appendix D.2 where the results for all measurement positions are plotted in the same figure.

The measurement procedure for the second set is identical to the one discussed previously. The differences are limited to the investigation points entered into the traverse grid, the measurement durations, and the sampling frequency being increased to  $102\text{ kHz}$  with a low-pass filter at  $30\text{ kHz}$ . (note that the choice of analog low-pass filter was limited because of the hardware).

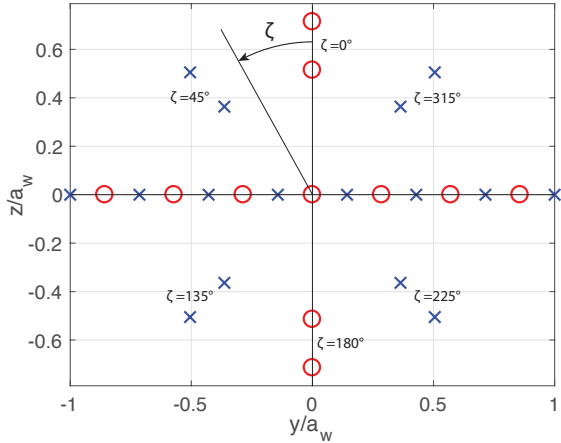


Figure 3.9: Blue crosses indicate positions of 10 second measurements duration in the  $y - z$  plane and the red circles those of 40 second measurements.

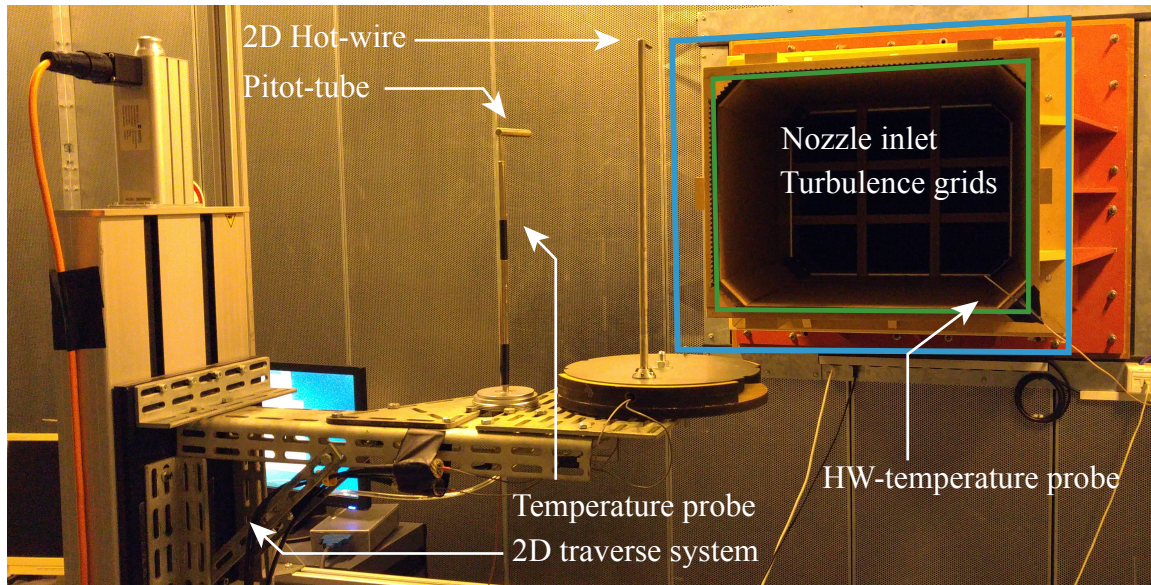


Figure 3.10: The Dantec 2D traverse system in front on the inlet nozzle of the wind tunnel. The traverse moves the hot-wire probe in between measurements according to a specified grid.

### 3.4.2 Particle Image Velocimetry

In addition to the CTA measurements also PIV measurements are performed on the turbulent flow field to corroborate the results from the CTA measurements. A secondary objective is to confirm the isotropy of the transverse components of the turbulence spectrum. In the CTA measurements it was always the  $y$ -component that was observed, using PIV we can easily measure the  $z$ -component.

PIV is near non-intrusive method of measuring flow fields. The developed experimental setup is shown in Fig. 3.12. For those readers unfamiliar with the technique a short description will be provided here. As can be observed the system consists of three main components. Particles, a light source (laser), and a camera. The particles are released into the flow. Since the wind tunnel is a closed system they will circulate for approximately 30 minutes before dissipating. The laser light is converted into a plane or sheet using sheet optics and directed towards the flow as is illustrated in Fig. 3.11. The light from the laser illuminates the particles which scatter the light. This light can, because of the high intensity of the laser, be picked up by the camera. By doing this with two laser pulses with a very small  $dt$  the particles in both photos will have moved only a few pixels. Using a two-dimensional autocorrelation function the mean flow velocity between two sections of the photos can be calculated, thus obtaining a vector field based on the image pairs.

The experimental setup and processing is based on the book *Particle Image Velocimetry - a practical guide* Ref. [19], this work provides an extensive introduction and theoretical background as well as a guide for the experimental process.

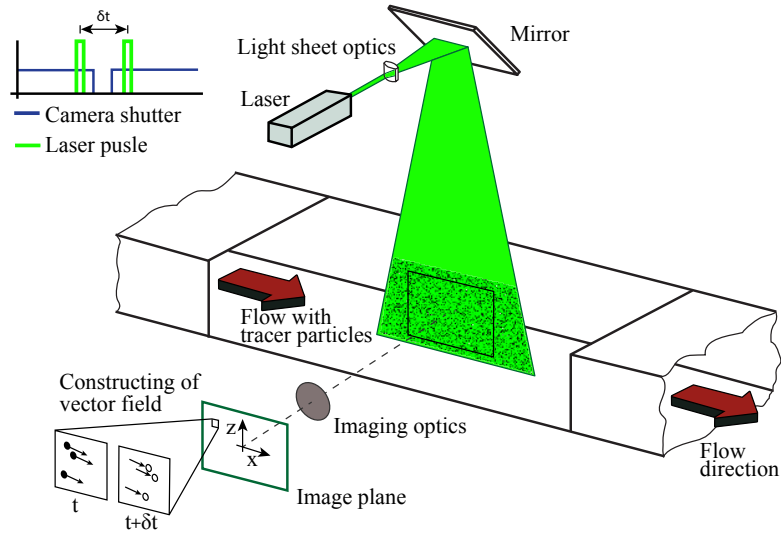


Figure 3.11: Schematic overview of the PIV system. Edited version of image from DLR. (Reference in figure list.)

## Experimental setup

The setup in the wind tunnel is as shown in Fig. 3.12. Particles are being generated using a *PIVTEC PIVpart45* seeder. Using a hose the particles are injected into the free stream and are circulated in the closed wind tunnel. The particles are small oil (Di-Ethyl-Hexyl-Sebacat) spheres with a average diameter of  $0.9\mu m$ . A measurement area is chosen and a target is mounted at this location to focus the high-speed camera on. The target is a board with a known pattern on it, as seen in Fig. 3.14. The laser system used to illuminate the particles is a *Litron Nano 135-15 PIV* laser. This is a dual cavity laser allowing for high intensity, close spaced pulses. The camera used is a *Phantom v611* capable of matching the  $15Hz$  of the laser and its minimum inter frame time (" $\delta t$ " in Fig. 3.11). Here inter frame times between  $50$  and  $150\mu s$  were used, depending on the flow velocity in order to obtain particle displacements of approximation 8 pixels.

The laser and camera timing is crucial. Both are connected to a Programmable Timing Unit (PTU) which allows for synchronous operation of both systems. The PTU is connected to a desktop computer running *LaVision - DaVis* software which is designed for PIV purposes allowing the user to control operations of most parameters in the system. This system has a terminal both inside and outside of the anechoic chamber of the tunnel, allowing for alignment and trouble shooting from inside and running experiments from outside.

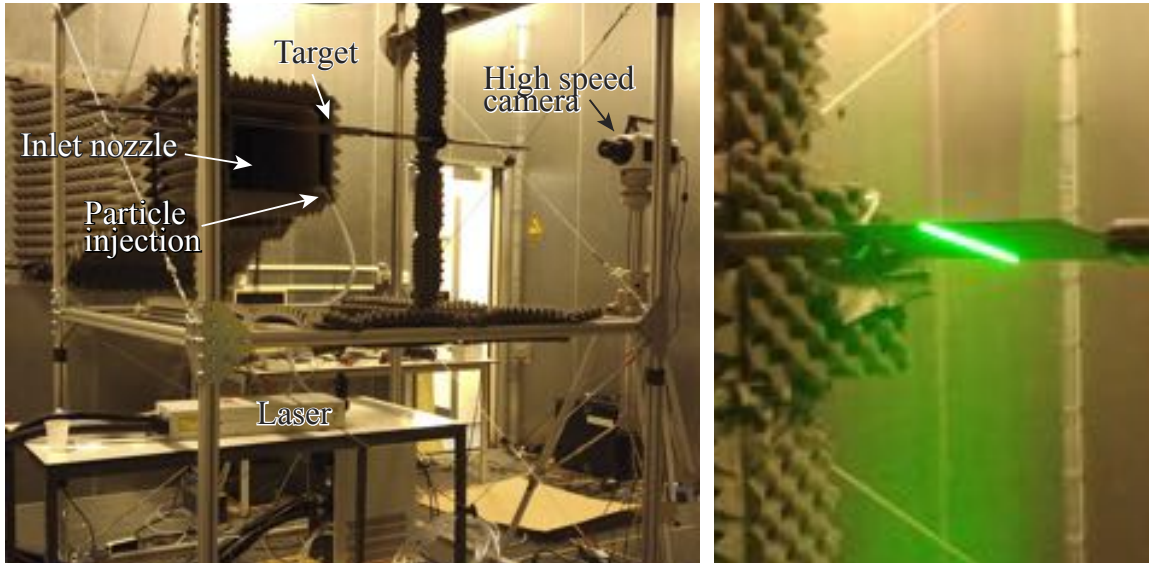


Figure 3.12: Left: PIV setup in the wind tunnel. Right: laser sheet around the angled straight wing.

### Particle behavior

For the particles to be visible to the camera the light scattering is important to consider. The behavior is dependent on the particle properties and on the wavelength of the scattered light. The particles generated by the used seeding system have an average diameter of  $0.9 \mu\text{m}$  and the liquid is an oil. The wavelength of the light produced by the laser is  $532 \text{ nm}$ . For this type of configuration the scattering properties are shown in Fig. 3.13. For the current setup the view angle will always be close to  $90^\circ$  with respect to directionality of the light, resulting in relatively poor light intensity. This is compensated for by using a high intensity laser, and if required a slightly longer duration pulse.

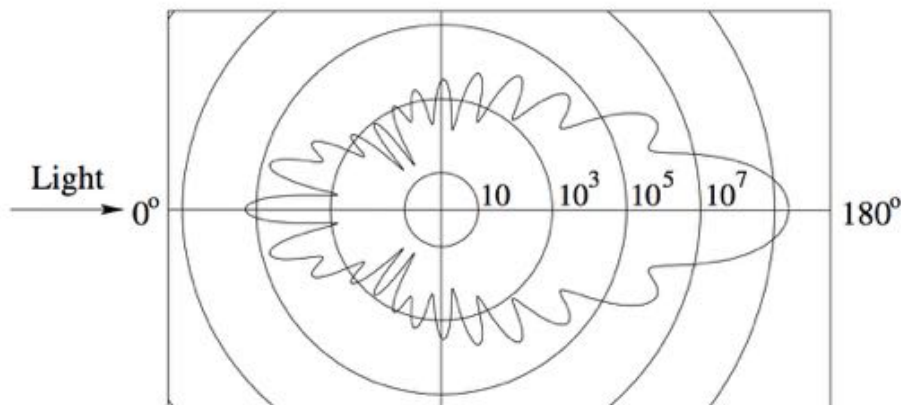


Figure 3.13: Light scattering relative intensity of an oil particle ( $d_p = 1 \mu\text{m}$ ), incoming light  $532 \text{ nm}$ . Ref. [19] page 19.

The assumption in using any PIV setup is that the particles will closely follow the velocity field of the surrounding fluid. There has been significant research into this topic. In order to estimate the particle behavior in this setup the 1997 paper by A. Melling [16] is used. The equation of motion for a (spherical) particle in any flow field is described by the following equation of Basset [5] where temporarily  $\vec{v} = \vec{u}_p - \vec{u}$ :

$$\begin{aligned} \frac{\pi d_p^3}{6} \rho_p \frac{d\vec{u}_p}{dt} = & -3\pi\mu d_p \vec{v} + \frac{\pi d_p^3}{d} \rho_f \frac{d\vec{u}}{dt} - \frac{1}{2} \frac{\pi d_p^3}{6} \rho_f \frac{d\vec{v}}{dt} \\ & - \frac{3}{2} d_p^2 (\pi\mu\rho_f)^{0.5} \int_{t_0}^t \frac{d\vec{v}}{d\xi} \frac{d\xi}{(t-\xi)^{0.5}} \end{aligned} \quad (3.4)$$

This equation is little intuitive but we can see the different contributions to the difference in velocity between fluid and particle which is interesting. On the left hand side of the equation we see the inertia term, i.e. the mass of the particle times its acceleration. The first term on the right hand side is the viscous resistance. This term combined with the LHS is Stokes' law. The second term is the force due to the pressure gradient surrounding the particle caused by the fluid moving around the particles. And the third term is the resistance of an inviscid fluid to acceleration of the sphere. The final fourth term on the right hand side is the 'Basset history integral', modeling unsteady effects in the wake. These contributions will describe the full particle motions.

Based on this model the same paper by A. Melling obtains a measure for the relative velocities between particle and fluid. This depends on the following characteristic frequency of the particle fluid system (Ref. [16] *Fig. 3., Eq. 12*):

$$C = \frac{18\mu_f}{\rho_p d_p^2} [Hz] \quad (3.5)$$

In our case the particles are a specific oil ( $\rho_p = 912 \text{ kg/m}^3$ ), and the particle diameter is  $d_p \approx 1 \cdot 10^{-6} \text{ m}$ . The viscosity of the liquid is also known. Therefore the value of  $C$  we have in our experiments is equal to  $C \approx 2.7 \cdot 10^5 \text{ Hz}$ . Based on the results in the work of A. Melling we can now see that up to a fluctuation frequency of  $\pm 10^4 \text{ Hz}$  the difference between  $u$  (actual flow velocity) and  $u_p$  will be less than  $\pm 10\%$ . This implies that the energy content of high frequency turbulence will be reduced in the PIV results. According to the paper the inertia effects of the particle start playing a role at  $\pm 2000 \text{ Hz}$ .

## Image processing

To obtain quantitative data from any PIV images the positions in the image must be related to real world distances. In addition there are the camera angle and camera/lens distortions to take into consideration. For this reason a calibration photo is taken of a known target image, as is depicted in Fig. 3.14. Using software this image can be transformed into a view completely perpendicular to the measurement plane, a vector of unit length placed in this image will when moved not rotate or elongate. This transformed image is shown in the figure. Because the distances between the

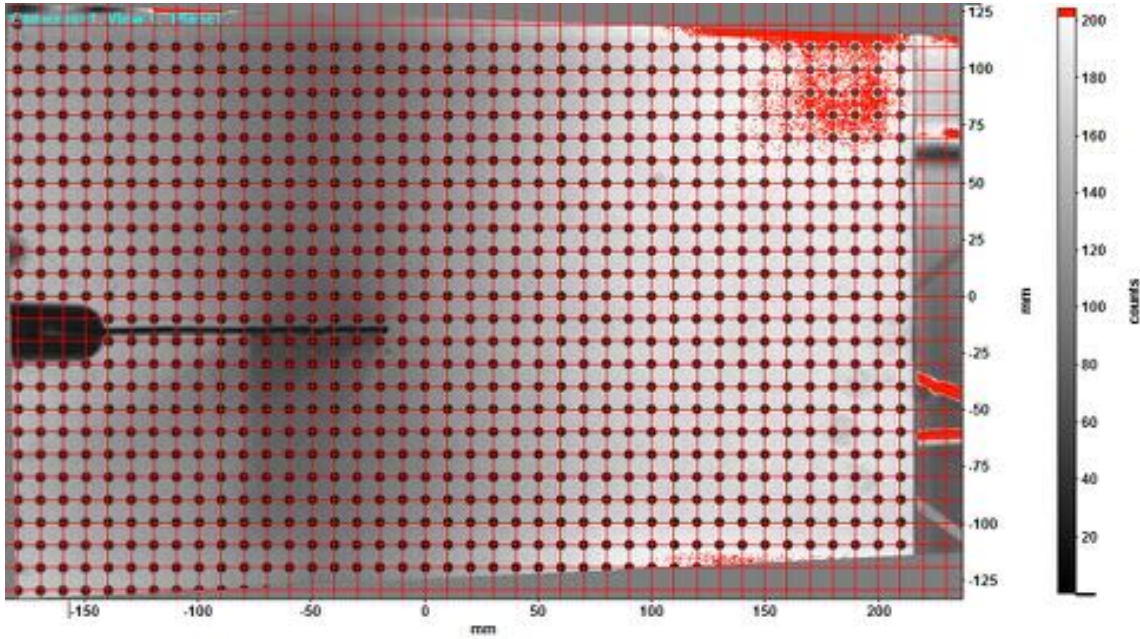


Figure 3.14: Camera image angle and lens corrections applied to target photo.

points on the target are also known the scaling from pixels to real world distances is possible, enabling calculation of physical flow velocities.

Additionally before each measurements twelve background images were taken using the same laser and timing settings. The particles will be visible in each individual image however by averaging of these images the particles will disappear and only the illuminated (stationary) background will remain. For the actual measurements this average will be subtracted from the intensity values resulting in particles on a black background. This approach results in more accurate vector fields with fewer holes. However for some image pairs during high velocity measurements error occur due to the frame vibrating: shifting from its reference position. This creates erroneous vectors in these locations which need to be dealt with in post processing.

### Data processing

The *LaVision - DaVis* software package was used. It was found that for the turbulence intensity measurements the amount of smoothing and post processing strongly affect the end results. Therefore it was decided to use two different methods of post processing, one for the intensity and a second for the integral length scale. For the second it was found beneficial to do some smoothing and interpolation to obtain more valid correlation functions (not containing holes or outliers) and this processing did not change the results since only intensity is affected not spacial/temporal correlation.

The first pass interrogation window shape was chosen to be a horizontal ellipse of 4 : 1 since there is a main flow component in horizontal direction. The second pass uses regular square windows. The final spacial resolution for the turbulence intensity of  $3.67 \times 3.67$ , and for the integral length scale of  $2.45 \times 2.45$ .

In these PIV images it turned out that the Cartesian directions based on the reference photo did not correspond to the main flow and transverse directions. The reason is the reference plate tended to angle slightly downwards when mounted on the wing. For this reason an optimization algorithm was devised to find the angular rotation of the coordinate frame in order to minimize the transverse flow component. The resulting distribution of found mean angles is displayed in Tab. 3.3. For a single configuration the distribution of angles is also plotted for all 240 image frames in Fig. 3.15. From this we can see that the flow angle is reasonably constant and appears to increase with flow speed, indicating a flow moving more downwards. The found angles appear to follow a normal distribution which is expected.

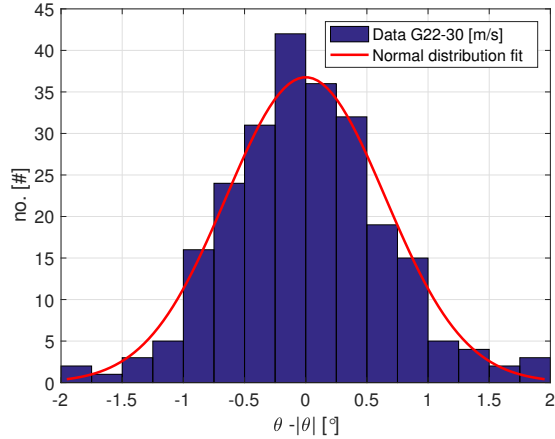


Figure 3.15: Distribution of found flow angles for grid 1. (2x2) at 30 m/s and the corresponding normal distribution fit.

Grid no.	Set flow velocity		
	15 [m/s]	30 [m/s]	45 [m/s]
1. (2x2)	1.97°	1.86°	2.50°
2. (3x3)	1.97°	2.31°	3.37°
3. (4x4)	1.82°	2.10°	2.31°

Table 3.3: Mean flow angles found using the PIV vector field rotation algorithm.

### Measurements procedure

The PIV measurements were performed for all combinations of flow velocity and turbulence grids in order to check the CTA measurements. These measurements were performed twice; once investigating the area surrounding the leading edge with the camera upstream, and once with the camera downstream focused on the wing and area slightly behind the trailing edge. Note that no wing was present in order not to modify the turbulence. Each measurement consists of 240 image pairs obtained over a 20 second period after the flow was allowed to stabilize. Any results obtained from these images are the statistical average of this data set.

The theoretical model discussed in this report assumes that the turbulence upstream of the wing is not affected by the presence of the wing. In other words: the turbulence reaching the wings leading edge is statistically identical to the free stream turbulence. In order to verify this PIV images were taken at the leading edge of the wing (with the wing present) for all velocities and grids. Based on examination of the turbulence intensities and integral length scales in the flow no noticeable difference was observed between the two, validating the assumption made in the model. An example image

of this is depicted in Fig. 3.16. Based on this image we can see the effect of the wings presence and the noise generation mechanism. Near the airfoil boundary the motion of the vortices gets impeded upon, resulting in zero normal velocity near the boundary. This effect is clearly visible in this image, the turbulent eddies are squeezed and stretched, creating high frequency oscillations as they rush by the airfoil. Because there is also interest in applying the model for different angles of attack it was interesting to see how well the system can capture the flow behavior around a angled flat wing. Especially in detecting flow separation and recirculation regions since the theory will not be applicable in those cases. Therefore some images are also made for an angled wing, primarily to test the system.

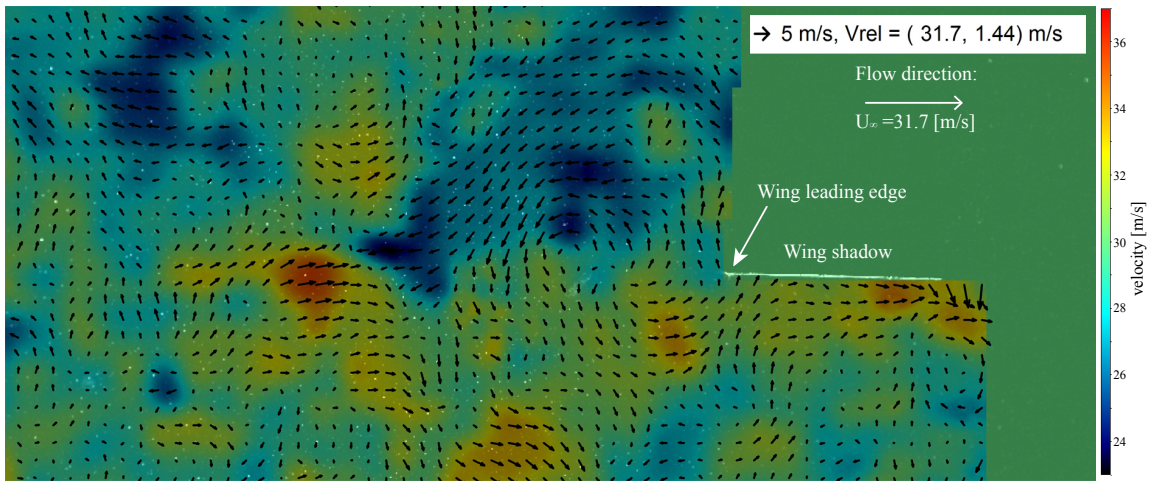


Figure 3.16: PIV applied to leading edge of the flat airfoil single image pair results. Incoming turbulence generated by grid 1 (2x2), mean flow velocity 31.7 m/s. Vector field shown is with mean flow velocity subtracted.

### 3.4.3 Acoustics

The final experiment is designed to obtain the left hand side of Eq. 2.15 i.e. the acoustic spectra. The goal is to experimentally determine the intensity of the noise produced by the airfoils as well as the directionality of this sound.

The acoustic experiments need to be performed for all of the three chosen free stream velocities, corresponding to the velocities used to characterize the turbulence, and for all grid turbulence grid types. The experiments will also be performed without a grid to see the effects.

The resulting spectra obtained from this measurement set will be used as a comparison for the noise predictions using the Amiet model.

#### Acoustics in the anechoic chamber

An overview of the setup used for acoustic measurements is shown in Fig. 3.2. Reduction of ambient noise and limiting reflections is crucial in order to obtain accurate intensity values when doing acoustic measurements. The nozzle and section containing the turbulence grids are covered in a layer of foam designed to dampen

any vibroacoustic noise sources. A secondary layer of pyramid foam was also applied to the whole inlet nozzle in order to reduce any reflections.

The anechoic chamber itself was also cleared of any objects that were not needed during operation. Recreating as best as possible “free field” conditions, in which there are no reflected signals reaching the observer, only the noise directly generated by an object. Sections of the stage tower and any required equipment was also covered with foam for this reason.

### Microphone calibrations and configuration

Fourteen microphones are used in this experiment. The microphones are *LinearX - M51* microphones. The frequency response of these microphones is flat for frequencies up to  $\approx 10 \text{ kHz}$ . Being linear means here that only a single calibration parameter needs to be determined to give accurate intensity readings. A special calibration unit is used producing a Sound Pressure Level (SPL) of  $94 \text{ dB}$  signal at  $1000 \text{ Hz}$ , this corresponds to a root-mean squared value of  $1 \text{ Pa}$ . Thus the linear calibration factor was obtained for all microphones.

It was found that the amplifier channel and the wires used during measurements had a significant effect on the value of this calibration factor. Therefore the calibrations were performed for set channels and wires. These were then labeled and used throughout all experiments in the same configuration.

The Microphones are mounted in an arc, as shown in Fig. 3.2, in order to capture effects of directionality of the noise. The angle of the microphones ( $\psi$  see Fig. 2.1) is defined here around the  $y$ -axis starting from the negative  $x$ -axis. Therefore the microphone near the inlet (upstream) will have the smallest angular value. The microphones are evenly distributed along the arc at  $9.23^\circ$  intervals. The angle of the first microphone is  $31.5^\circ$ . The radius of the arc is exactly  $1500 \text{ mm}$ . The microphones are mounted  $10 \text{ mm}$  closer to the center making the microphone distance  $1490 \text{ mm}$ . The microphones are mounted directly over the centerline of the wing and nozzle ( $y = 0$ ).

In some cases there was some issue with noise contamination by the free stream affecting the microphones at the end of the array. A fix was attempted by using foam caps to insulate the microphones against low-frequency gusts. It was found to not be effective, in addition to this the intensity was slightly affected which is undesirable. Therefore the microphones were employed in their unaltered state.

### Mounting and positioning of the wings

The wings are mounted in the center of the inlet nozzle. The center of the wing is positioned  $1200 \text{ mm}$  behind the turbulence grids. The center of all coordinate systems, unless otherwise stated, is this central position: in the center of the nozzle outlet  $1200 \text{ mm}$  behind the grids. The leading edge of the wing is the central point of the microphone array, note that this does not apply for the circular wing.

All wings are held by two rods from the sides. The rods have markings on them indicating the positioning of each wing. The rods have two ends; one to mount flat plate wings (clamps) and the second for the circular wings (prongs). This is depicted

in Fig. 3.17. The wings are mounted into place in the clamps. Spacer plates are used to fill the excess space between the clamps and wing in order to prevent generation of aeroacoustic noise. The rods are connected to the “stage tower” and tightened. It was found that the wings will not vibrate or shake in this configuration.

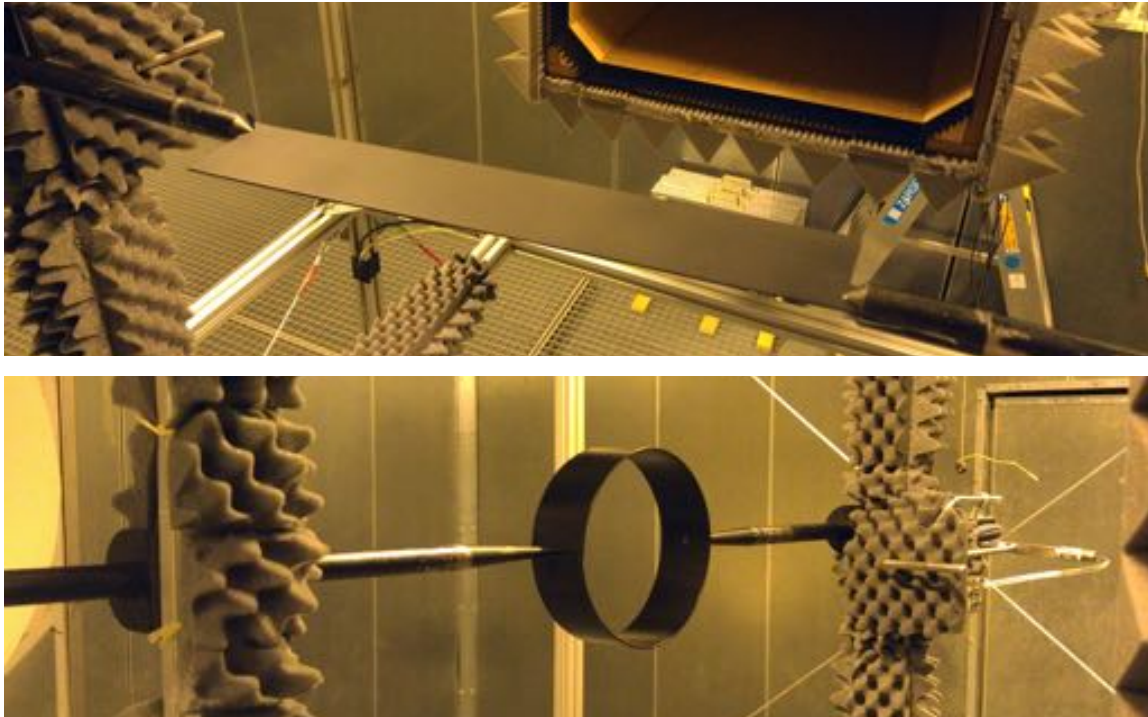


Figure 3.17: Top: Swept wing mounted in the clamps which are tightened using set screws. Bottom: Circular wing mounted on the prongs, bolts are used on the inside of the wing to attach it to the prongs.

### Data acquisition and processing

The microphones are connected to amplifier boxes, which also provide the power to the microphones. The amplifier boxes are connected to a *National instruments PXI 1042q* with two data acquisition cards *PXI 4472* installed. These cards can sample up to a frequency of  $102.4\text{ kHz}$ . The cards contain both an analog and digital filter. The analog filter is set to filter out any frequencies beyond the range of the A/D converters, preventing contamination of the lower frequencies. Next the digital filter is set to the Nyquist frequency corresponding to the set sampling frequency in order to negate the effects of aliasing.

The system is operated by means of MATLAB. The read data is also converted into  $Pa$  using MATLAB and the predetermined calibration values. Acoustic data is converted into power spectral density plots. The MATLAB function *pwelch* is used to do all spectral density estimations. A spectral resolution of  $9.77\text{ Hz}$  is obtained. For the windowing function a 50% overlap is used, and all windows are windowed using the Von Hann window or Hanning window.

## Measurement procedure

Acoustic measurements are performed for all grids, measurement velocities, and for all wing types specified in section 3.2. The mean velocity near the wing is determined using a Pitot-tube. The positioning of the tube is identical to the CTA measurements, therefore the measured flow velocity, and other flow properties will correspond well to the CTA data.

The temperature is monitored during the measurements using a thermocouple mounted in one of the corners of the inlet. The temperature is adjusted using the cooling system when required. Temperature dependence is far less important when compared to the CTA measurements, but is still kept constant for the duration of the measurements. The effect of changing temperatures is solely limited to affecting the mean flow velocity.

Before the acoustic measurements the wind tunnel is given time to stabilize, after which the Pitot-tube is removed. When the wing is interchanged the tunnel is briefly stopped and given time to stabilize again. Acoustic data is gathered for a 40 second period. All wing measurements are performed in sequence, next the velocity is altered, and finally the grid is changed.

In addition to the wing measurements also background measurements are performed. Firstly without anything present in the flow i.e. the background levels of the wind tunnel. Secondly measurements with the supporting rods in place, for both the flat plate and the circular configuration. A final round of angle of attack experiments has also been performed. The 350 *mm* straight wing was tested for angles of attack for the range  $[-10^\circ, -5^\circ, -3^\circ, -1^\circ, 1^\circ, 3^\circ, 5^\circ, 10^\circ]$ .

# Chapter 4

## Inflow turbulence characterization

In Ch. 2 it was shown that in order to be able to determine the noise radiated by the leading edge a full reconstruction of the turbulence spectrum is required. In order to do this only a few parameters need to be obtained: the mean free stream velocity, the turbulence intensity, and the integral length scale. When spectral reconstruction demands extension to the high frequencies domain the Kolmogorov length scale is also required, which will not be the case here.

In addition a reconstruction model must be chosen, the two models compared here are the Liepmann and the Von Kármán model. In practice generated turbulence does not always adhere to the theory. These models are for theoretical and semi-theoretical isotropic turbulence respectively, and must thus be compared to experimental results. This is especially important since the noise predictions also rely on the turbulence being isotropic.

Two experimental techniques are employed and compared in this chapter and the results are presented. There are also some practical things to take into account since the homogeneity of the velocity and turbulence fields near the wings will also affect the noise prediction model. The obtained results are used as input to calculate the term  $\Phi_{ww}$  in Eq. 2.15.

### 4.1 Homogeneity of the flow field

Close to the grids the turbulence will be not be homogeneous (statistically invariant under coordinate translations) and isotropic (statistically invariant under reflections and rotations). However, due to the decaying nature of turbulence, when no energy is added to the flow this state will decay to a homogeneous and isotropic state Refs. [18], and [8]. This has been shown in experimental work also, however in practice this ideal “free stream turbulence” state is not easy to obtain. The main concern is to get a match between the generated turbulence and the existing models for isotropic free stream turbulence.

For the purpose of leading edge noise generation we are looking for homogeneity in the  $y$ - $z$  plane since this is where the leading edge will be located. The turbulence intensity will decay in the  $x$ -direction since this direction is analogous to time. The main issue is the encroachment of the shear layer into the free stream area. The shear

layer is highly turbulent and will be less isotropic because of the boundary condition at its edges and is thus not free stream turbulence. To apply the semi-analytical noise prediction methods it must be possible to model the turbulence, which is more difficult in this region.

### 4.1.1 Flow field measurements

The flow field in the region in front of the inlet nozzle was fully characterized in order to obtain the best location to place the wings. Based on these results the leading edge of the airfoil was chosen to be located 1200 *mm* behind the grid. An example of the results is shown in Fig. 4.1, this data is for grid 3 (4x4) at a mean flow velocity of 15.5 *m/s*. In this figure the flow field in axial direction (*u*-field) is shown. The figure on the left shows contour lines in three dimensions, the flow is coming from the left and moving to right (i.e. the front plane is closest to the inlet nozzle). On the right the *u*-field is shown in the plane of the leading edge. By superimposing wing outlines the flow properties can be obtained at all points on the leading edge. In this figure we see the main flow channel and the shear layer developing. The velocity in the main channel is homogeneous but the shear layers are obviously not.

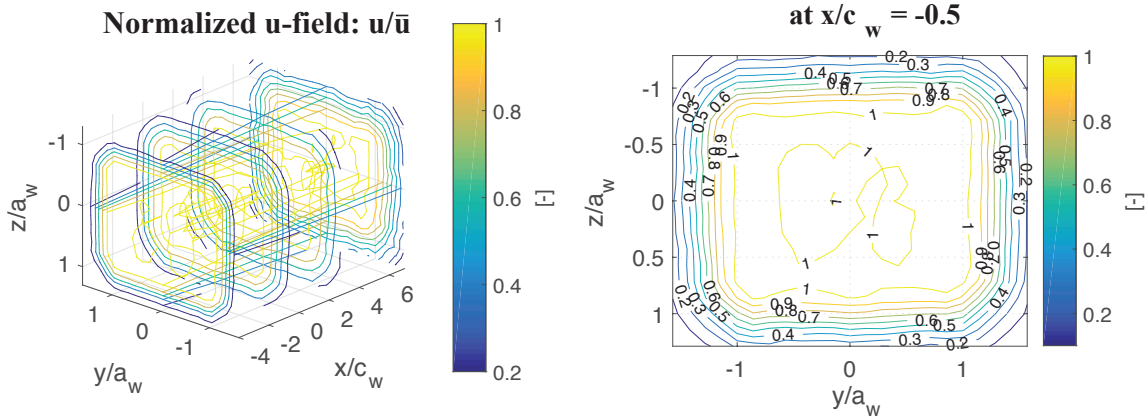


Figure 4.1: Left: Three dimensional view of the normalized velocity in axial direction. Right: Normalized axial velocity in the plane of the leading edge.

The plot in Fig. 4.2 shows the transverse velocity field (the *v*-field). The field is not normalized because it would result in large values, and make the results harder to interpret. It is clear that alignment of the probe is quite good as mentioned previously to within 0.5°, which will have no significant effect on the turbulence properties and their decomposition into axial and transverse direction. It is visible that the flow after it leaves the inlet nozzle diverges, the transverse velocity component is directed outwards from the central *x*-axis. This behavior is as expected.

It is important to note that the velocities at the top and bottom:  $|z/a_w| > 0.6$  are not necessarily realistic. The two-dimensionality of the cross hot-wire is not suited for flows with a relatively large velocity component in the third dimension resulting in a large error since the system is not calibrated for this. Still the results look reasonable enough for both Figs 4.1 and 4.2.

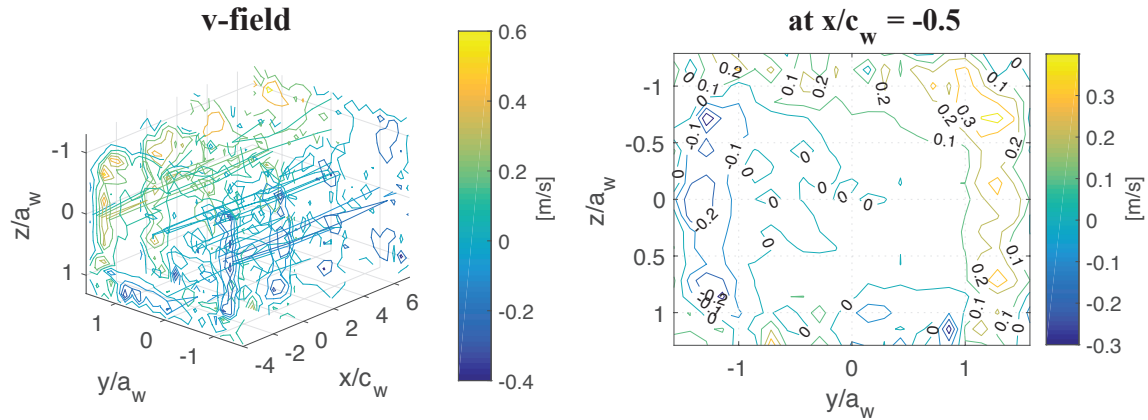


Figure 4.2: Left: Three dimensional view of the velocity in transversal direction. Right: Transverse velocity in the plane of the leading edge.

Similarly the turbulence intensity, defined as  $(TI_i = u'_i/U_\infty)$ , in both directions can also be displayed. Figs. 4.3 and 4.4 show examples of these for respectively the intensity in  $x$ - and  $y$ -directions. In these figures the shear layer and its thickness is very clearly visible. The intensity appears homogeneous in the main channel for both components, this is slightly surprising for the least dense grid. Additionally the growth of shear layer in  $x$ -direction is beautifully visualized. This is the main reason for the choice of wing location. The growth is quite rapid so further back is not an option. Closer to the inlet there was some instability in the velocity field present in some cases which is undesirable.

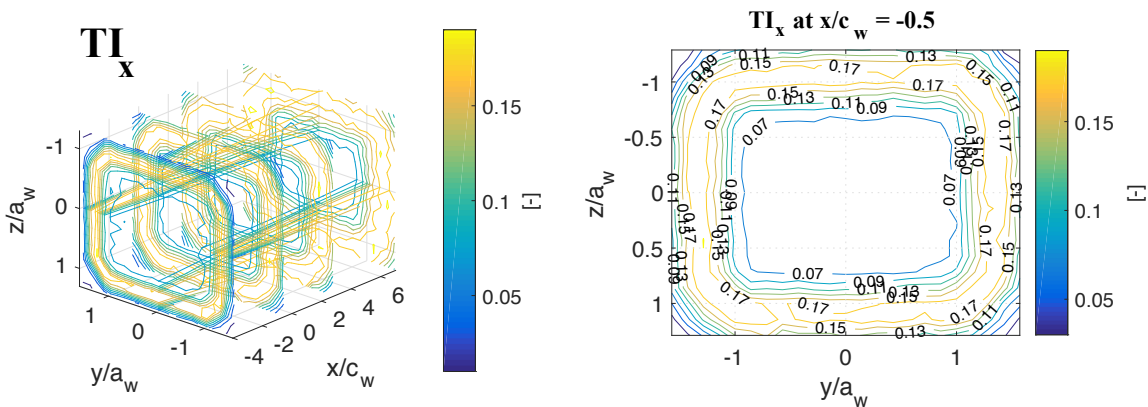


Figure 4.3: Left: Three dimensional view of the turbulence intensity in axial direction. Right: Axial turbulence intensity in the plane of the leading edge.

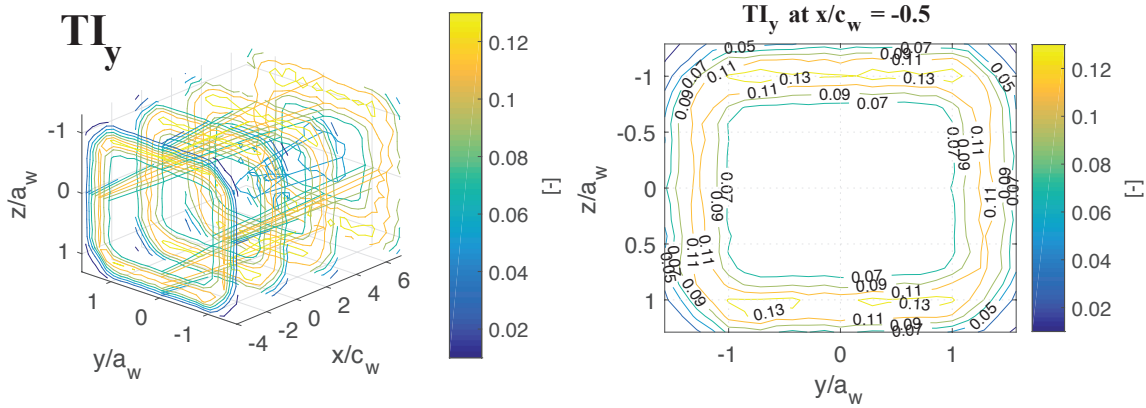


Figure 4.4: Left: Three dimensional view of the turbulence intensity in transverse direction. Right: Transverse turbulence intensity in the plane of the leading edge.

Finally the isotropy of the generated turbulence is depicted in Fig. 4.5, defined as  $TI_{xy} = TI_x/TI_y$ . This shows that the turbulence generated is homogeneous in the main channel, it however is not fully isotropic since it is not equal to singularity. This deviation is observed in almost all of the papers referenced in appendix C, even for the more advanced grid types. It is the general consensus that though not ideal it often is not harmful in regards to statistics and spectral properties of the turbulence and can still be approximated accurately using the assumption of isotropic turbulence. In this figure the shear layer is again visible, here as a clear source of anisotropy. In outward direction the ratio increases rapidly, this is the main reason the wing should not be submerged too much in this region.

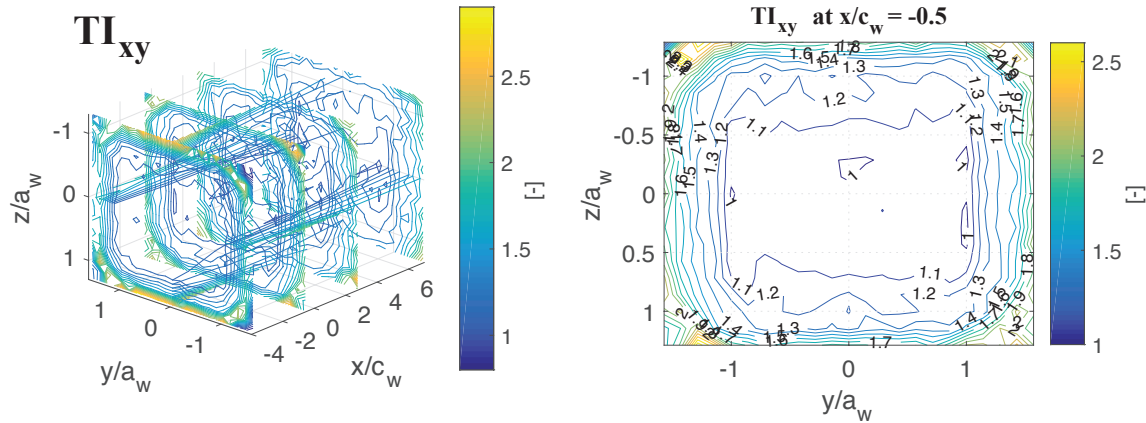


Figure 4.5: Left: Three dimensional view of the turbulence isotropy. Right: Turbulence isotropy in the plain of the airfoil leading edge.

These graphs are available for all grid and velocity configurations. The results between the separate measurements was very consistent. An interesting thing to note is that in some cases you can tell from the closest observation plane where the rods are located in the turbulence grids. This becomes visible from the velocity profile and turbulence intensity, i.e. the turbulence is not yet fully developed.

## 4.1.2 Leading edge measurements

The full measurements were extended using longer duration measurements on the leading edge location as previously mentioned in section 3.4.1. This makes it possible to obtain detailed information about the turbulence properties. For the configuration discussed in the previous section, grid 3 (4x4), the results are provided in Fig. 4.6 and 4.7. Here all free stream velocities for this grid are shown. N.b. these measurements were also performed for one plane behind the leading edge: i.e.  $x/c_w = 2.833$ . The full set of results, for all grids and the two planes in  $x$ -direction, is provided in appendix D.2.1.

The first figure shows velocity on the leading edge. The velocity in all cases shows some fluctuations in flow speed at the leading edge varying from approximately  $0.95 |u|$  to  $1.05 |u|$ . It should be noted that in this regard grid 2 (3x3) functions best. These results are within expectation for grids that have this high of a solidity ( $\sigma^*$ ).

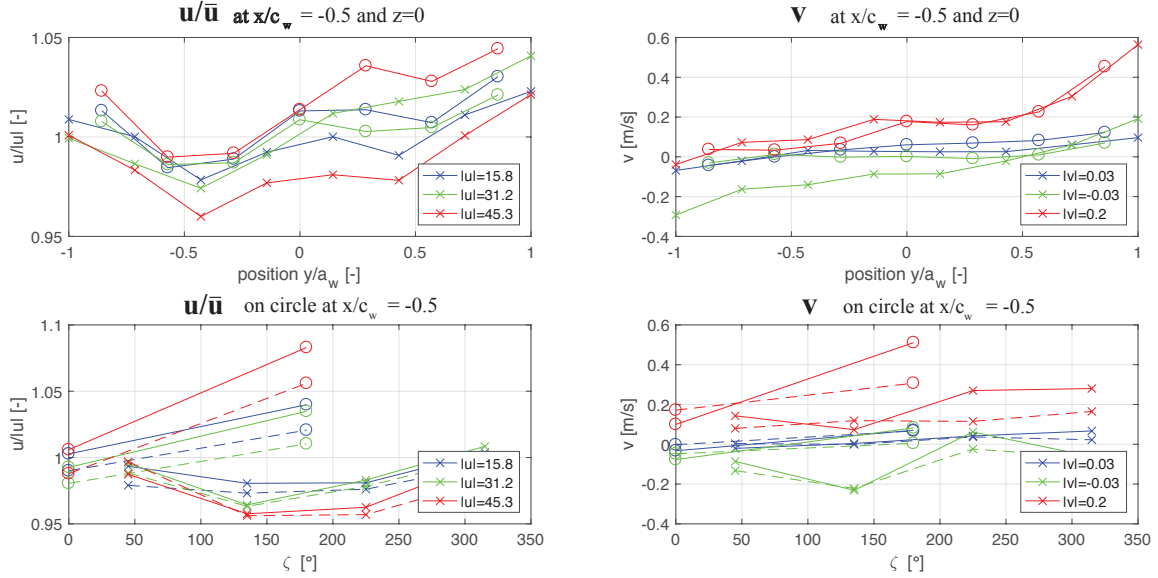


Figure 4.6: Left: Normalized axial velocity profile on LE. Right: Transverse velocity profile on LE. Top: Measurements for all flat wings. Bottom: Measurements for all circular wings: unbroken line is  $d_w = 250 \text{ mm}$  dashes is  $d_w = 180 \text{ mm}$ . Crosses and circles corresponds to measurement positions and duration given in section 3.4.1 and Fig. 3.9.

The second important characteristic is the turbulence intensity distribution along the span of the airfoil as shown in Fig. 4.7. It is observed that for the lower solidity grid the turbulence intensity is more constant along the leading edge. The TI is increasing near the tips of the wing, on the main part off the wing the intensity is very homogeneous in general. The results match very well with the shorter duration measurements performed. The isotropy value of the generated turbulence is excellent in the region on the leading edge, for higher solidity grids this is again worse.

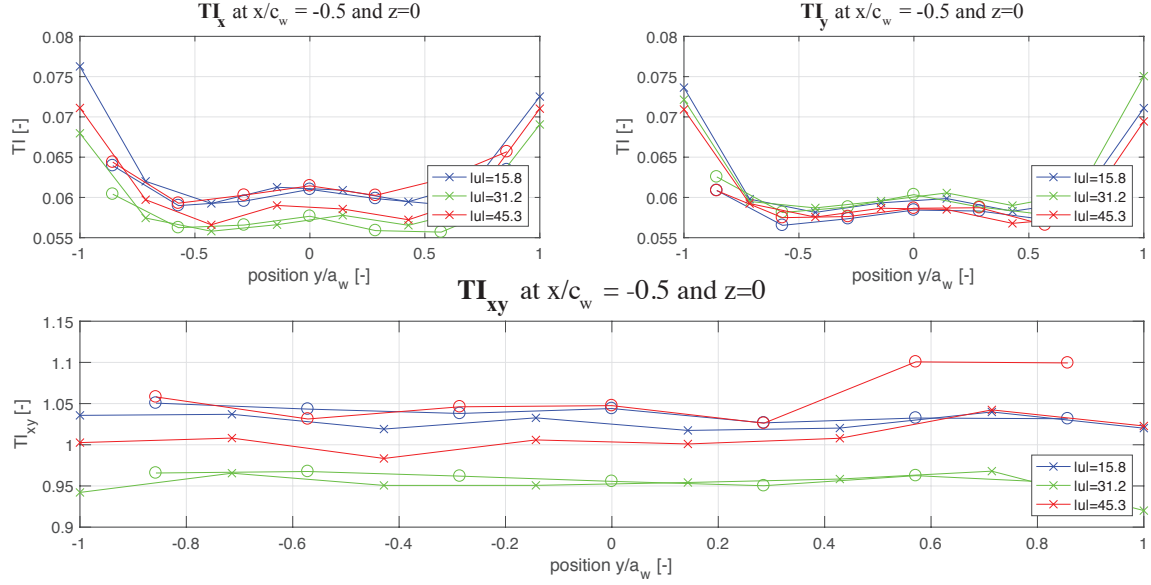


Figure 4.7: Top left: Turbulence intensity in axial direction on leading edge. Top right: Turbulence intensity in transverse direction on leading edge. Bottom: Turbulence isotropy on leading edge.

The values used in the semi-analytical model for the mean flow velocity and turbulence intensity are given in Tab. 4.1 for all grids and free stream velocities. Interesting to note here is that the turbulence intensity increases with a higher solidity, i.e. a decreasing blockage. For low solidity grids the inverse relation is found in literature, this was also observed for the initial grid designs which all had a solidity below  $\sigma^* = 0.5$ . The results found here are slightly counter intuitive, especially since based on Fig. B.1 in appendix B we note that more energy is extracted for the grids with higher blockage.

## 4.2 Integral length scales

To calculate the integral length scale the spacial coherence in the flow field needs to be evaluated. For this it is customary to use spacial correlation functions. In this case however the signal data is a function of time, not position. However by assuming the flow to be frozen, i.e.  $u'/U_\infty \ll 1$ , we can use Taylor's hypothesis to convert temporal scales to spacial scales. The idea is that sampling in different positions in the flow is identical to sampling at different times when the flow has moved past at a known speed. This allows us to use temporal autocorrelation functions on the signal and convert the results from time lags to spacial lags. The temporal correlation functions are:

$$\rho_{uu}(\tau) = \frac{|u(t)u(t + \tau)|}{u'(t)u'(t + \tau)} \quad (4.1)$$

$$\rho_{vv}(\tau) = \frac{|v(t)v(t + \tau)|}{v'(t)v'(t + \tau)} \quad (4.2)$$

These correlation functions for a single position for all grids and velocities are shown in appendix D.2.3. As is expected the temporal lags become smaller for increased flow velocity. Because we can apply Taylor's hypothesis the conversion from temporal lags to spacial lags is given as:

$$x_l = \tau|u| \quad (4.3)$$

Based on this equation we now have the correlation functions as a function of  $x_l$  instead of  $\tau$ : thus  $\rho_{uu}(x_l)$  and  $\rho_{vv}(x_l)$ . The formal definition of the integral length scale is defined as:

$$\Lambda_x = \int_0^\infty \rho_{uu} \, dx \quad (4.4)$$

$$\Lambda_y = \int_0^\infty \rho_{vv} \, dy \quad (4.5)$$

In practice it was usual to calculate the integral up to the first zero crossing, since the remainder is just oscillations around zero. Based on the calculated values of  $\Lambda$  a model can be constructed. The models for the correlation functions considered here are the theoretical Liepmann model and the mixed theoretical-experimental model of von Kármán. The spacial correlation models as given by Liepmann are:

$$\rho_{uu}(k_e x_l) = \exp \frac{(-k_e x_l)}{0.75} \quad (4.6)$$

$$\rho_{vv}(k_e x_l) = \left(1 - \frac{2}{3}(k_e x_l)\right) e^{-4/3(k_e x_l)} \quad (4.7)$$

According to the von Kármán model:

$$\rho_{uu}(k_e x_l) = \frac{2^{2/3}}{\Gamma(1/3)} (k_e x_l)^{1/3} K_{1/3}(k_e x_l) \quad (4.8)$$

$$\rho_{vv}(k_e x_l) = \frac{2^{2/3}}{\Gamma(1/3)} (k_e x_l)^{1/3} \left[ K_{1/3}(k_e x_l) - \frac{k_e x_l}{2} K_{-2/3}(k_e x_l) \right] \quad (4.9)$$

In these equations, from Refs. [14] and [17],  $K$  is a Bessel function of the second kind, the subscript value is a control parameter. The variable  $k_{e,i}$  is the wave number of the energy containing eddies, which is mathematically related to the turbulence integral length scale by:

$$\Lambda = \frac{\sqrt{\pi} \Gamma(5/6)}{k_e \Gamma(1/3)} \quad (4.10)$$

Note that  $k_e$  will be different for axial and transverse components.

In this report the method used to compute the integral length scale is an inverse method. Instead of calculating the value and then making the model, the model is directly fitted to the data and the appropriate value of  $\Lambda$  is extracted. This method was preferable for the current data since the correlation functions in many cases crossed zero only for very large lags. However the results up to  $\rho \approx 0.1$  matched very well with the theoretical models, therefore the use of this inverse method can be justified.

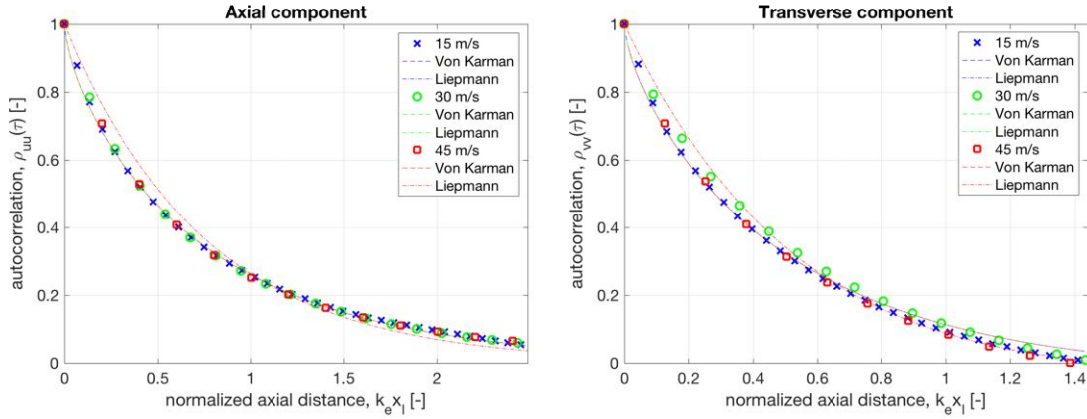


Figure 4.8: Axial and transverse autocorrelation measurement data fitted according to Kármán and Liepmann correlations.

The data and resulting fits for grid 3 (4x4) are shown in Fig. 4.8. Not all data points are plotted in order to avoid cluttering the image. It can be seen that for all velocities the fits match very closely to the von Kármán model for small axial distances. This appears to be the case for both the axial and transverse autocorrelation functions. The algorithm itself decides which model is a better fit and uses that to determine the value of  $\Lambda_i$ . In all cases it was found that the von Kármán model provided the better results. Results for the other grids are provided in appendix D.2.3. These results are excellent, the fits match very closely in all cases, even for probe positions on the edge of the wing (near the shear layer). This suggest that the tur-

bulence can be well modeled using the isotropic turbulence model and should be adequate for noise prediction purposes.

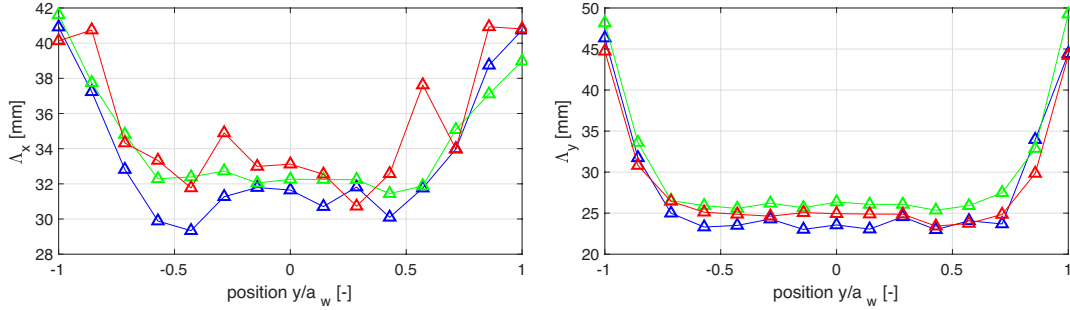


Figure 4.9: The integral or Taylor length scale plotted for several transverse positions on the y-axis. Upwards pointing triangle indicates von Kármán's correlation was used and a downwards pointing triangle indicates the theoretical Liepmann relation was used to determine the length scale.

Using these fitted functions the integral length scale is calculated for all measurement positions. For grid 3 these are shown in Fig.4.9. As can be observed the length scale grows rapidly near the shear layers, since this is not grid generated turbulence the length scales here will not be related to the grid dimensions. The average values used in the noise prediction model are given in Tab. 4.1. Interesting is the large difference in axial length scale for grid 1 (2x2). These values are very clear outliers from the rest of the data.

Theoretically in isotropic turbulence the length scales in axial direction and the two transverse directions for free stream turbulence are related by, as given in Hinze [14] (ref. Eq. 3-75):

$$\frac{1}{2}\Lambda_x = \Lambda_y = \Lambda_z \quad (4.11)$$

The ratio of these two is another measure of the isotropy of the turbulence and is also provided in Tab. 4.1. It is however common for this not to exactly match. The differences here are very representative of the general trend observed in the work of others. Some examples are the work of G. Comte-Bellot and S.Corrain [8] and,[9], the report by J.V. Larssen [15], and the work by M. Gad-el-Hak and S. Corrsin [13].

<b>Grid 0: 0x0</b>									
<b>Velocity:</b>	$\bar{u}$	$\bar{v}$	$TI_x$	$TI_y$	$TI_{xy}$	$\Lambda_x[mm]$	$\Lambda_y[mm]$	$\Lambda_y/\Lambda_x$	
15 m/s	15.35	0.03	0.0349	0.0368	0.9426	-	-	-	
30 m/s	29.66	-0.01	0.0287	0.0317	0.8991	-	-	-	
45 m/s	45.14	0.64	0.0302	0.0297	1.0112	-	-	-	
<b>Grid 1: 2x2</b>									
15 m/s	16.11	0.06	0.0706	0.0624	1.1337	43.2	25.0	0.5848	
30 m/s	31.58	-0.03	0.0681	0.0639	1.0669	44.2	26.4	0.6008	
45 m/s	47.59	0.35	0.0707	0.0602	1.1751	44.2	26.0	0.5946	
<b>Grid 2: 3x3</b>									
15 m/s	15.55	0.04	0.0644	0.0605	1.0655	32.5	24.2	0.7492	
30 m/s	30.64	-0.01	0.0610	0.0614	0.9925	34.9	26.5	0.7629	
45 m/s	45.07	0.22	0.0636	0.0600	1.0610	34.2	25.3	0.7437	
<b>Grid 3: 4x4</b>									
15 m/s	15.82	0.02	0.0608	0.0578	1.0488	32.4	25.1	0.7737	
30 m/s	31.32	-0.05	0.0565	0.0580	0.9723	33.4	27.2	0.8130	
45 m/s	45.31	0.24	0.0603	0.0573	1.0523	34.6	25.7	0.7435	

Table 4.1: Turbulence intensities, isotropy, and Taylor length scales of the different grids at the leading edge of the airfoils  $x/c_w = -0.5$ . The values are the averaged quantities of the interrogation points located on the airfoil.

### 4.3 Turbulence spectra

Using the obtained length scale and turbulence intensity it is now possible to reconstruct the turbulence spectrum for use in noise-prediction algorithms. To test this the isotropic models of Liepmann and von Kármán are again tested but this time against the power spectral density results. The results for grid 3 are shown in Fig. 4.10. The intensity of the spectrum is normalized using the energy in the source range. Also the wavenumber is normalized using the wavenumber of the energy containing eddies. This scaling results in identical spectra for any velocity. This approach is used by R. W. Paterson and R.K. Amiet [17]. The results for other grids are shown in appendix D.2.2.

The models used by Liepmann for the turbulence spectra are:

$$\frac{4\Phi_{uu}(k_x)}{\Phi_{uu}(0)} = \frac{4}{\left(1 + \frac{9k_x^2}{16k_e^2}\right)} \quad (4.12)$$

$$\frac{4\Phi_{vv}(k_y)}{\Phi_{vv}(0)} = \frac{4 \left(1 + 27/16 \left(\frac{k_y}{k_e}\right)^2\right)}{\left(1 + 9/16 \left(\frac{k_y}{k_e}\right)^2\right)^2} \quad (4.13)$$

The von Kármán models are defined as:

$$\frac{4\Phi_{uu}(k_x)}{\Phi_{uu}(0)} = \frac{4}{\left(1 + \frac{k_x^2}{k_e^2}\right)^{5/6}} \quad (4.14)$$

$$\frac{4\Phi_{vv}(k_y)}{\Phi_{vv}(0)} = \frac{4 \left(1 + 8/3 \left(\frac{k_y}{k_e}\right)^2\right)}{\left(1 + \left(\frac{k_y}{k_e}\right)^2\right)^{11/6}} \quad (4.15)$$

From the results in Fig. 4.10 we see that again the von Kármán model provides the better match. The model described the spectrum almost perfectly. This is the case for all grids, therefore this approach is viable for use in noise prediction.

In Fig. 4.11 the spectra for all positions along the wing span is shown for grid 2 (3x3) at a free stream velocity of 30 *m/s*. The results are a very close match also for the region near the shear layer. For the axial component there is almost no difference. In the power input range of the spectrum (up to  $10^{-1}$ ) there is some difference resulting in the slightly higher turbulence intensities, but the energy cascade for all positions is almost identical. The same applies for the transverse flow direction. The differences are however more pronounced. This is because the shear layer will also add energy into this flow component: resulting in larger deviations. Again the cascade is almost identical.

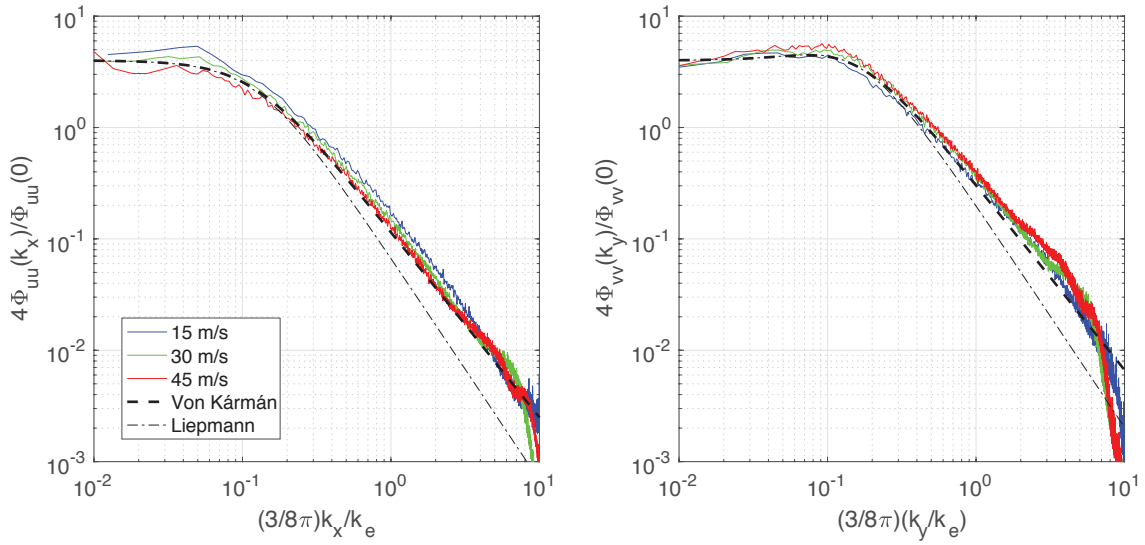


Figure 4.10: Normalized turbulence spectrum for turbulence grid 3 (4x4) at the three measurement velocities of 15, 30, and 45  $m/s$ .

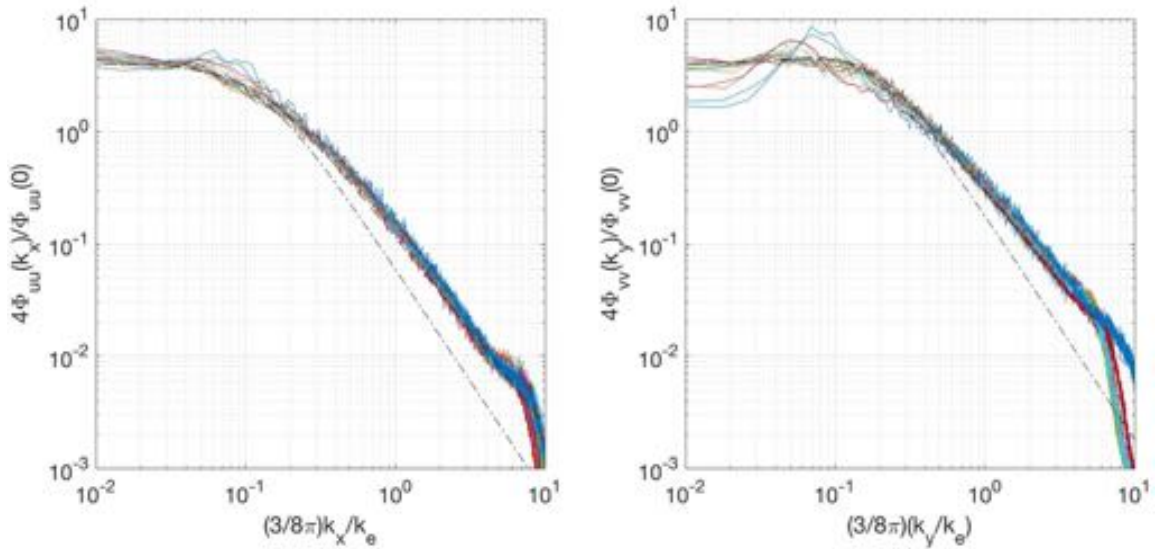


Figure 4.11: Normalized turbulence spectrum for turbulence grid 2 (3x3) at an approximate free stream velocity of 30  $m/s$ .

## 4.4 PIV results

### 4.4.1 Turbulence intensity

Using the rotated vector fields obtained during PIV processing it is possible to calculate the turbulence intensities. This can be done for specific regions, in this case horizontal lines in  $x$ -direction are used. This results in the turbulence intensities as a function of the  $z$ -coordinate. Leading to in comparable measurement results to those obtained by CTA ( $TI$  as a function of a transverse Cartesian direction). In Fig. 4.12 the values are shown for all grids and velocities. Since the velocity field is

again decomposed in two main components ( $u, w$ ) the turbulence intensities are also given in both directions.

The number of vectors on a horizontal line is too little to get good statistics, however because we have 240 images we can use all velocities in the same line for all images. Using this approach there are more than enough statistics for the results to converge and give a continuous representation of  $TI$  as a function of  $z$ .

The average values of the turbulence intensity for each configuration are given in Tab. 4.4.

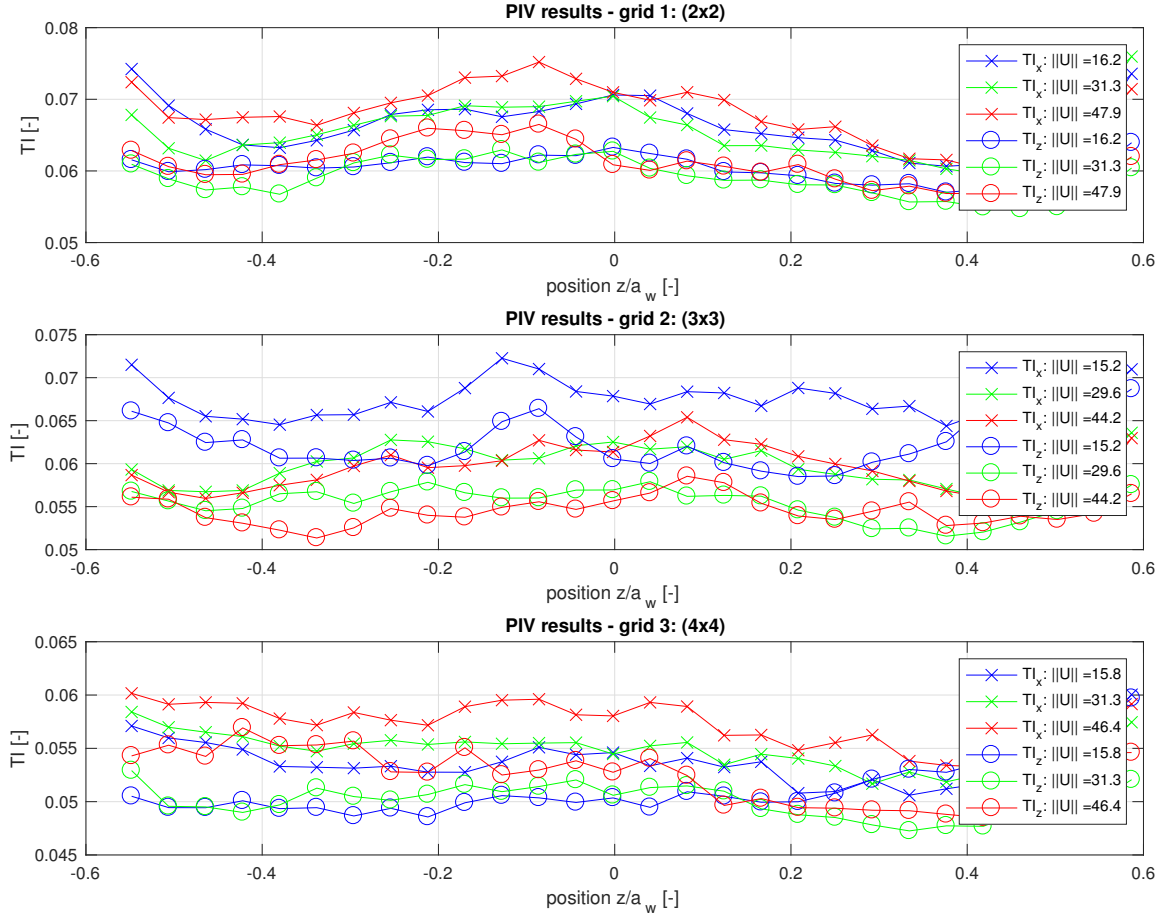


Figure 4.12: Turbulence intensities in both directions obtained using the PIV data. Resolution in  $z$ -direction is approximately 4 mm.

Vel. $m/s$	Grid 1 (2x2)			Grid 2 (3x3)			Grid 3 (4x4)		
	15	30	45	15	30	45	15	30	45
$10^2 \Delta TI_x$	-0.16	-0.05	-0.02	0.61	0.09	-0.17	-0.49	0.01	-0.04
$10^2 \Delta TI_y$	0.00	-0.32	0.31	0.54	-0.42	-0.32	-0.48	-0.64	-0.16

Table 4.2: Differences between the turbulence intensity results of the CTA and PIV measurements. The differences are percentage points differences.

## 4.4.2 Integral length scale

Using the same techniques regarding the correlation functions in axial direction of the transverse and axial flow component makes it possible to also obtain the integral length scale from the PIV measurements. Instead of having to convert the correlations from the temporal domain to the spacial, as was the case for CTA, we already have spacial correlations because PIV provides a spacial overview at a single instance in time.

These methods are programmed into MATLAB and applied to all PIV measurements. It should be noted that for this calculation the filtering and smoothing algorithms actually benefit the results. This is because they do not affect the spacial correlations, only the intensity of the vector field. Additionally these algorithm fill in empty vectors and correct erroneous ones, resulting in more realistic data. Therefore these methods were applied for this analysis.

The results thus obtained are shown in Fig. 4.13 as a function of the  $z$  coordinate. The averaged results are given in Tab. 4.4. A comparison is given between the integral length scales obtained using CTA and PIV in Tab.4.3. This table illustrates an interesting phenomenon. The factor in integral length scale between CTA and PIV experiments appears to be consistent and approximately 1.5. The reason for this remains unclear, no satisfactory explanation has been found.

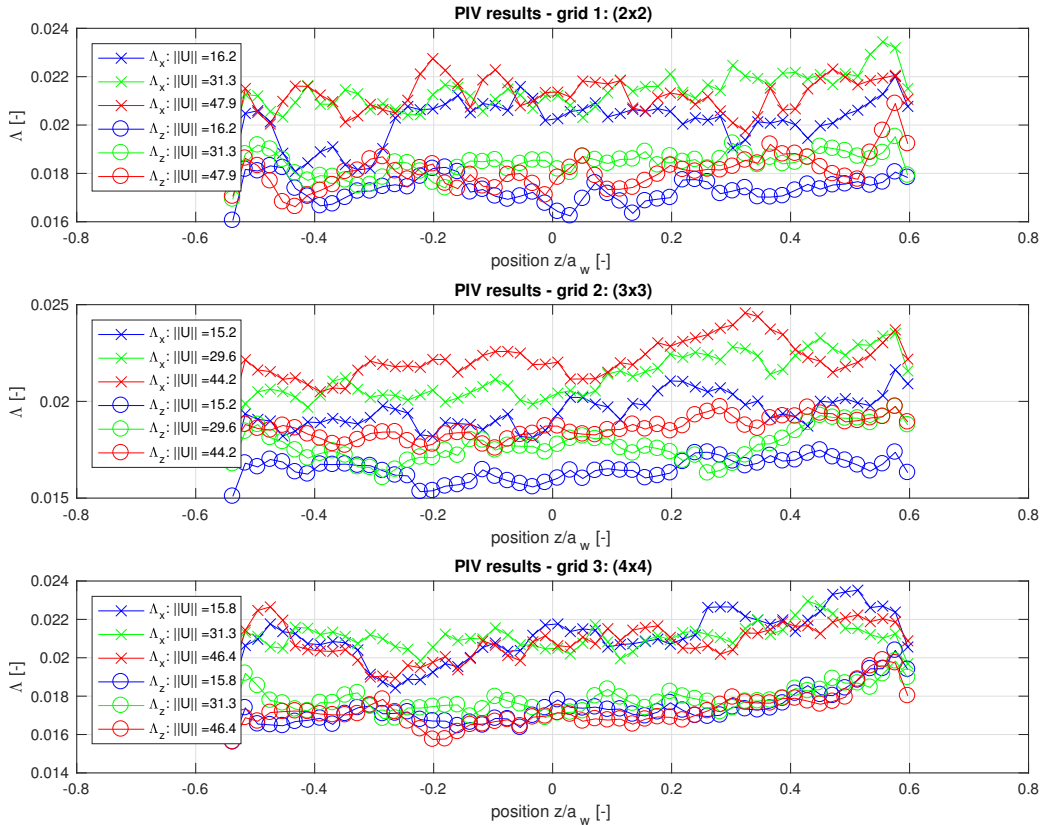


Figure 4.13: integral length scales calculated using PIV for all three turbulence grids and all three free stream velocities. The data is plotted against the vertical transverse direction  $z$ . Both axial and transverse components of the length scale are plotted.

Vel. $m/s$	Grid 1 (2x2)			Grid 2 (3x3)			Grid 3 (4x4)		
	15	30	45	15	30	45	15	30	45
$\Lambda_x$ : CTA/PIV	2.15	2.07	2.08	1.67	1.65	1.54	1.54	1.58	1.66
$\Lambda_y$ : CTA/PIV	1.45	1.43	1.44	1.47	1.50	1.36	1.45	1.53	1.49

Table 4.3: Factor difference in the integral length scale results of the CTA and PIV measurements.

Grid 1: 2x2							
Velocity:	$\bar{u}$	$TI_x$	$TI_z$	$TI_{xz}$	$\Lambda_x[mm]$	$\Lambda_z[mm]$	$\Lambda_z/\Lambda_x$
15 m/s	16.24	0.0690	0.0624	1.1058	20.1	17.3	0.8605
30 m/s	31.28	0.0676	0.0607	1.1137	21.4	18.4	0.8602
45 m/s	47.95	0.0705	0.0633	1.1137	21.2	18.1	0.8524
Grid 2: 3x3							
15 m/s	15.21	0.0705	0.0659	1.0698	19.5	16.5	0.8467
30 m/s	29.61	0.0619	0.0572	1.0822	21.2	17.7	0.8345
45 m/s	44.20	0.0619	0.0568	1.0898	22.2	18.6	0.8395
Grid 3: 4x4							
15 m/s	15.76	0.0559	0.0530	1.0547	21.1	17.3	0.8239
30 m/s	31.32	0.0566	0.0517	1.0969	21.1	17.8	0.8483
45 m/s	46.40	0.0599	0.0557	1.0754	20.8	17.2	0.8268

Table 4.4: Averaged results based on the PIV measurements. The location in x-direction is around the leading edge of the airfoil.

#### 4.4.3 Velocity statistics - higher order moments

Another way to compare the turbulence is by means of the statistics of the measured velocities. The higher order statistical moments i.e. skewness (third order moment), and kurtosis (fourth order moment) are a good indicator for turbulence flows. The skewness is an indicator for asymmetry in the probability density function and is zero for isotropic free stream turbulence. This was found to be the case for both CTA and PIV measurements for all configurations. The kurtosis, or flatness of the distribution, indicates how likely the outliers are relative to results near the mean value. In free turbulence we expect it to follow closely to a Gaussian distribution which has a kurtosis of 3, see [15] pages 62-66. For both the CTA and PIV data this turned out to match very closely for all configurations. Only for grid 1 (2x2) at 15  $m/s$  it deviates significantly for PIV. It gives a value of around 5 in both directions. This corresponds with the deviation in integral length scale found in the CTA measurements. This could indicate that the isotropic turbulence model is not sufficient to describe the flow for this configuration.

#### 4.4.4 Upstream influence of thin airfoil

The turbulence in front of the airfoil was compared with the turbulence in the same location without the wing present, in order to see the its effects. The assumption is that the wing will not affect the flow field until it passes over the wing. The region compared is 20 *mm* high and 45 *mm* long. The closest point of the area is located 5 *mm* in front of the airfoils leading edge.

In this region the turbulence intensity and integral length scale deviated very little when the same PIV procedures were applied. No significant outliers were detected here. This suggests that the turbulence models for the free stream without wing will be a good representation of the same region when the wing will be present.

The probability density functions for the fluctuating part of both flow components in this region are also compared. The data is the accumulation over 240 image pairs collected using grid 3 (4x4) at 30 *m/s*. The results are shown in Fig. 4.14. Something very interesting is visible here, even though the intensity does not appear to be affected the distribution is slightly different. The axial component appears to be flattened, corresponding to a higher kurtosis. The transverse component however is largely unaffected. This is good for noise prediction since the transverse component is crucial in this.

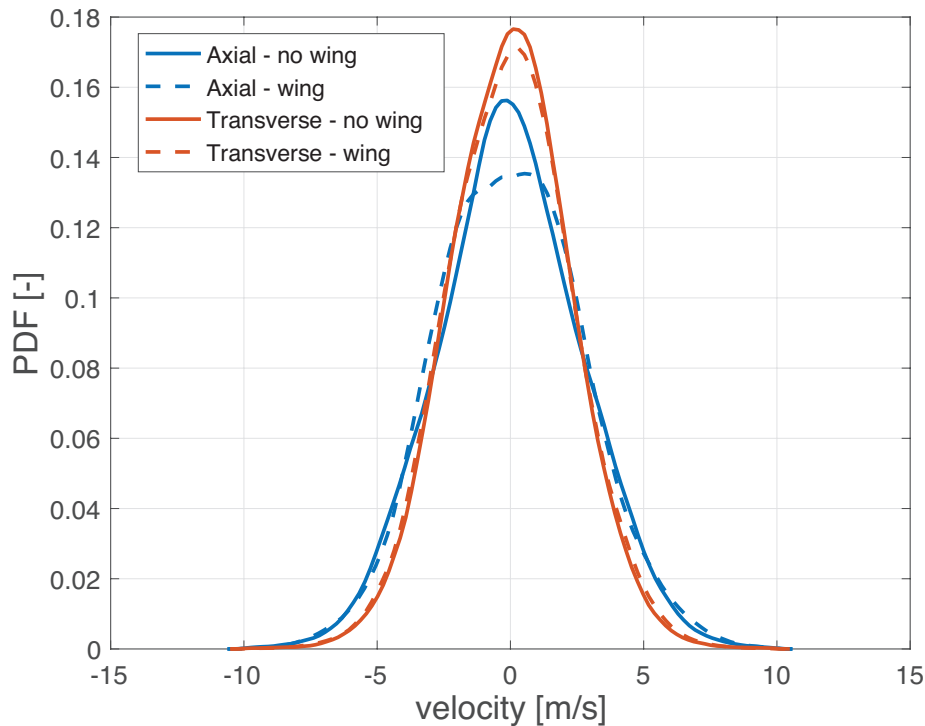


Figure 4.14: Probability density function for the velocity field without the wing (solid line) and with the wing (dashed line).

# Chapter 5

## Acoustic far-field experimental results

Acoustic signals are obtained for the three different turbulence grids and for the case of no grid. The velocities used in the measurements are 15, 30, and 45  $m/s$ . All wing types are tested for all of these configurations. Additionally the angle of attack was varied from  $-10^\circ$  to  $10^\circ$  for the straight airfoil using both grids 2 and 4 at the same velocities.

### 5.1 Background noise levels

The improved grids with a higher solidity  $\sigma^*$  resulted in better acoustic signal-to-noise ratio. However it is still useful to quantify the noise produced by these grids. Therefore an experiment was performed using the acoustic array to determine the noise levels and directionality of the background noise.

The results for a single microphone are shown in Fig. 5.1. Based on the results presented here there is a significant increase in the background noise for higher flow velocities, this fits with aeroacoustic scaling of noise. This effect is much stronger than the effects of the different grid densities. We do see increase in the noise for more denser grids. This increase appears reasonably consistent for all flow velocities and is approximately 2.1  $dB$  between the grids 1 and 2, and 4.8  $dB$  between grids 2 and 3, which is a significant increase. From the initial grids and their noise production levels we learned that the grid noise will result in significant adverse effects on the signal-to-noise ratio.

These results contain no significant sources of tonal noise or other contamination. This is favorable for the measurements with the wing present, making it possible to evaluate the entire range of the frequency spectrum for which there is enough signal-to-noise ratio. It was also noted that the background noise intensity is lower for the microphones upstream (above the inlet nozzle). This reduction in noise levels is very significant and indicates that most of the noise is indeed produced by the grids and the outlet. The noise levels in vertical direction compared to the microphones down stream (larger angle) are near identical. Only at high velocities there is some contamination in the low-frequency regime due to the shear layer interacting with

the last microphone in the arc. This effect of background noise directionality will be corrected for, due to the background subtraction performed on the wing signal.

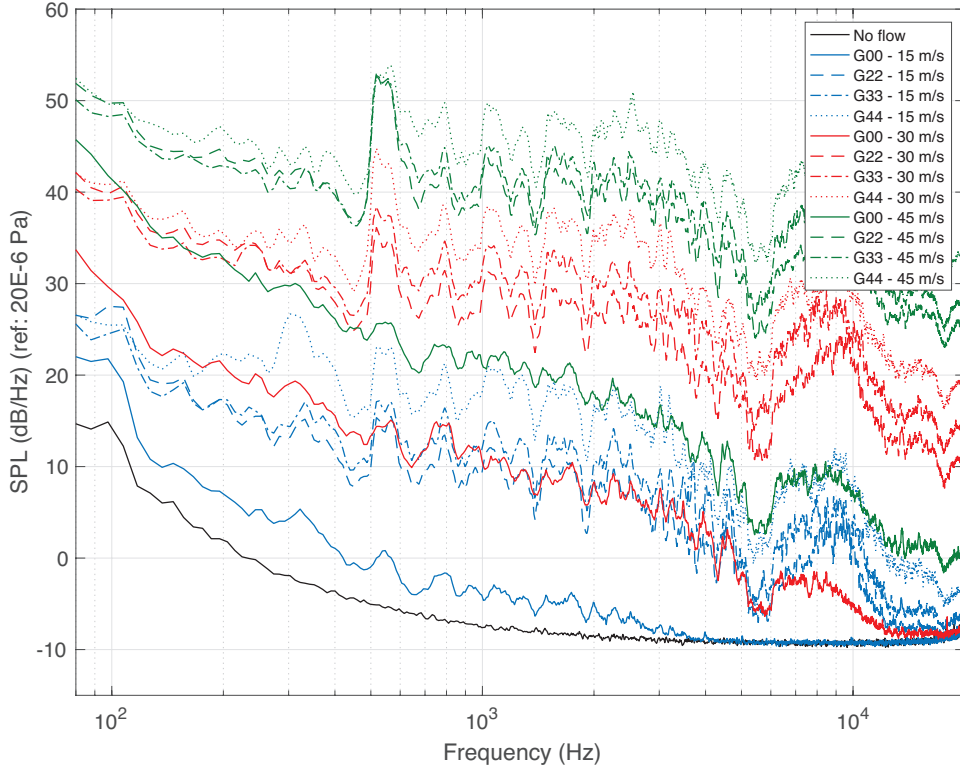


Figure 5.1: Background noise produced by the wind tunnel. For all flow velocities and grid types.

## 5.2 Flat plate measurements

### 5.2.1 Acoustic signals

Three examples of acoustic spectra obtained for two configurations are shown in Figs. 5.2, 5.3, and 5.4. The results shown in these figures are after background subtraction is applied. This is the acoustic signal of wing and support minus the acoustic signal of only the support. The assumption here is that the noise produced by the wing and support interacting is negligible. Thus the difference between the two measurements is purely caused by the wing interacting with the turbulent in flow, which is what we want to obtain.

The first figure is an example of tonal noise produced by a thin airfoil. This is the results of having no grid present in the flow and the resulting very low free stream turbulence intensity. The behavior observed here is caused by trailing edge noise, governed by the scattering of flow instability waves reaching the trailing edge. The second and third figures show leading edge noise for grid 2 at 30 *m/s* for respectively a circular and a flat plate wing. The noise produced by this configuration is broadband noise, no distinct frequencies are present in the signal. The results are similar in

characteristics to those observed in the works of R.W. Paterson R.K. Amiet and [17], M. Roger [22], and L.D. de Santana [11].

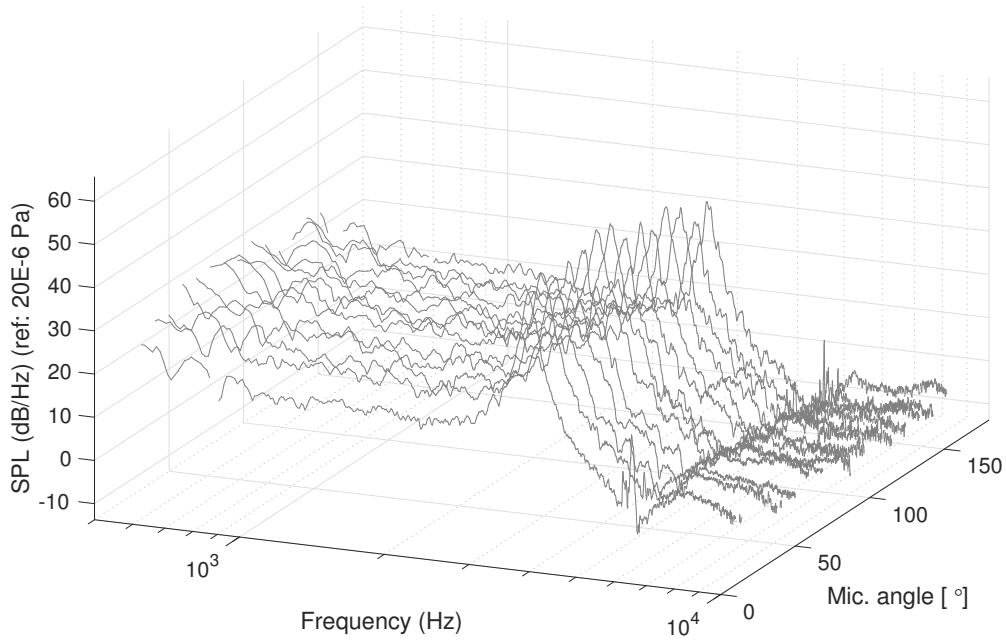


Figure 5.2: Example of tonal noise produced by the circular wing of at a free stream velocity of  $30\text{ m/s}$  (background subtraction is applied).

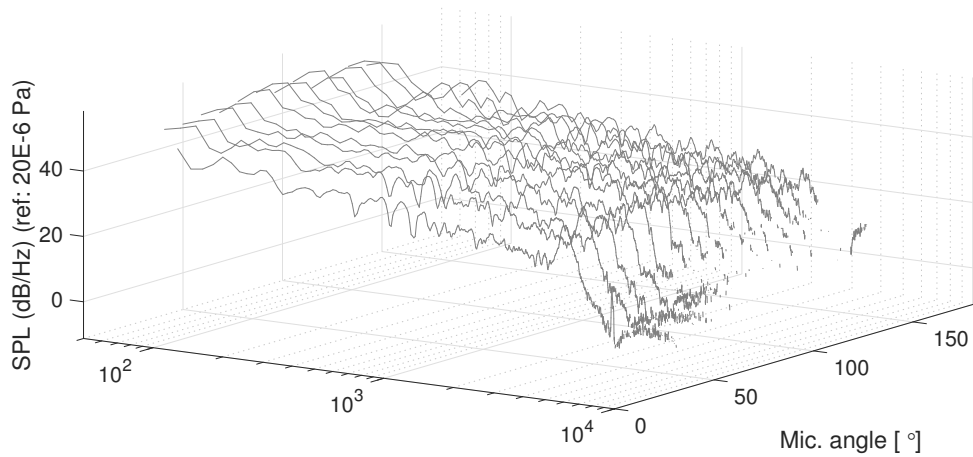


Figure 5.3: Example of broadband noise produced by the circular airfoil of  $d_w = 250\text{ mm}$  at a free stream velocity of  $30\text{ m/s}$  (background subtraction is applied).

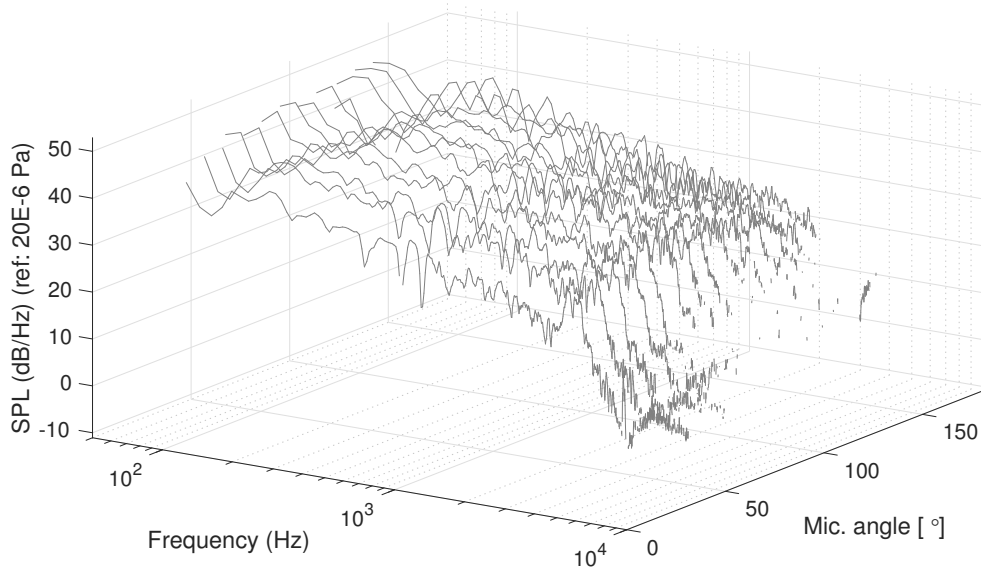


Figure 5.4: Example of broadband noise produced by the straight airfoil of  $s_w = 350 \text{ mm}$  at a free stream velocity of  $30 \text{ m/s}$  (background subtraction is applied).

An interesting phenomenon was reported by M. Roger Ref. [22]. He detects an increase in the sound pressure levels for approximately  $3.3 \text{ kHz}$  in his acoustic spectra. In the referenced work on circular airfoils it was noted that this could be the effect of acoustic reflection inside the circular airfoil itself since it did not seem dependent on the flow velocity. In this study we do find a similar phenomenon like this bump, however it is dependent on the velocity. Coincidentally for  $20 \text{ m/s}$  it is exactly at  $3.3 \text{ kHz}$  as is shown in Fig. 5.6. This bump was also found here for straight wings (see Fig. 5.7), so in this study we can conclude that the reflection phenomenon has not been found.

The “bump” found in the data here appears to correspond to the frequency where the tonal noise was observed during the measurements without any grids. The explanation here could be that this is caused by trailing edge noise. However the phenomenon appears to be also intermittent, in some data sets it does not appear. Additionally it is observed that when the wing does not interact with the shear layer at all, in the case of the circular wing with  $d_w = 150 \text{ mm}$  and the straight wing of  $s_w = 250 \text{ mm}$ , the probability of this phenomenon appearing in the data is drastically reduced. Concluding that either the turbulence intensity or the non-isotropic properties in this region is the cause of this state. Interestingly both causes are also present in the work of M. Roger: both higher  $TI$ , and shear layer turbulence. This phenomenon is worth investigating in more detail.

Using the different observation positions on the microphone array we can also plot the directionality of the acoustic signal. These results can also be compared to the noise predictions made by the model. An example of the data presented this way is shown in Fig. 5.5. The colors indicate the frequency bins over which the intensity is averaged. There appears to be no significant difference in up- or downstream radi-

ated noise intensity levels. Theoretically LE noise is supposedly more intense in the downstream direction.

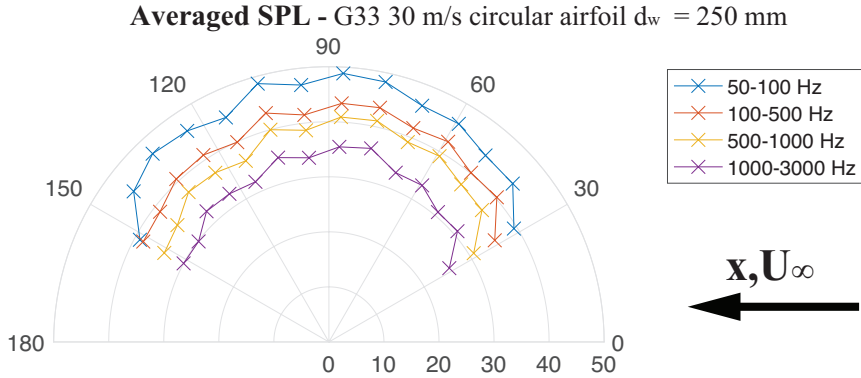


Figure 5.5: Directionality of the leading edge noise produced by the circular airfoil  $d_w = 250 \text{ mm}$ . The sound pressure levels shown in radial direction are the average SPL's over the given frequency domain. Configuration: Grid 2,  $30 \text{ m/s}$ .

## 5.2.2 Signal-to-noise ratio

Important in signal analysis of acoustic sources is the signal-to-noise ratio. For this type of experiment the signal-to-noise ratio is acceptable in the frequency range of 50 to approximately  $3000 \text{ Hz}$ . Beyond this the signal-to-noise ratio becomes less than  $3 \text{ dB}$ . This range depends on the free stream velocity, grid type, and microphone position and is therefore not easily defined. In Figs. 5.6 and 5.7 two examples are provided for the processed data, the difference between the red and purple line corresponds to the signal-to-noise ratio.

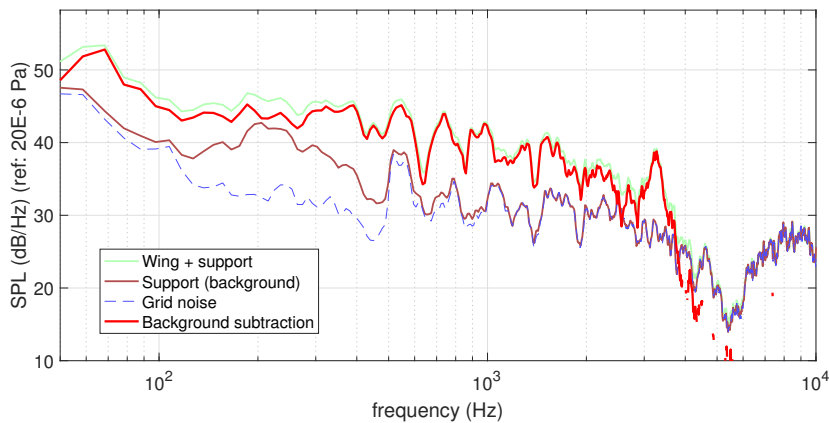


Figure 5.6: Signal-to-noise ratio for circular airfoil  $d_w = 250 \text{ mm}$ . Configuration: Grid 2,  $30 \text{ m/s}$ .

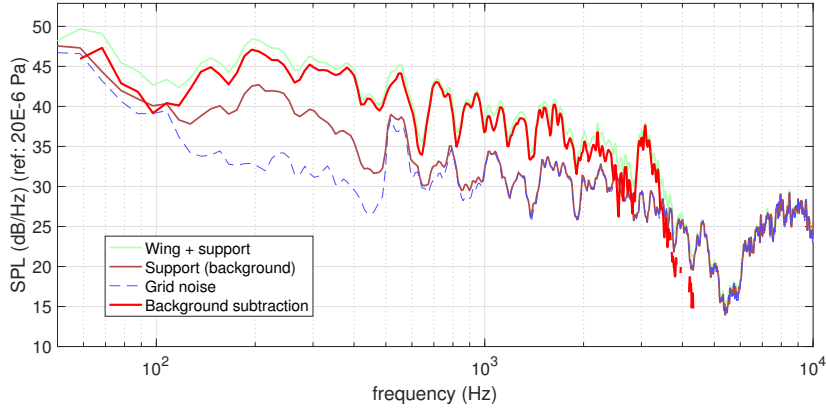


Figure 5.7: Signal-to-noise ratio for straight airfoil  $d_w = 250 \text{ mm}$ . Configuration: Grid 2,  $30 \text{ m/s}$ .

The signal-to-noise ratio shows a few general trends that are worth noting for future design of grids. Positive correlations are found for: lower flow velocities, higher grid solidity, higher turbulence intensities, and larger airfoils. The ratio for grid 3 (4x4) is already relatively bad over the entire frequency spectrum, making these results significantly more unreliable.

The sage of grids to generate the inflow turbulence has significant drawbacks with regards to the signal-to-noise ratio. The results for the higher grid solidities (grid 1 and 2) are similar to those obtained by both R.W. Paterson and R.K. Amiet [17], and L.D. de Santana [11] who employ similar techniques. The jet shear layer method employed by M. Roger is far superior in this regard but is less suitable for flat airfoils. However the wing is placed here in shear turbulence, which will affect the turbulence properties and statistics.

For the comparison with the prediction model any signal-to-noise ratio higher than  $1 \text{ dB}$  will be displayed. This signal-to-noise ratio is usually not considered to be sufficient. Generally a ratio of  $3 \text{ dB}$  is used, so keep this in mind when looking at the results.

### 5.2.3 Aeroacoustic scaling

Noise generated by aeroacoustic sources should behave according to the scaling laws determined for this phenomenon. The noise production should scale with the free stream velocity according to a sixth power law. This behavior is verified for all grid configurations. The results for three microphones of grid 2 are displayed in Figs. 5.8, 5.9, and 5.10. The angles corresponding to the microphone numbers can be found in appendix B.3. Based on these figures it is clear that the noise production collapses for the different velocities when this scaling is applied to the measurement data. For  $d$  required to calculate the Strouhal number, which is displayed on the  $x$ -axis of the figures, the chord length of the wings was used.

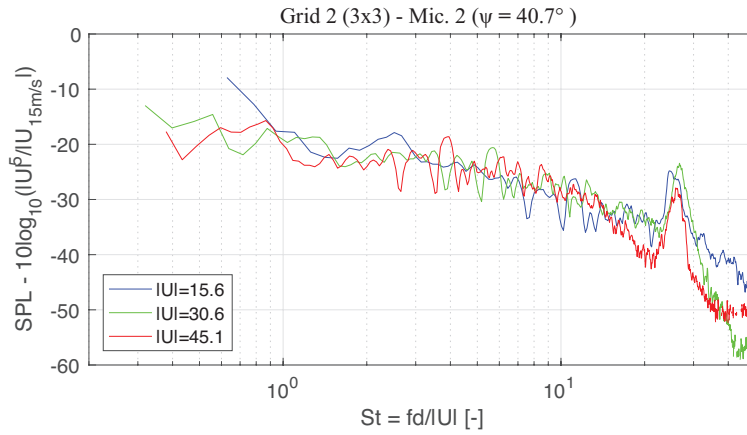


Figure 5.8: Collapse of acoustic spectra when scaled according to sixth power law. For the microphone at an angle of  $40.7^\circ$ .

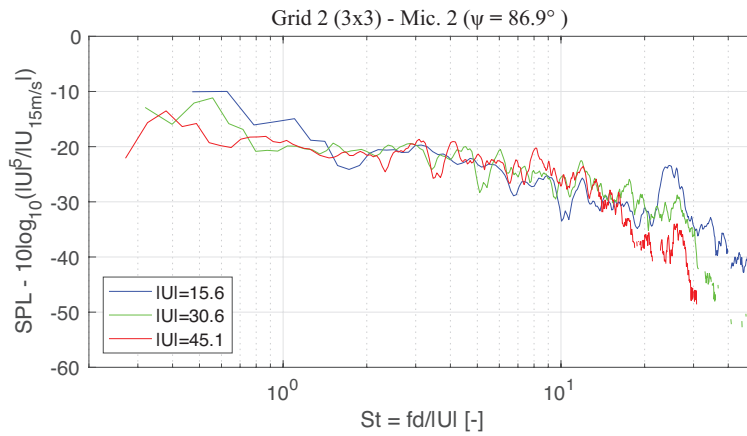


Figure 5.9: Collapse of acoustic spectra when scaled according to sixth power law. For the microphone at an angle of  $86.9^\circ$ .

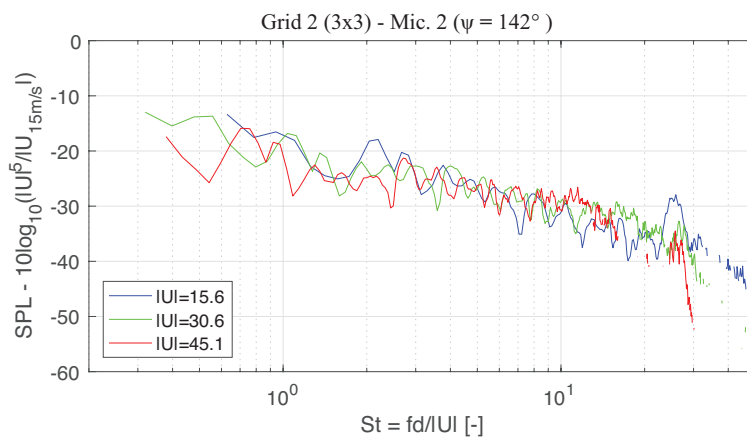


Figure 5.10: Collapse of acoustic spectra when scaled according to sixth power law. For the microphone at an angle of  $142.4^\circ$ .

These figures also indicate that around the point where the signal-to-noise ratio is equal to 1  $dB$  the noise recorded by the microphones no longer adheres to the aeroacoustic scaling laws. This indicates that this noise can definitely no longer be classified as leading edge (aeroacoustic) noise. Interesting to note is that for microphone 7, located near  $\psi = 90^\circ$  i.e. straight above the airfoil, the bump found to be corresponding to the trailing edge noise appears not to scale according to this relation.

### 5.3 SPL comparison for different wing types

In Figs. 5.11, 5.12, and 5.13 the acoustic signals from different wing types are compared. The images shown here are for grid 2 at 30  $m/s$ . Differences in intensity are provided quantitatively in Tab. 5.1, these results correspond to the figures shown in this section.

First consider the comparison between the circular wings and the flat plate wings shown in Fig. 5.11. The differences between these wings turn out to be small. In all cases the larger wing produces more noise, which is as expected.

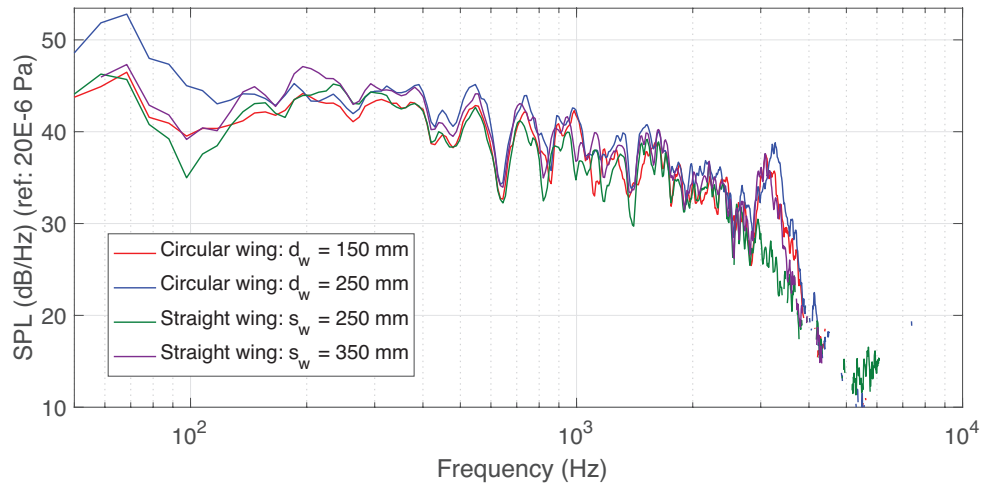


Figure 5.11: Comparison of the SPL's of the circular (V.) and the straight wings (I, and II).

Fig. 5.12 shows a comparison in noise levels for a straight airfoil and airfoils with a different sweep angle ( $\delta$ ). In the low-frequency domain there appears to be a significant difference. All swept airfoils produce significantly less noise in this frequency range. For higher frequencies there appears to be a small difference, it appears that in general the noise level is slightly lower for swept wings. This is corroborated by the results in Tab. 5.1. Note that the suspected trailing edge noise appears to be slightly lower also.

The final figure, Fig. 5.13, shows the comparison between the straight wing and the wings with a varying chord length. The results are very similar to those of the swept wing. For the trailing edge noise it appears that a larger variation in chord length leads to reduced trailing edge noise.

When compared to other velocities the results scale a little with the free-stream velocity but in general appear reasonably consistent. It appears that the differences found are genuinely the result of different wing types. However the differences are still very small and therefore might not be distinct enough to correlate to predictions made by the analytical models.

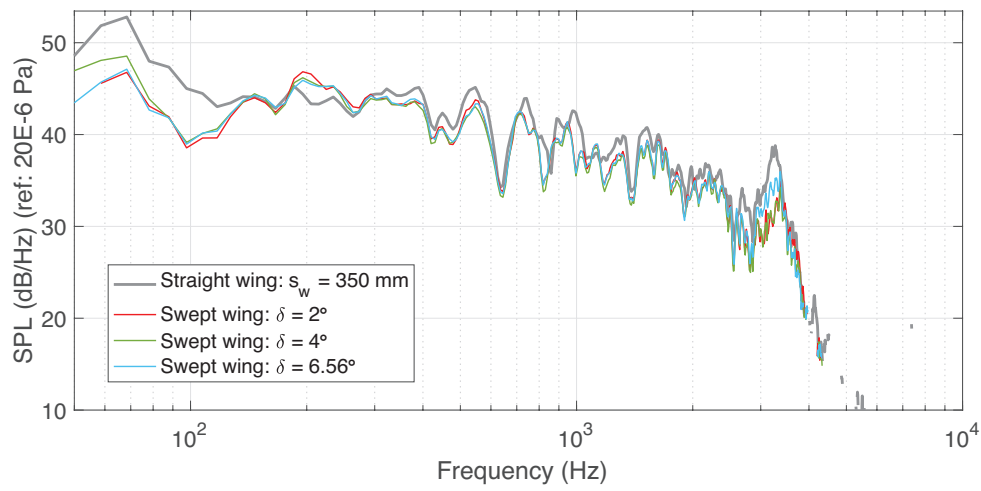


Figure 5.12: Comparison of the SPL's of the straight(I.) and the swept wings (III.).

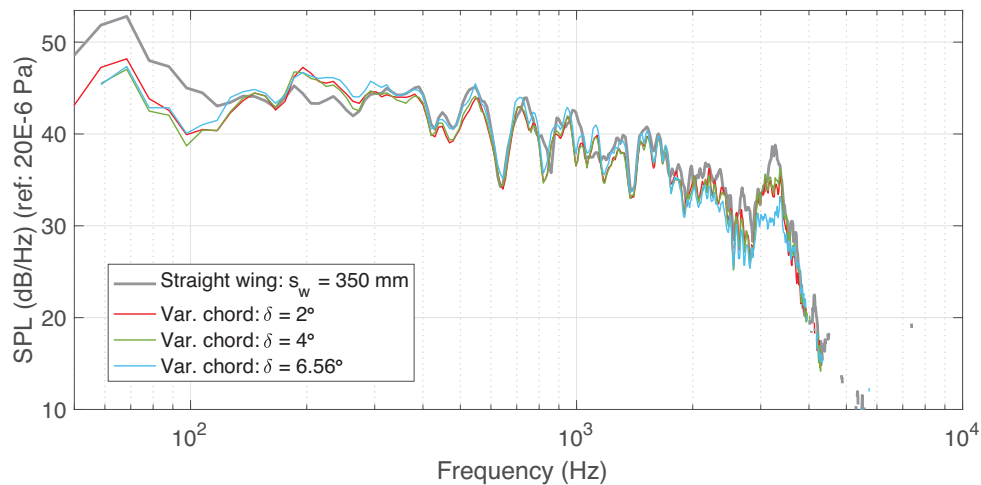


Figure 5.13: Comparison of the SPL's of the straight (I.) and the varying chord wings (IV.).

	50 - 100 Hz	100 - 500 Hz	0.5 - 1 kHz	1 - 3 kHz
<i>Circular wing</i>	6.58 dB	1.71 dB	1.68 dB	1.70 dB
<i>Straight wing</i>	1.52 dB	1.25 dB	1.78 dB	1.61 dB
<i>Str.-swept 4°</i>	-1.85 dB	0.67 dB	0.93 dB	1.56 dB
<i>Str.-v.c. 4°</i>	0.81 dB	0.24 dB	0.12 dB	0.76 dB

Table 5.1: Difference between SPL for different wing models for the specified frequency bins. For circular and straight wings this is large minus small. The SPL's are averaged over all microphones, i.e. for all observer angles. These results are for grid 2, at 30 m/s.

# Chapter 6

## Comparison of the Amiet model and experimental results

In this chapter the experimental results obtained in previous chapters are used to test the noise prediction capabilities of the Amiet model for circular and straight airfoils. The turbulence data, as presented in 4.1, is used to compute the  $\Phi_{ww}$  term in Eq. 2.15. Combining this with existing algorithms for the acoustic transfer function makes it possible to predict the noise levels at specific observer locations. These results will be compared to the acoustic experimental results as presented in Ch. 5.

In general it was found that grid 1 (2x2) and 2 (3x3) yielded the best results. Since there is still some doubt about the turbulence homogeneity and isotropy generated by grid 1, all results presented here are obtained using grid 2. However the results obtained using grid 1 are very similar to the results presented here, so it appears that the model works to the same extent for that grid. The results of grid 3 (4x4) show that for higher velocities the signal-to-noise ratio for higher frequencies was not enough to draw adequate conclusions. This causes larger errors towards the higher frequencies. For lower velocities the acoustic results appear to match well with those produced using the other grids.

### 6.1 Intensity and spectral comparison

#### 6.1.1 Circular wing

In Figs. 6.1, 6.2, and 6.3 the acoustic spectra are shown for three observer angles: one above the inlet nozzle ( $\psi = 40.7^\circ$ ), one straight above the airfoil ( $\psi = 86, 9^\circ$ ), and one near the outlet of the anechoic chamber ( $\psi = 142.4^\circ$ ). Each figure is for a different free stream velocity. In addition to the experimental data shown, the respective predictions are indicated in the identical color using a dashed line.

Judging from these figures we see that for the circular airfoil the match is very good in the low frequency regime. For frequencies greater than 1  $kHz$  the experimental results show greater intensity compared to the predictions. This effect appears to get worse for higher free stream velocities.

Interestingly enough the largest variations appear for the smallest observation angles. Beyond a frequency of 1 kHz the experimental data is much too high in all cases. This effect appears to be proportional to the free stream velocity also. This could be the effect of trailing edge noise in some fashion, especially since it is directed backwards. The exact cause however is unknown.

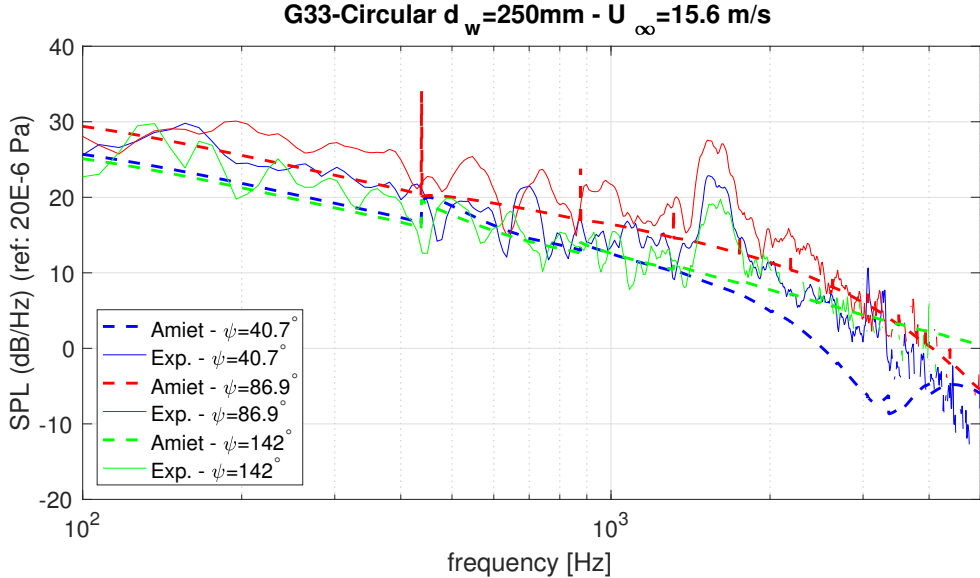


Figure 6.1: Theoretical noise predictions compared with the corresponding experimental results for three observer positions.

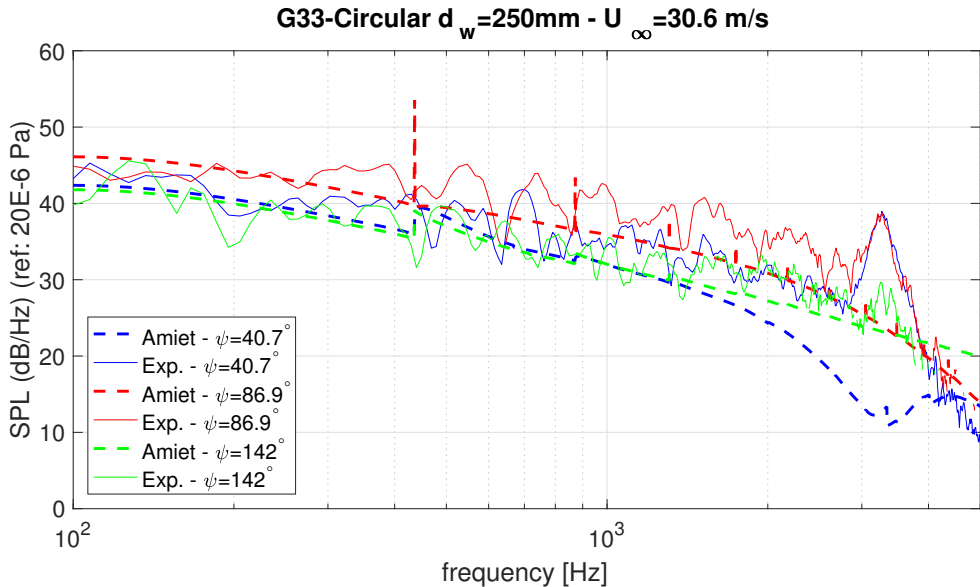


Figure 6.2: Theoretical noise predictions compared with the corresponding experimental results for three observer positions.

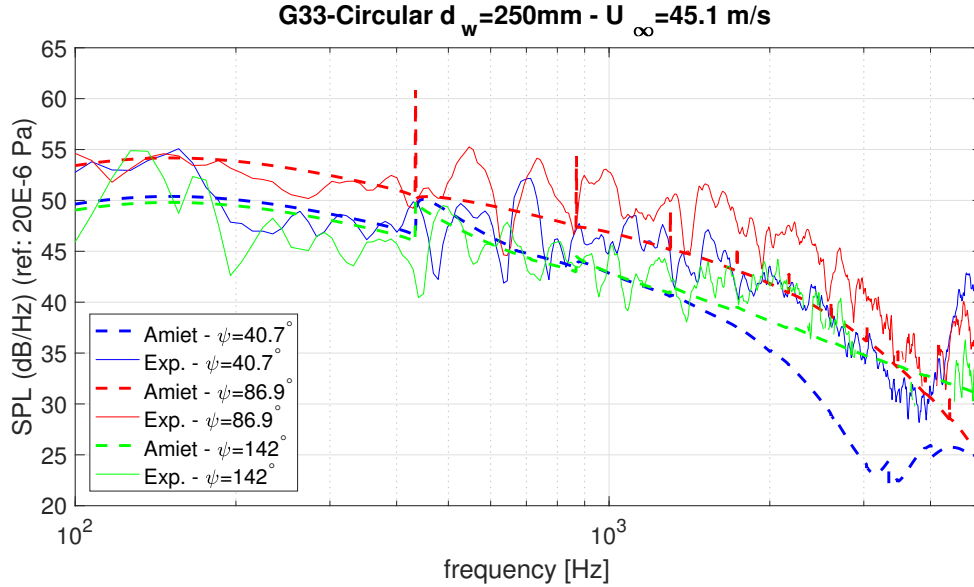


Figure 6.3: Theoretical noise predictions compared with the corresponding experimental results for three observer positions.

### 6.1.2 Straight wing

In Figs. 6.4, 6.5, and 6.6 the acoustic spectra are again shown for the same three observer angles at different free stream velocities. Here the acoustic spectra and noise predictions are however for the straight airfoil with a span length  $s_w = 350 \text{ mm}$ . Again the dashed line indicates the noise prediction corresponding to the continuous line of the corresponding color.

The general trends are the same as for the circular wing. The match for low velocities and lower frequencies is good, not as good as for the circular airfoil however. For high frequencies we again see the deviation between experiment and model developing. Again for high frequencies and small observer angles the drop in SPL predicted is not observed in the experiments.

An additional phenomenon visible in these results is the low frequency drop in SPL found in the experimental data. This is not predicted well by the semi-analytical model. Some correction models have been developed to better predict this effect (see the work of L.D. de Santana [11] *Ch.5: Extension of the Amiet theory to the low-frequency regime*).

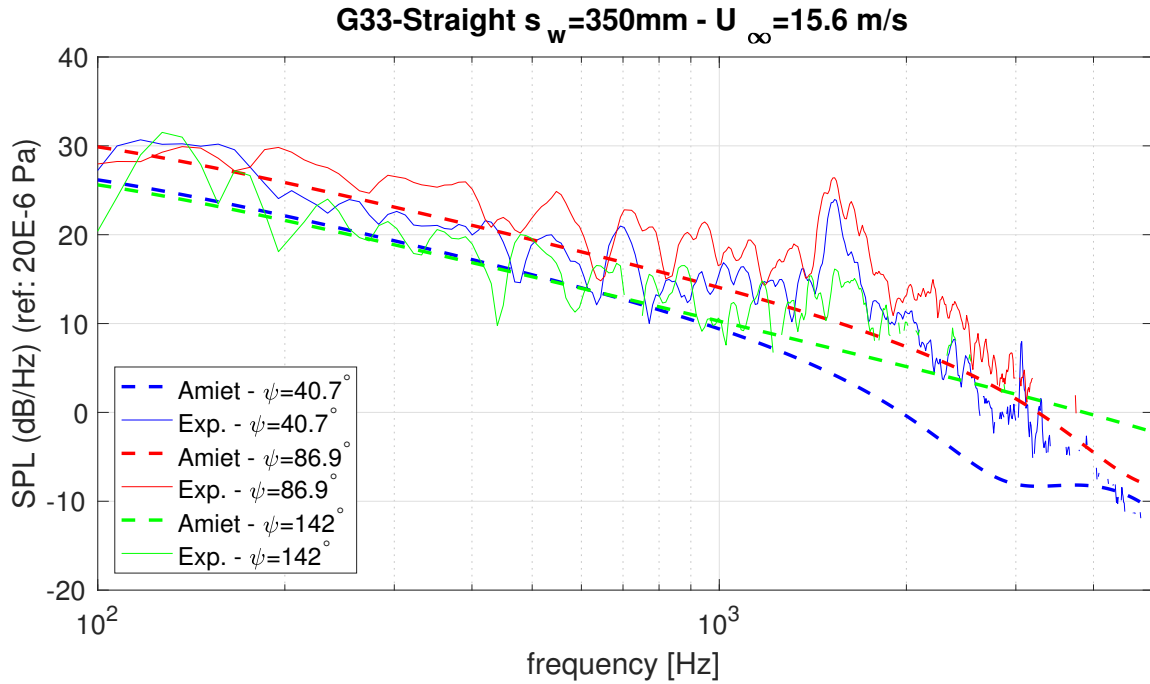


Figure 6.4: Theoretical noise predictions compared with the corresponding experimental results for three observer positions.

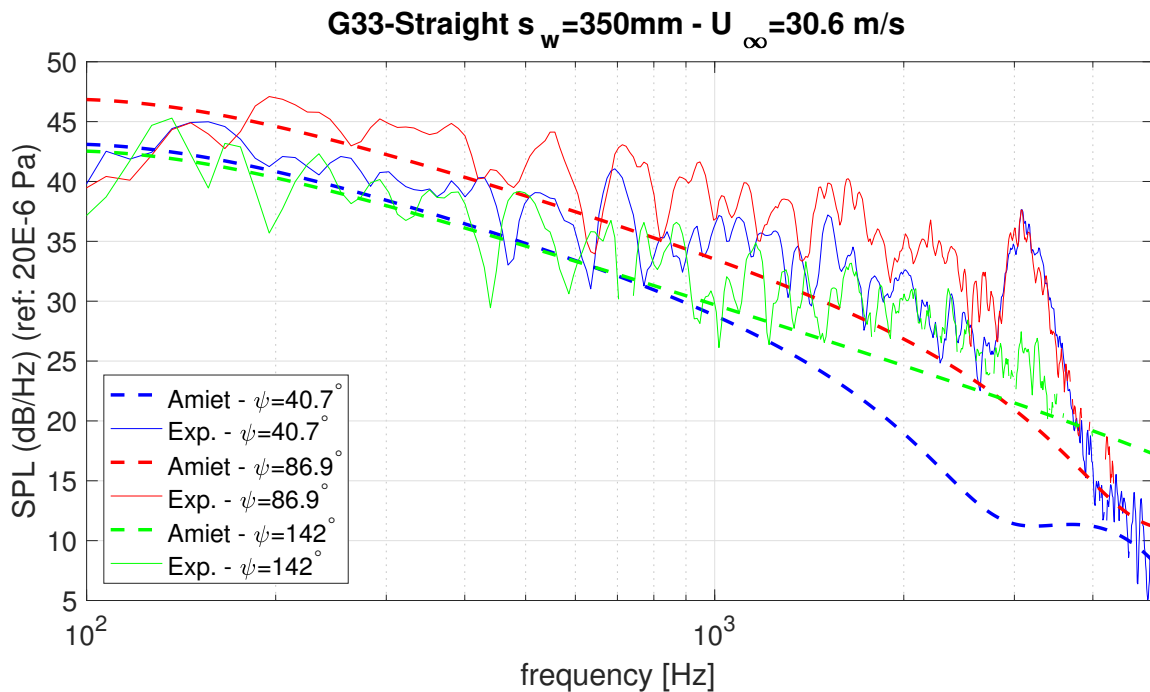


Figure 6.5: Theoretical noise predictions compared with the corresponding experimental results for three observer positions.

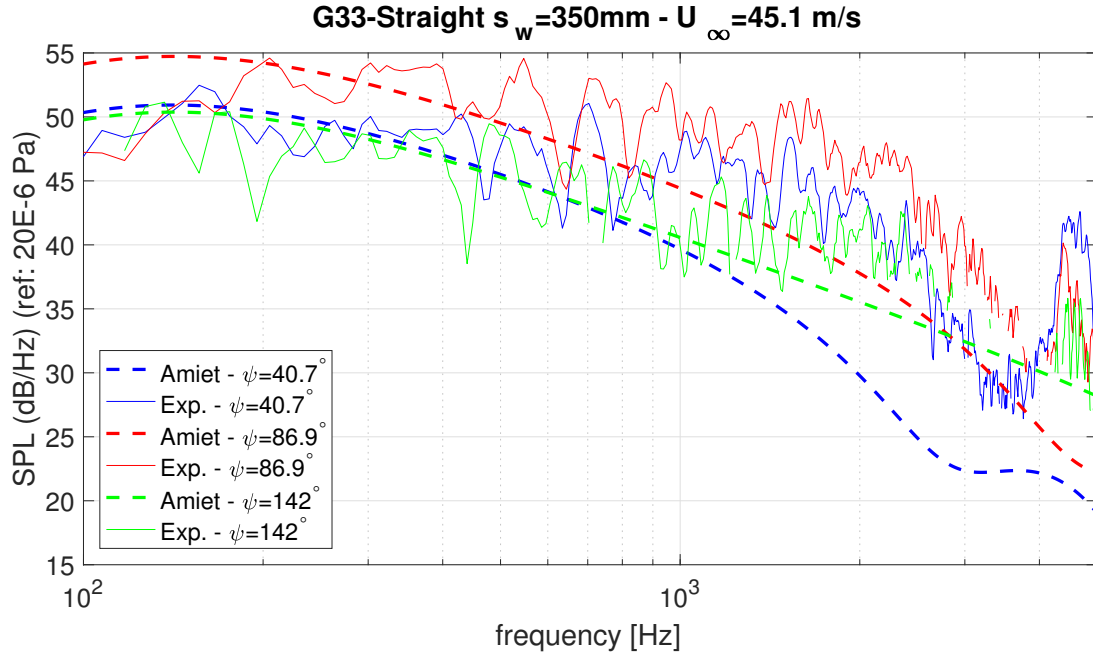


Figure 6.6: Theoretical noise predictions compared with the corresponding experimental results for three observer positions.

## 6.2 Comparison of the directionality

### 6.2.1 Circular wing

In Figs. 6.7, 6.8, and 6.9 the directionality of the acoustic signals is compared to the predictions made by the Amiet model for circular wings. The left part of the figures shows the SPL's for each observer, and the right part the absolute difference in  $dB$  between the experimental results and the predictions. The color of the lines corresponds to frequency bins as defined in the figure's legend. The radial direction shows the SPL's averaged over the frequency bins for the experimental results (solid line) and the predictions (dashed line). The angular direction corresponds to the observer angle ( $\psi$ ). The flow direction in these figures should be seen as from the right to the left, i.e. the small observer angles are in the upstream direction.

For the low velocities of around  $15\text{ m/s}$ , Fig. 6.7, the match is good in general. It is observed that the results around  $\psi = 80^\circ$  are underpredicted for all frequency ranges, though the effect is more pronounced for high frequencies. This upstream phenomenon is the main source of the error in the predictive model. This can also be observed from the right hand side of the figures, the absolute error between the two. Another effect is observed for the large angles approaching  $\psi = 151.6^\circ$ . Here the drop in predicted acoustic intensity is not found in the experimental results.

For the intermediate flow velocity  $30\text{ m/s}$ , shown in Fig. 6.8, the results are similar. The predictive capability of the model is good, the trends in the radiated noise are accurately described. Again for the higher frequencies the intensity of the sound radiated upstream is underpredicted. The effect described for the measurements at  $15\text{ m/s}$ , the drop in in SPL for larger angles, is no longer observed here.

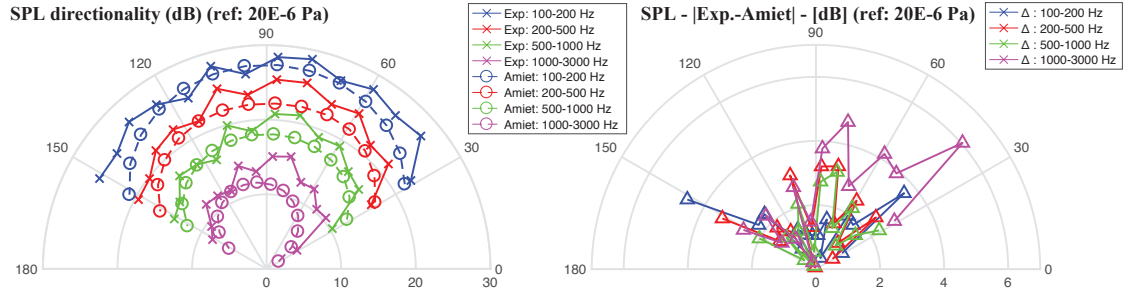


Figure 6.7: Directionality results for the circular airfoil of  $d_w = 250$  [mm] grid 2 (3x3) at approximately  $15$  [m/s].

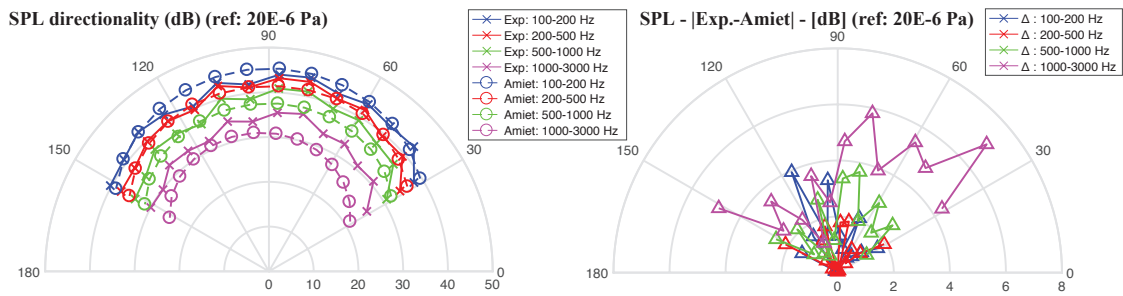


Figure 6.8: Directionality results for the circular airfoil of  $d_w = 250$  [mm] grid 2 (3x3) at approximately  $30$  m/s.

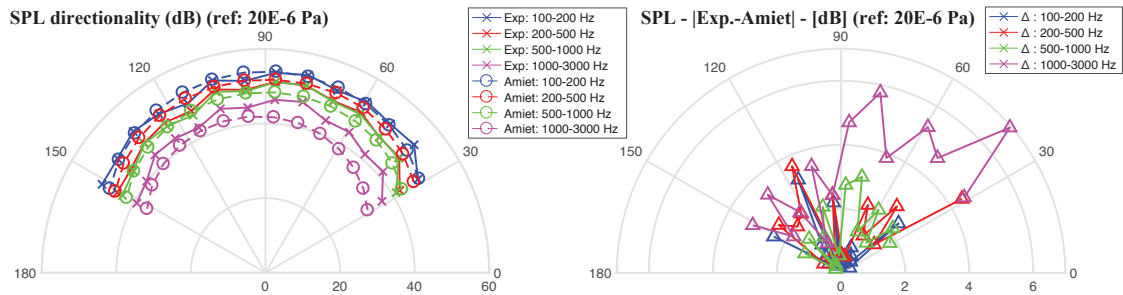


Figure 6.9: Directionality results for the circular airfoil of  $d_w = 250$  [mm] grid 2 (3x3) at approximately  $45$  m/s.

For the highest free stream velocity  $45$  m/s, Fig. 6.9, the results are again good in regard to both the noise levels and the trends in directivity. The high frequency phenomenon is again clearly visible. Important to note is the fact that the error between experiment and the Amiet model remains relatively small and the error does not appear to be affected by the free stream velocity. This implies the error is consistent. Most likely this can be improved by alterations to the model, which is promising.

Something that is also very interesting to note is the fact that the error in the frequency bin  $1$  kHz -  $3$  kHz is very consistent between the three different flow velocities for angles around  $\psi = 60^\circ$ . This suggest that this is not a statistical

anomaly but an actual effect of noise generated by the airfoil. The directionality of this effect can clearly be seen when comparing the right hand side of the three figures. Again this suggest the presence of some sort of noise source radiating upstream, perhaps trailing edge noise.

## 6.2.2 Straight wing

In Figs. 6.10, 6.11, and 6.12 the directionality of the acoustic signals for the straight airfoil, span  $s_w = 350 \text{ mm}$  is shown. The results are displayed identically to those of the circular airfoil.

The results shown in Fig. 6.10 are for a measurement velocity of  $15 \text{ m/s}$ . When compared to the results of the circular wing they seem similar with one exception: the noise radiated in upstream direction for the highest frequency bin,  $1 \text{ kHz} - 3 \text{ kHz}$ , is slightly larger. The prediction of the model matches quite closely to the experimental results. The errors for lower frequencies are all under the  $5 \text{ dB}$  level for all observer angles. Note that also here the drop in intensity for low frequencies near  $\psi = 151.6^\circ$  is not observed.

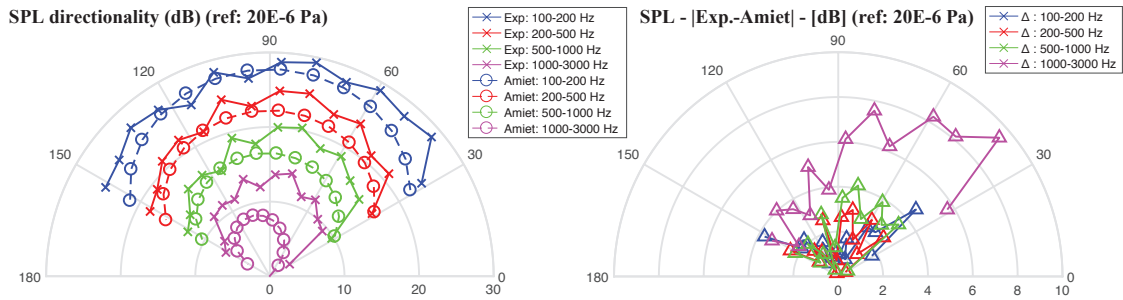


Figure 6.10: Directionality results for the straight airfoil of  $s_w = 350 \text{ [mm]}$  grid 2 (3x3) at approximately  $15 \text{ m/s}$ .

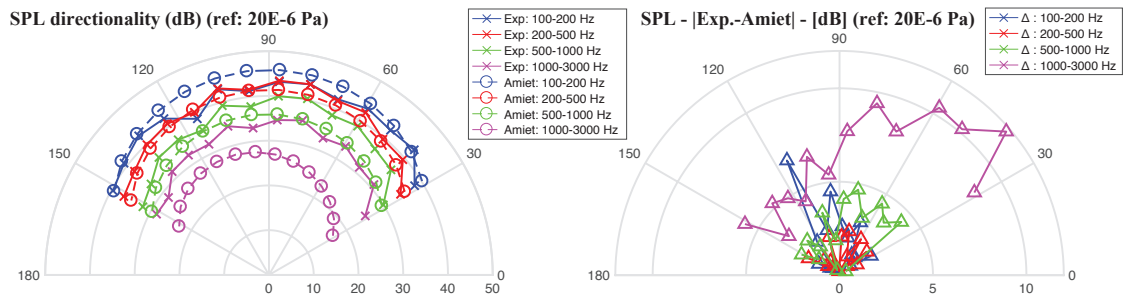


Figure 6.11: Directionality results for the straight airfoil of  $s_w = 350 \text{ [mm]}$  grid 2 (3x3) at approximately  $30 \text{ m/s}$ .

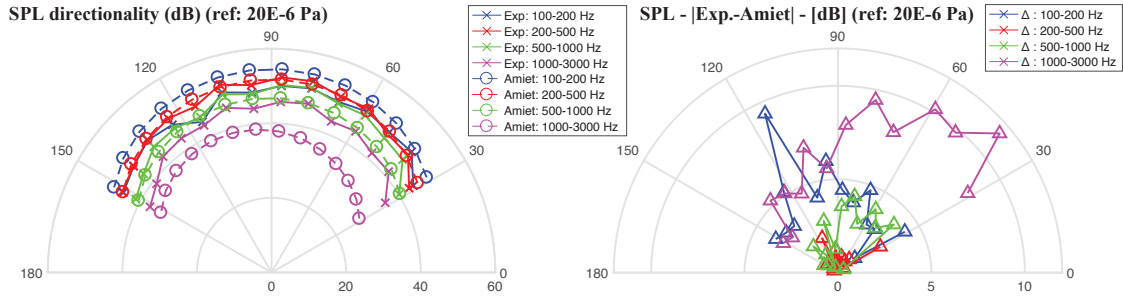


Figure 6.12: Directionality results for the straight airfoil of  $s_w = 350$  [mm] grid 2 (3x3) at approximately  $45$  m/s.

For the higher velocities  $30$  and  $45$  m/s the results are shown respectively in Figs. 6.11, and 6.12. In the frequency range  $100$  Hz -  $1$  kHz the results match closely. For high frequencies the upstream deviation is clearly visible. This high frequency error in directionality is again very consistent for the different flow speeds. In these results however the low-frequencies do not match nearly as well. For the highest flow velocity there is a large drop in SPL for this frequency range, mainly located in downstream direction. See the right plot in Fig. 6.12. Corrections can be applied to model this phenomenon. The fact that this is observed is meaningful since it indicates that the setup can be used to discover this type of behavior and test the algorithms designed to correct for it.

### 6.2.3 Additional configurations

In order to show the consistency of the model the directionality results for the circular wing of  $d_w = 180 \text{ mm}$  and for the straight wing of span  $s_w = 250 \text{ mm}$  are shown in Figs. 6.13, and 6.14 respectively. The results are very similar to those for the larger variants of the wings. The errors follow the same trends especially for the flat plate airfoil. Overall the errors between prediction and experimental results are slightly larger for the smaller versions of the airfoils. The most significant deviation is noted in the results for the circular airfoil, here the SPL in the  $1 \text{ kHz} - 3 \text{ kHz}$  domain is increased for all observation angles in the experimental data, this was not the case for the larger versions of the straight and circular airfoils.

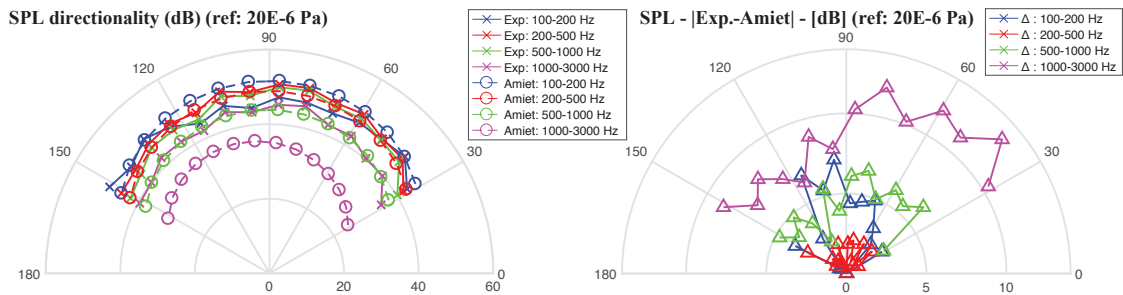


Figure 6.13: Directionality results for the circular airfoil of  $d_w = 180 \text{ mm}$  grid 2 (3x3) at approximately  $45 \text{ m/s}$ .

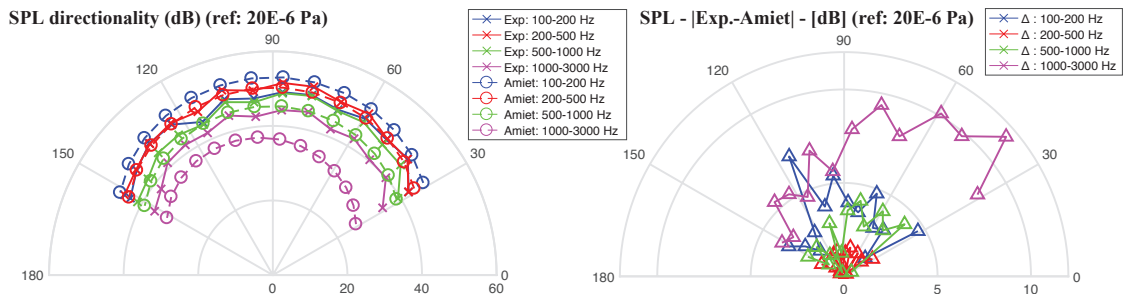


Figure 6.14: Directionality results for the straight airfoil of  $s_w = 250 \text{ mm}$  grid 2 (3x3) at approximately  $45 \text{ m/s}$ .

# Chapter 7

## Conclusion and recommendation

### 7.1 Turbulence generation and characterization

In this research the effects of solidity of passive turbulence grids has been examined for the purposes the generation of isotropic turbulence and silent operation for acoustic measurements. A wind tunnel section and three, interchangeable, turbulence grids have been designed and constructed which can generate turbulence levels ranging from 5-7 percent. The developed grids have a very high solidity, i.e. little blockage, and generate turbulence spectra which are viable for use in acoustic noise prediction. The range of obtained turbulence levels is limited (lower than the desired 5-15 percent). This was the result of a compromise between a wide range in turbulence intensities (low solidity:  $\sigma^* < 0.5$ ) and a good acoustic signal-to-noise ratio (high solidity:  $\sigma^* > 0.5$ ). It was found that for high solidity grids the turbulence intensity does not change much for different amounts of channel blockage.

Using Constant Temperature Anemometry (CTA) and a two-wire probe the axial and transverse velocity component and the turbulence statistics in both directions could be obtained. An experimental setup was constructed using a 2D traverse system to measure planes perpendicular to the axial  $x$ -direction. Four planes in  $x$ -direction were examined located at 1, 1.2, 1.4, and 1.65  $m$  downstream of the turbulence grids. Each  $y$ - $z$  plane is subdivided in a 25  $mm$  by 25  $mm$  measurement grid, resulting in the full characterization of the velocity and turbulence fields in front of the inlet nozzle. This data was obtained for three velocities, 15, 30, and 45  $m/s$ , and for the three turbulence grids and the case of no grid. Thus the homogeneity of the field is verified and the optimal location for the airfoils was chosen.

Using the same setup longer duration CTA measurements were performed in order to obtain the turbulence spectra and autocorrelation functions. These measurements were performed for positions where the leading edge of the airfoil would be located. The generated turbulence spectra and autocorrelation function were found to match well with the von Kármán model for isotropic turbulence. Using these measurements the averaged turbulence intensity and integral length scale for all wing types could be determined. These properties in combination with the mean free stream velocity on the wing were used in the von Kármán model to reconstruct the spectrum for acoustic noise prediction.

The integral length scale was found to be consistent between all measurements. This was in line with expectations since theory suggested it to be dependent on the rod diameter in the grids. Only for grid 1 at 15  $m/s$  it varied significantly, no explanation for this was found. The ratios between the axial and transverse components of both the turbulence intensity and the integral length scale is a measure for isotropy. These ratios deviate from the theoretical values, the results are in line with results obtained by other authors for generated passive grid turbulence.

The turbulence results were corroborated using Particle Image Velocimetry (PIV). The CTA data for the turbulence intensity matched well with the results obtained from the PIV. For the integral length scale a consistent difference of a factor 1.5 was found in the results. This error is still unexplained. The PIV setup was also used to examine the upstream influence on the turbulence spectrum to verify the assumption that this remains largely unaffected. A slight alteration in statistics was found though it turned out to be insignificant in the spectral reconstruction.

## 7.2 Acoustics measurements and validation of the Amiet model

An experimental setup was designed and built, capable of capturing the intensity and directionality of leading edge noise radiated from different airfoil shapes. A mounting structure and ten wings were constructed. These wings have been tested for all flow conditions. By recording background noise from the support and subtracting this from the wing signal we were capable to determine differences in airfoil shape, sweep angle, and variations in chord length. The effects are small however are consistent in their occurrence and therefore significant.

To validate the semi-analytical model the measured Sound Pressure Levels (SPL) were compared to the values predicted by the Amiet model. The model was programmed in MATLAB for both straight airfoils and circular ones. The flow field properties and reconstruction of the turbulence spectrum were based on experimental data obtained from the turbulence measurements.

For two circular and two straight airfoils the acoustic spectra and directionality was compared with the Amiet theory for leading edge noise prediction. The results matched closely for frequency ranges up to 1  $kHz$ . Intensity was in almost all cases within a 5  $dB$  margin. The trends in directionality of the noise in the experimental data was well described by the model. Beyond this frequency very significant differences depending on the flow velocity were detected, suggesting the presence of trailing edge noise. This explanation still needs to be corroborated. Additionally for straight airfoils deviations were found in the low frequency range, something the general model also does not capture well.

These results are mainly positive since it shows the setup is capable of capturing these phenomena. This implies that the setup is capable of delivering experimental results which can be used to compared with theoretical predictions. Improvements can thus be made to the model which can than be validated using this or a similar

setup, resulting in models for increasingly complex airfoil types and configurations.

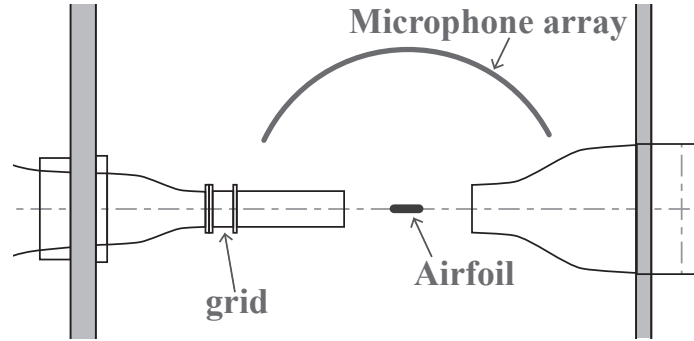


Figure 7.1: Possible improvement in the experimental acoustic setup.

### 7.3 Recommendations

The setup developed in this thesis is able to generate good experimental acoustic data for leading edge noise. The developments made here allow for additional testing to extend and test different aspects of the Amiet model. A lot was learned designing, building, and operating this setup and many improvements can be made because of it. Some practical considerations which will lead to better results are presented here:

- In order to obtain more variation in the intensity of the generated turbulence new techniques should be considered. The generation must be as silent as possible since this will affect the signal-to-noise ratio obtained during the measurements. For the current grids this is stretching the limits already for the lower solidity grids. One option is to use shear layer turbulence as similar to M. Roger [22]. A concept that can be tried is a shear layer nozzle for flat wings as shown in Fig. C.1 in appendix C. This could possibly produce high intensity shear layer turbulence for a flat plate wing whilst minimizing noise production. Other options are active grids as described in appendix C. Caveat: for active grids testing must be preformed in order to see if it can be done without causing noise to be radiated towards the microphones.
- The anechoic chamber has been shown to work well in reducing noise reflections. However it was found that, especially at higher velocities, a lot of noise is generated by the flow buffeting the walls of the chamber near the outlet. It could be beneficial to extend both the inlet and the outlet towards the center of the chamber as depicted in Fig. 7.1. This would prevent a lot of ambient noise contaminating the signal. The effects on the shear layer growth and thickness in this case are also interesting.
- Increasing the distance between grid and airfoil could reduce the noise generated by the grid reaching the observer positions. This could be especially useful for active turbulence generation. This approach will reduce the turbulence intensity reaching the wing. This is not necessarily a problem if the

generated turbulence has a much higher intensity directly behind the grid. In addition this would benefit the isotropy of the turbulence, especially if a small contraction is placed after the grids. This has been found beneficial by G. Comte-Bellot and S. Corrsin Ref. [8].

- In this thesis only one of the transverse flow components was measured using CTA, the isotropy of the two transverse components was tested using PIV. In the future it might be beneficial to obtain both using CTA. This could be relevant since the nozzle size does not allow for equal spacing of the rods for the turbulence grids. Theoretically this should not matter since it will decay to isotropic turbulence. It is worth corroborating this fact using CTA.
- In order to reach the desired flow velocities when using turbulence grids a contraction was placed before the grids in order to accelerate the air. This contraction in the current setup is highly inefficient. The cross section is reduced four fold yet the maximum velocity only increases from 60  $m/s$  to approximately 80  $m/s$ . A smaller contraction could be constructed which would allow larger wings to be mounted, thus increasing the signal to noise ratio.
- Currently the wings are mounted in clamps that are located in the flow. For background subtraction the noise of the clamps in the flow is used, however the noise of the clamps interacting with the wing is not considered. This could result in contamination of the signal. This effect is difficult to test. An attempt can be made by using side plates to mount the wings instead, the difference in results should provide some insight into this. This should also remove any tip noise, if at all present. During these the acoustic experiments it was assumed that for an angle of attack of zero no tip noise was being generated because there are no large constant pressure differences between the top and bottom of the airfoils.

# Appendix A

## List of symbols

Symbol	Dimension	Description
$\alpha$	[°]	Angle of attack of the airfoil.
$\beta$	[−]	Compressibility factor defined as: $\beta = \sqrt{1 - M^2}$ .
$\delta$	[°]	Sweep angle of the leading edge (and for varying chord trailing edge) of the airfoil.
$\kappa$	[−]	Characteristic term in the Helmholtz equation, defined as $\kappa^2 = \mu^2 - \bar{k}_y M / \beta^2$ .
$\lambda_i$	[m]	Acoustic wave length
$\Lambda_i$	[m]	Taylor or integral length scale of turbulence.
$\mu$	[−]	Compressibility parameter, defined as: $\mu = \bar{k}_x M / \beta^2$ .
$\phi$	[m <sup>2</sup> /s]	Harmonic scattered (near field) flow potential function.
$\Phi_{ii}$	[U <sup>2</sup> s]	Power spectral density function of velocity signals.
$\psi$	[°]	Observer or microphone angle. Angle around the $y$ -axis starting from the negative $x$ -axis.
$\Psi$	[m <sup>2</sup> /s]	Scattered (near field) flow potential function.
$\rho$	[kg/m <sup>3</sup> ]	Density of air.
$\rho_p$	[kg/m <sup>3</sup> ]	Density of PIV particles.
$\rho_{ii}$	[−]	Normalized autocorrelation function of velocity signals.
$\sigma_s$	[m]	Distance between source and observer accounting for compressibility.
$\sigma_t$	[m]	Wave propagation distance corrected for compressibility.
$\theta$	[°]	Angle of the incoming flow in the horizontal plane.
$\omega$	[rad/sec]	Angular frequency.

Symbol	Dimension	Description
$a_w$	[ $m$ ]	Airfoil wing half span length.
$b_w$	[ $m$ ]	Airfoil wing half chord length.
$c_0$	[ $m/s$ ]	Speed of sound in air.
$c_w$	[ $m$ ]	Airfoil wing chord length.
$C$	[ $1/s$ ]	Characteristic frequency of particle motion.
$d_p$	[ $m$ ]	Particle diameter for PIV measurements.
$d_r$	[ $m$ ]	Grid rod diameter in transverse flow direction.
$d_w$	[ $m$ ]	Circular wing diameter.
$e$	[ $m$ ]	Initial chord length of the varying chord airfoils.
$E_i$	[ $V$ ]	Voltages applied to the hot-wire wires.
$f$	[ $1/s$ ]	Frequency.
$i$	[ $-$ ]	Imaginary number defined as: $i = \sqrt{-1}$ .
$J_{ix}$	[ $s$ ]	Integral time scale of turbulence.
$k$	[ $rad/m$ ]	Acoustic wave number defined as $\omega/c_0$ .
$k_i$	[ $rad/m$ ]	Wavenumber in Cartesian direction.
$\bar{k}_i$	[ $-$ ]	Normalized wavenumber ( $\bar{k}_i = k_i b$ ).
$k_e$	[ $rad/m$ ]	Characteristic wavenumber corresponding to the energy-containing eddies.
$K_x$	[ $rad/m$ ]	Chordwise specific wavenumber $\omega/U_\infty$
$K_y$	[ $rad/m$ ]	Spanwise specific wavenumber $y/\sigma_0 k$
$M_h$	[ $m$ ]	Horizontal grid spacing.
$M_v$	[ $m$ ]	Vertical grid spacing.
$s_w$	[ $m$ ]	Airfoil wing span length.
$ST$	[ $m$ ]	Strouhal number, dimensionless number relevant for oscillating flow mechanisms.
$t$	[ $s$ ]	Time.
$T_i$	[ $-$ ]	Turbulence intensity direction of index $i$ .
$T_{ij}$	[ $-$ ]	Turbulence isotropy parameter $T_j$ over $T_i$ .
$t_w$	[ $m$ ]	Thickness of the airfoil.
$\vec{u}$	[ $m/s$ ]	Velocity vector of fluid flow consists of three velocity components designated by either $\{u, v, w, \}^T$ or $u_i$ where $i = 1, 2, 3$ .
$u'_i$	[ $m/s$ ]	Root mean square value of velocity component $u_i$ .
$U_\infty$	[ $m/s$ ]	Time and spatial averaged flow velocity in axial direction of the main channel.
$x_l$	[ $m$ ]	Spacial lags for in autocorrelation of turbulence spectral measurements.
$\vec{x}_o$	[ $m$ ]	Observer position vector.
$\vec{x}_s$	[ $m$ ]	Position vector to point on the airfoil surface.
$\vec{x}_t$	[ $m$ ]	Relative position vector between source and observer corrected for compressibility effects.

Table A.1: List of all symbols and parameters used in this report.

# Appendix B

## Experimental process

### B.1 Wind tunnel - frequency velocity diagram

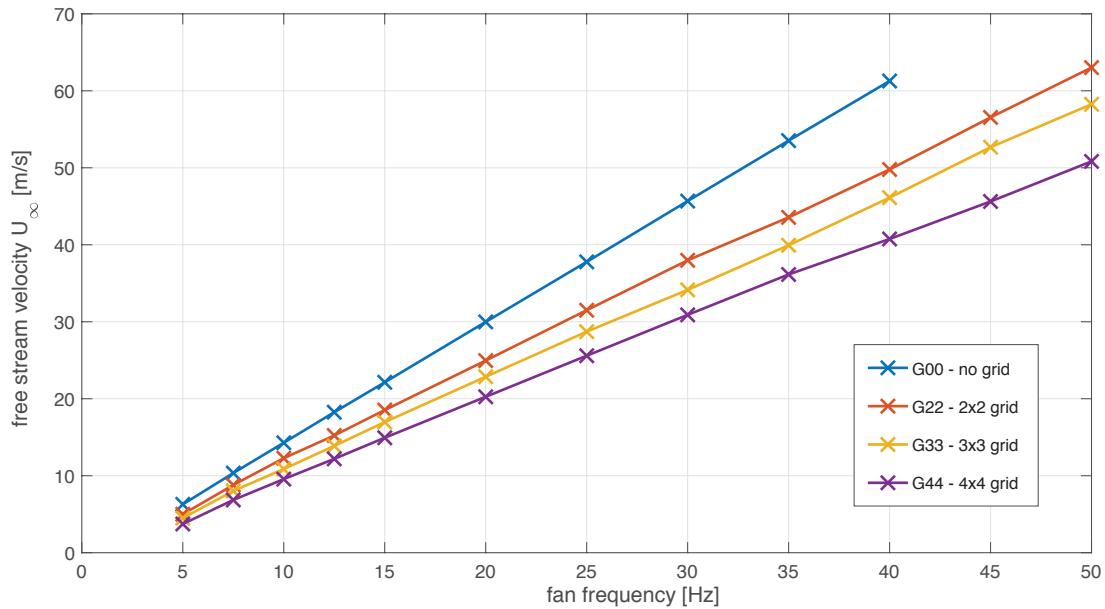


Figure B.1: Settings of the wind tunnel and the corresponding free stream velocity measured using the Pitot tube in the designated position. This position is used in all experiments to set the wind tunnel to the desired velocity in order to maintain consistent results.

## B.2 Unfiltered turbulence spectral measurements

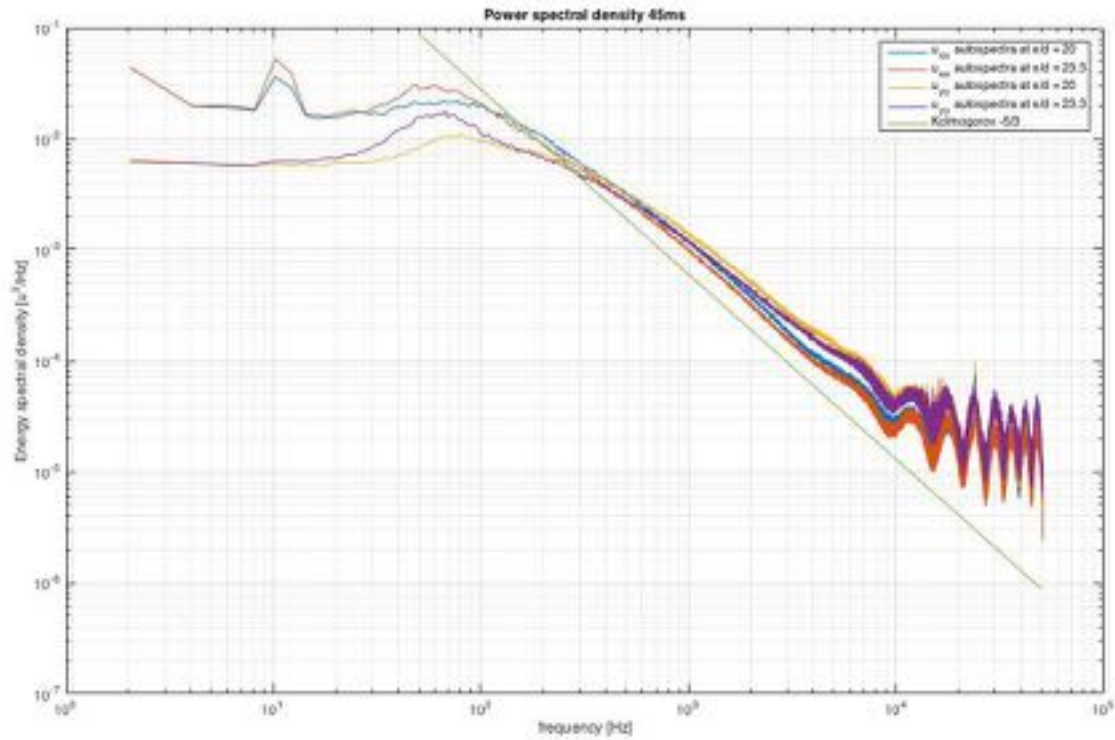


Figure B.2: Example of high frequency oscillations of the turbulence spectra in x- and y-directions. These measurements are for grid 2 (3x3) at 45 m/s. For each spectral direction two positions in x-direction are plotted corresponding to the position of the leading edge and just behind the trailing edge.

## B.3 Microphone array positions

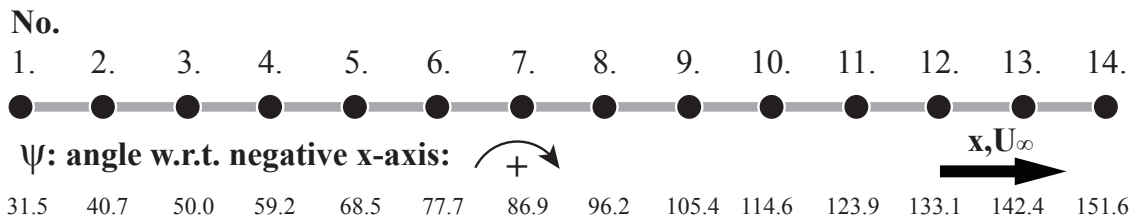


Figure B.3: The angle in degrees around the  $y$ -axis starting from the negative  $x$ -axis corresponding to the microphone numbers:

# Appendix C

## Optimization of the turbulence grid design

### C.1 Grid types and considerations

The first distinction that is made in the choice of grid is active versus passive grids. Active grids will add momentum into the flow field therefore producing higher levels of turbulence ([15],[4]), passive grids rely on the energy contained in the flow to generate the turbulence. Active grids thus have two major advantages; they generate higher turbulence intensities ( $TI_i = u'_i/U_\infty$ ), and secondly they have a lower pressure reduction and thus higher flow velocities behind the grid. The downside however is that they are more complex to construct and require a lot of time to adjust to generate isotropic and homogeneous turbulence. The passive grids on the other hand are easier to design, implement, and construct but still multiple designs might be required to obtain an adequate turbulent flow field.

Directly behind a grid the flow will not be homogeneous or isotropic. In general the rule of thumb is to measure at least  $10 * d$  behind the turbulence grid. Where  $d$  is the characteristic scale of the grid. Important to note is that the turbulence intensity ( $TI_i$ ) will decay with increasing distance from the grid ( $x$ ) and the integral length scale ( $\Lambda_i$ ) will grow. These quantities are given for static grids in Ref. [21], and for jet injection in Ref. [4], and for oscillating grids in [24].

Additionally it is desirable to have minimal change in intensity and integral length scale in the region where the experiment is performed. It should be noted that the largest gradient in these quantities is near the grid.

#### Passive grids

The functioning of a passive grid is based on two effects. The first is a manipulation effect altering the spectrum of incoming turbulence. The second is the wake-effect which contributes turbulent energy to the flow field behind the grid. The frequency of this turbulent energy is quite high and decreases the scale of the upstream fluctuations. This approach of turbulence generation causes large pressure drops because all energy of the turbulence comes directly from the flow. This approach is discussed in the paper of P.E. Roach [21]. Various grid types are compared here, a

number of types are: mesh grids constructed of fine wires, grids of rods of square or circular cross-section, or perforated plates. Important parameters in the design are the solidity of the grid, defined as:

$$\sigma^* = \frac{\text{open area}}{\text{total area}} \quad (\text{C.1})$$

It is generally considered required to keep the solidity below a value of 0.5 in order to produce homogeneous turbulence. This is mentioned in both the work of J.V. Larssen [15] and the work of P.E. Roach [21]. In addition P.E. Roach notes that the dimensions of the grid rods (or holes) should be significantly smaller ( $<10\%$ ) compared to the dimensions of the channel. No source is provided other than unpublished work by the author. In the design of the grid this will be kept in mind. The results of these type of grids as given in the paper by P.E. Roach show turbulence intensities ranging from 11% close to the grid (at  $x/d = 10$ ) to 1% at distances of  $x/d = 100$ . The integral length scales observed near the grid were of the order of the rod diameter  $d$ . The value of the length scale close to the grid is around  $0.5 \cdot d$  at distances of  $x/d = 100$  this is increased to nearly  $10 \cdot d$ . Close to the grid isotropy of the length scales is poor, further away it starts getting closer to Eq.4.11 from Hinze [14].

Another passive method is making use of shear layer turbulence near the inlet nozzle. This approach was used by M. Roger [22]. However this method is mainly suited for circular airfoil, not for straight ones. Another point of contention is the use of shear layer turbulence, the statistics of which are varying from free stream turbulence. The main advantage is that it is silent and produces very high turbulence intensities.

### Active grids

Two types of active grids are to be considered. The first type is a grid of actuated rods with plates attached to them. This type of grid is shown in Refs. [24], and [15]. The rotation of the plate is actuated by electric motors attached to the ends of the rods. Therefore this method requires a lot of engines to drive the turbulence generation grid and can be quite costly. Interestingly enough the pattern of actuation of the motors, the angle, rotation speed, and rotation pattern all affect the turbulence produced. This method therefore requires significant effort to get to work. The advantage obviously is that it can produce a very wide range of turbulent flow fields and spectra. Another downside for the current research is that the actuation will produce some noise which should be avoided during acoustic measurements. However high turbulence intensities can be obtained (depending on the free stream velocity) and also a wide range is possible, this would improve the acoustic signal to noise ratio. Anisotropy of the grid is interesting, depending on the methods used the anisotropy is very high or normal as was documented by Larssen [15]. Also of note is that the return to isotropy for larger distances from the grid is not always there. The second type of active grid is one in which momentum is added through the use of jets injected in the free stream. This method is used in Refs. ([4], and [13]) and works well there. As can be observed the required blockage is much lower when compared to

the other type of grids. In the work of Auderheide, Bode, Friedrichs, and Kožulović [4] there is no mention of measurements on the isotropy of the flow. However the flow is very homogeneous for large portions of the measurement section. They followed the approach laid out in the other paper by Gad-el-Hak and Corrsin [13]. The levels of isotropy mentioned in this paper show that the axial flow component ( $u'$ ) and the vertical component ( $w'$ ) are of the same order (within 5%). The component in  $y$ -direction (horizontal), and perpendicular to the mean flow differed by as much as 15%. This difference is explained due to the rods used for jet injection being placed only horizontal, parallel to the  $y$ -axis.

## C.2 Initial design and layout

The grid built for the experiments was chosen to be a passive grid. An extension was built which could be connected to the contraction cone in the Twente wind-tunnel. This section has a slot in it so different types of grid could be used without having to completely reconstruct the test section of the wind-tunnel. A picture of this setup functioning is shown on the left in figure C.4.

For the grids themselves a cylindrical cross section was chosen with a diameter of  $d = 10\text{mm}$  for all grids. This diameter was chosen as a constant to keep the integral length scale of the turbulence  $\Lambda$  constant since this is determined by the characteristic size of the grid. The mesh size  $M$  was varied across the three grid design to obtain different values of another important parameter: the solidity  $\sigma^*$ .

The solidity of the grid is important because for the generation of homogeneous and isotropic turbulence it is generally considered good practice to use a solidity value of  $\beta < 0.5$ , see the work of Roach [21], and Larssen [15]. For a square-mesh grid the solidity of the grid can be calculated using the following relation:

$$\sigma^* = \left(1 - \frac{d}{M}\right)^2 \quad (\text{C.2})$$

Where  $d$  is the diameter of the rods or beams used in the grid and  $M$  is the periodic spacing between the rods or beams. This is also shown in figure 3.4. The design parameters of the three grids are shown in table C.1.

Grid no.	Diameter $d$ [mm]	Mesh spacing $M$ [mm]	Solidity $\sigma^*$ [–]
1	10	19.55	0.2386
2	10	25.00	0.3600
3	10	29.60	0.4385

Table C.1: Table detailing the different design parameters of the original grids.

A problem with turbulence grids making use of cylindrical rods is that the vortex shedding behind the cylinders can cause flow induced vibrations. In order to check this the lowest eigenfrequency of the rods was calculated for transversal vibrations of a clamped system. This resulted in the following relation for the first eigenfrequency:

$$f_1 = \frac{22.3729}{2\pi} \sqrt{\frac{EI}{\rho AL^4}} \quad (\text{C.3})$$

This will be shown to be true in the next section of this appendix. From this equation we can learn that this frequency is highest when maximizing the Young's modulus of the material  $E$ , the moment of inertia  $I$ , and minimizing the density  $\rho$  and the cross sectional area  $A$ . It should be noted that increasing the wall thickness of the cylinder lowers the first natural frequency. Since we want to check whether this can go below the highest vortex shedding speed we should use the largest length of the rods in this equation.

In addition to this the highest vortex shedding frequency for the cylinders was also determined. If this turns out to be higher than the lowest eigen frequency there will be problems with oscillations. If not, there will most likely be no problem. The vortex shedding frequency can be determined by means of the Strouhal number which is defined as:

$$St = \frac{f_{vs} d_r}{U_\infty} \quad (\text{C.4})$$

Where  $f_{vs}$  is the vortex shedding frequency,  $d_r$  is the rod diameter, and  $U_\infty$  is the free stream velocity. The Strouhal number itself is determined as a function of the Reynolds number for specific cross sections, in this case cylindrical. We use the values given by Fey, König, and Eckelmann [12]. These show that for a Reynolds number of around  $10^3$  the Strouhal number is at its maximum. This corresponds to the highest vortex shedding frequency. Let us assume that this is a Strouhal value of 0.22. This results in a shedding frequency of:

$$f_{vs} = \frac{0.22 \cdot 50}{0.01} = 1100 \text{ Hz}$$

## C.3 Frequency analysis of the grid

In the hope to get an idea on how the grid will respond under the excitation by the flow an analysis will be provided here to give some predictive capabilities. This will consist of two parts. First the mechanical part will give insight in the frequency response of the rods or beams placed in the grid. Secondly a flow field behavior and vortex shedding frequencies will be examined.

### C.3.1 Mechanical analysis

The analytical spacial solution for a beam in transverse vibration is given as:

$$\frac{\partial^4 V(x)}{\partial x^4} - \beta^4 V(x) = 0 \quad (\text{C.5})$$

Where:

$$\beta^4 = \frac{\rho A \omega^2}{EI} \quad (\text{C.6})$$

In this equation  $\rho$  is the density of the material,  $A$  is the cross sectional area,  $E$  is the Young's modulus of the material, and  $I$  is the moment of inertia. Writing this in term of the period:

$$\omega = \beta^2 \sqrt{\frac{EI}{\rho A}} \quad (\text{C.7})$$

The general solution to this differential equation is:

$$V(x) = B_1 \cos(\beta x) + B_2 \sin(\beta x) + B_3 \cosh(\beta x) + B_4 \sinh(\beta x) \quad (\text{C.8})$$

Applying the following boundary conditions:

$$\begin{aligned} \text{at } x = 0: \quad & V(0) = 0 \\ & V'(0) = 0 \\ \text{at } x = L: \quad & V(L) = 0 \\ & V'(L) = 0 \end{aligned}$$

From this it follows that:

$$\begin{aligned} B_1 + B_3 &= 0 \\ B_2 + B_4 &= 0 \\ B_1 \cos(\beta L) + B_2 \sin(\beta L) + B_3 \cosh(\beta L) + B_4 \sinh(\beta L) &= 0 \\ -B_1 \sin(\beta L) + B_2 \cos(\beta L) + B_3 \sinh(\beta L) + B_4 \cosh(\beta L) &= 0 \end{aligned}$$

Writing in matrix vector form:

$$\begin{bmatrix} 1 & 0 & 1 & 0 \\ 0 & 1 & 0 & 1 \\ \cos(\beta L) & \sin(\beta L) & \cosh(\beta L) & \sinh(\beta L) \\ -\sin(\beta L) & \cos(\beta L) & \sinh(\beta L) & \cosh(\beta L) \end{bmatrix} \cdot \begin{Bmatrix} B_1 \\ B_2 \\ B_3 \\ B_4 \end{Bmatrix} = \begin{Bmatrix} 0 \\ 0 \\ 0 \\ 0 \end{Bmatrix} \quad (\text{C.9})$$

Making use of the fact that  $B_3 = -B_1$  and  $B_4 = -B_2$  we can simplify to a  $2 \times 2$  matrix:

$$\begin{bmatrix} \cos(\beta L) - \cosh(\beta L) & \sin(\beta L) - \sinh(\beta L) \\ -\sin(\beta L) - \sinh(\beta L) & \cos(\beta L) - \cosh(\beta L) \end{bmatrix} \cdot \begin{Bmatrix} B_1 \\ B_2 \end{Bmatrix} = \begin{Bmatrix} 0 \\ 0 \end{Bmatrix} \quad (\text{C.10})$$

Taking the determinant of this matrix and equating it to zero we obtain the characteristic equation:

$$\begin{aligned} \cos^2(\beta L) + \cosh^2(\beta L) - 2\cos(\beta L)\cosh(\beta L) - (-\sin^2(\beta L) + \sinh(\beta L)) &= 0 \\ \Rightarrow (\cos^2(\beta L) + \sin^2(\beta L)) + (\cosh^2(\beta L) - \sinh^2(\beta L)) - 2\cos(\beta L)\cosh(\beta L) &= 0 \\ \Rightarrow 2\cos(\beta L)\cosh(\beta L) - 2 &= 0 \\ \Rightarrow \cos(\beta L)\cosh(\beta L) - 1 &= 0 \end{aligned} \quad (\text{C.11})$$

From this it follows that:

$$\begin{aligned}\beta L &= 0 \text{ (trivial)} \\ \beta L &= \pm 4.7300\dots \\ \beta L &= \pm 7.8532\dots \\ \beta L &= \pm 10.9956\dots \\ &\text{etc.}\end{aligned}$$

We can now substitute these expressions for  $\beta$  into equation C.7 to obtain the natural frequencies. The following relation is thus obtained:

$$\begin{aligned}\omega_i &= c_i \sqrt{\frac{EI}{\rho AL^4}} \quad [\text{rad/s}] \\ f_i &= \frac{c_i}{2\pi} \sqrt{\frac{EI}{\rho AL^4}} \quad [1/s]\end{aligned} \tag{C.12}$$

Where  $c_i$  is a constant for determining the  $i$ -th eigenfrequency:

$$\begin{aligned}c_1 &= 22.3729 \\ c_2 &= 61.6728 \\ c_3 &= 120.9032\end{aligned}$$

### C.3.2 Vortex shedding

Next we want to determine the excitation frequency at which the rod is actuated by the free stream. This corresponds to the frequency at which vortices are formed and advection away from the cylinder. This process is governed by the dimensionless Strouhal number  $St$  which is defined as:

$$St = \frac{f_{vs} d}{U_\infty} \tag{C.13}$$

Where  $f_{vs}$  is the vortex shedding frequency in Hertz,  $d_r$  is the rod diameter in meters, and  $U_\infty$  is the free stream velocity.

It is further possible to find the relations between the Strouhal number and the Reynolds number for specific (simple) structures like cylinders. For this analysis a paper by Fey, König, and Eckelmann [12] was used. This gives up approximate data to estimate the values of the Strouhal number. This figure was put into Matlab and the data was interpolated using the given relations. In this way the vortex shedding frequency can be determined as a function of the diameter and the free stream velocity since the Reynolds number is also a function of these two. It is also important to note that the variation in Strouhal number in the higher Reynolds range is very minute.

### C.3.3 Results

Ideally we would like the vortex shedding frequency to be lower than the first eigenfrequency, since this would mean that the system will not experience any significantly large vibrations. If this is not possible however it will not necessarily be a problem since as long as the beam is not actuated in an eigenfrequency it will not vibrate a lot.

In figure C.2 the first, second, and third natural eigenfrequencies are plotted as a function of the outer diameter of the rods. The rod thickness has been set to 1 *mm*. It should be noted that the thinner the rods are the higher the natural frequency. This implies that thin rods are desirable. In the figure is also shown the vortex shedding frequency as a function of the diameter. Different lines are drawn for different flow velocities.

From the diagram it is clear that for the long (0.45 *m*) rods the thickness must be large for the shedding frequency to stay under the first natural eigenfrequency.

## C.4 Testing of grid acoustic properties

In order to test the acoustic properties of the grids a quick setup was constructed to measure the acoustic signal using a single movable microphone. The background noise levels of the grids are shown in Fig. C.5 along with the baseline noise levels in the wind tunnel. To test the signal-to-noise ratio for these configuration a meal plate was inserted in the flow and measurements were performed. The differences in acoustic signal was considered to small to be feasible for the acoustic measurements. Initially it was attempted to improve the acoustic properties of the grids. This was done by building an extension to the inlet nozzle, implementing the serrations to the outlet, and breaking the symmetry in the grids by adding helical wires to the rods. The effects of extensions and serrations is shown in Fig. C.5. No significant benefits to the nozzle and serrations were found for the baseline noise levels of the grids in the wind tunnel. The reason the extension was still used later on was to prevent the flow from diverging as much when leaving the outlet.

The effects for the helical wire were tested using several different materials, see Fig. C.6, and for different spacings, Fig. C.7. An optimum was found for a grid spacings of 11  $S_{wing}/d_{rod}$  and the ideal material was found to be thick rubber tubing for pressure tabs.

These helical wires were applied for one of the three grids. Each rod was wrapped in this wire. The acoustic results of the this grid version compared to the baseline is shown in Fig. C.8. In this figure the results are also shown when a flat plate airfoil is present. These results indicated no significant improvement in the acoustic signal-to-noise ratio.

## C.5 Optimizing grid design for acoustic properties

The acoustic properties of the developed first generation grids was found to be unsuitable for noise measurements on flat plate airfoil. Therefore all aluminum rod were removed from the grids and acoustic testing was done for a different grid solidities

and rod types. Many wooden (MDF) rods were constructed that could be snugly fit into the aluminum frame. This way acoustic test could be performed and the rods were still interchangeable. The results for the three grid used in this project are shown in Figs. C.9, C.10, and C.11. The signal-to-noise ratios have much improved in comparison to the the grids of lower solidity. For the wooden grid lower solidities were also tries, see Fig. C.12, here however it is already visible that the acoustic signal resolution is getting worse compared to the other configurations. this is the reason we obtained the three grids that were used during this thesis.

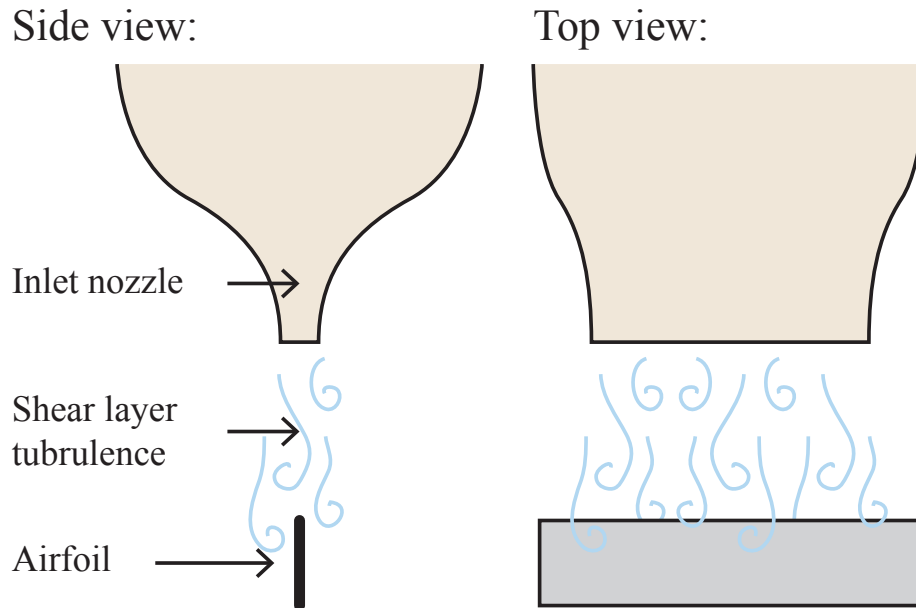


Figure C.1: Proposed contraction nozzle for generation of shear layer turbulence for flat wing designs.

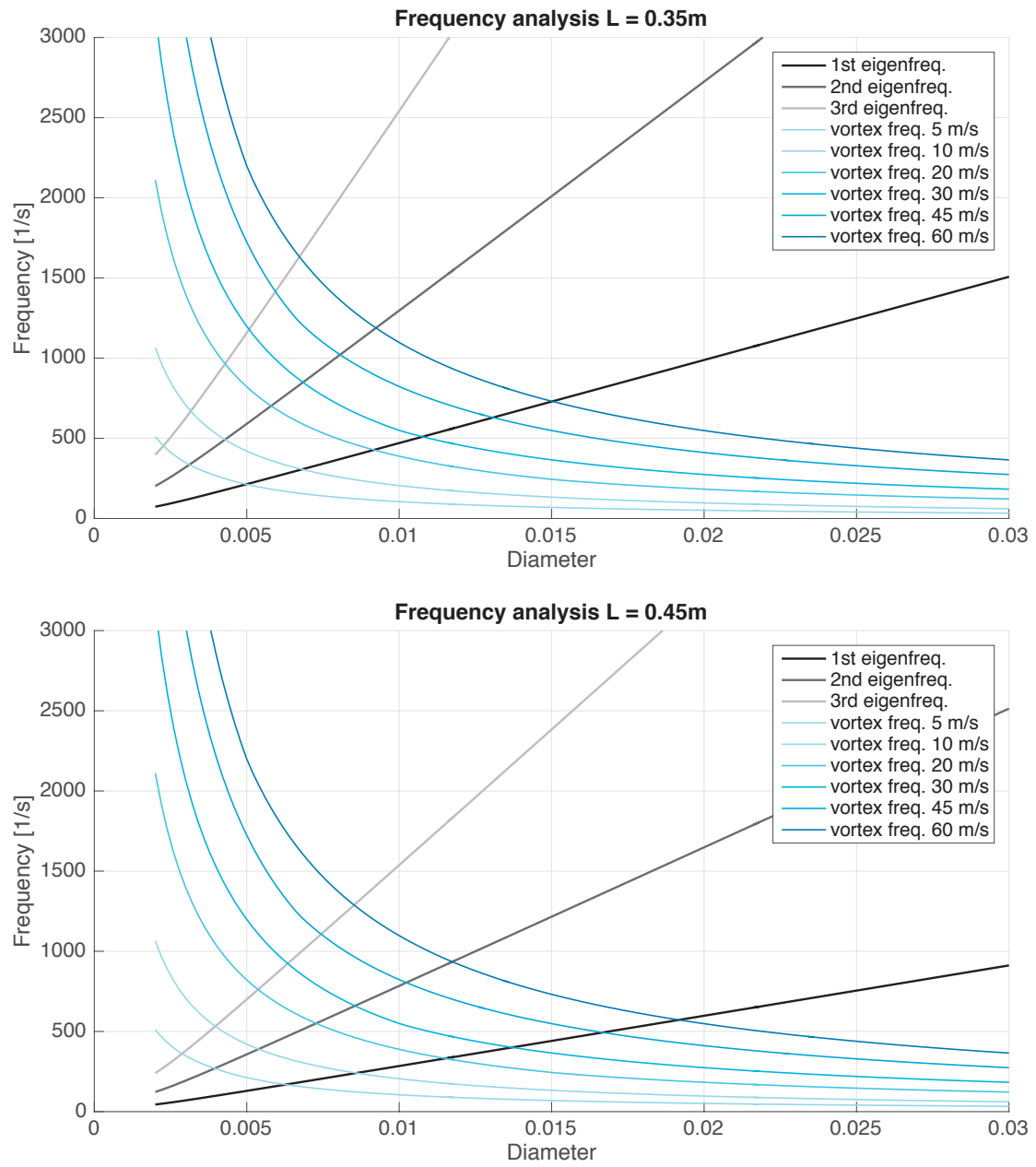
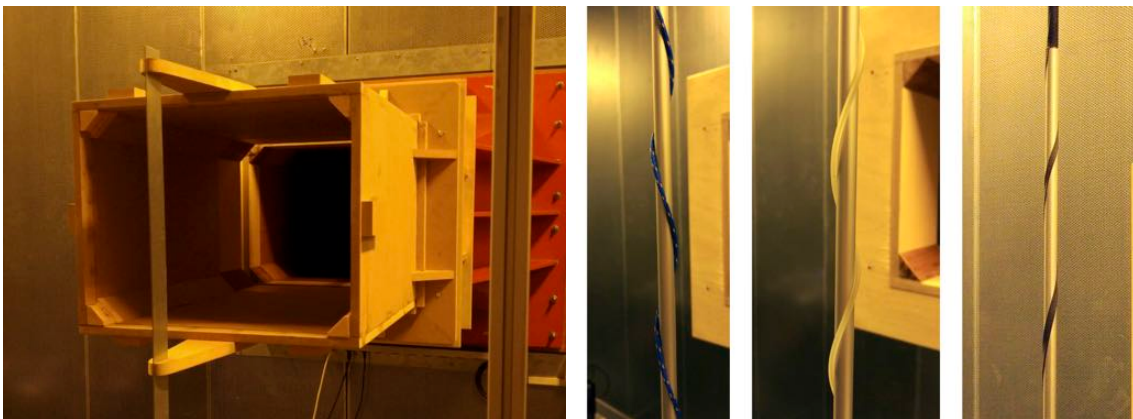


Figure C.2: Frequency of the grid: Eigenfrequencies (1,2, and 3) as a function of diameter and the vortex shedding frequencies as a function of diameter and free stream velocity.



Figure C.3: Left: One of the turbulence grid being inserted into the slot in the wind tunnel section developed for interchangeable grids. Middle: Extension constructed to magnetically mount different serration profiles to the inlet nozzle. Right: The extension construction to extend the length of the inlet nozzle in order to direct grid noise down stream instead towards the microphones.



(a) Temporary setup to test the leading edge noise produced by a flat plate airfoil. (b) Three variations of wires used to wrap the rods with.

Figure C.4: Two of the temporary experimental setups used in order to study the acoustic properties of the grid.

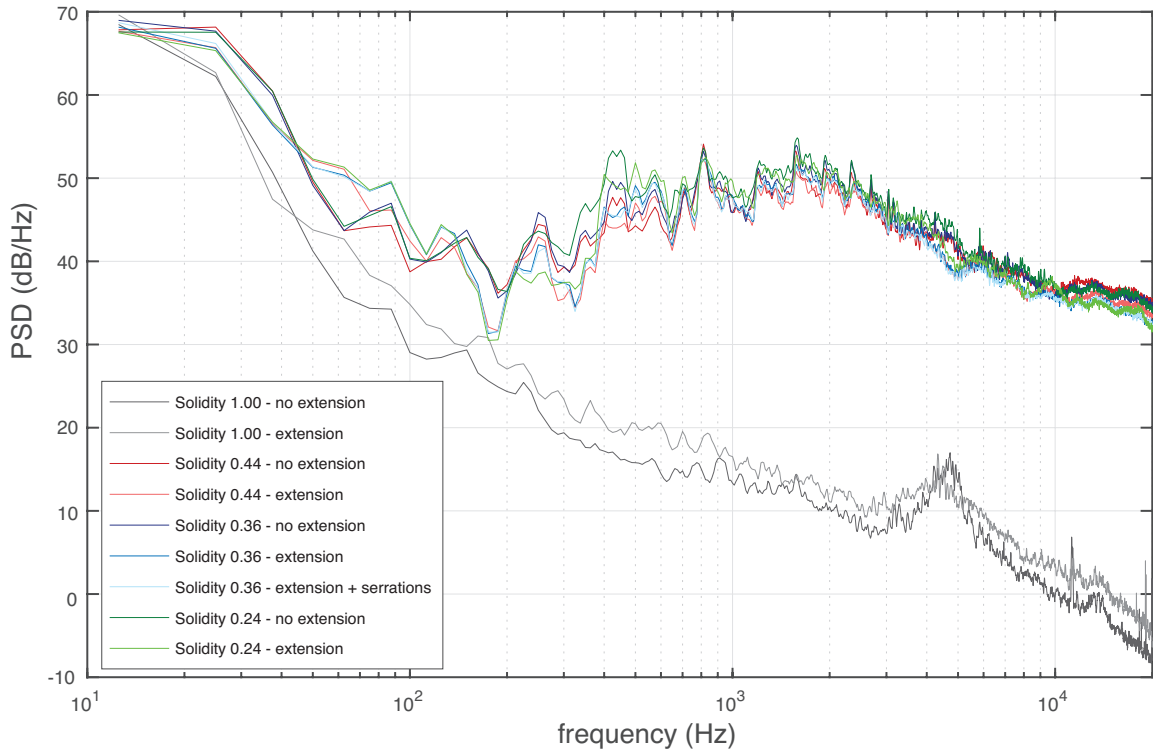


Figure C.5: Noise generated by the first generation grids.

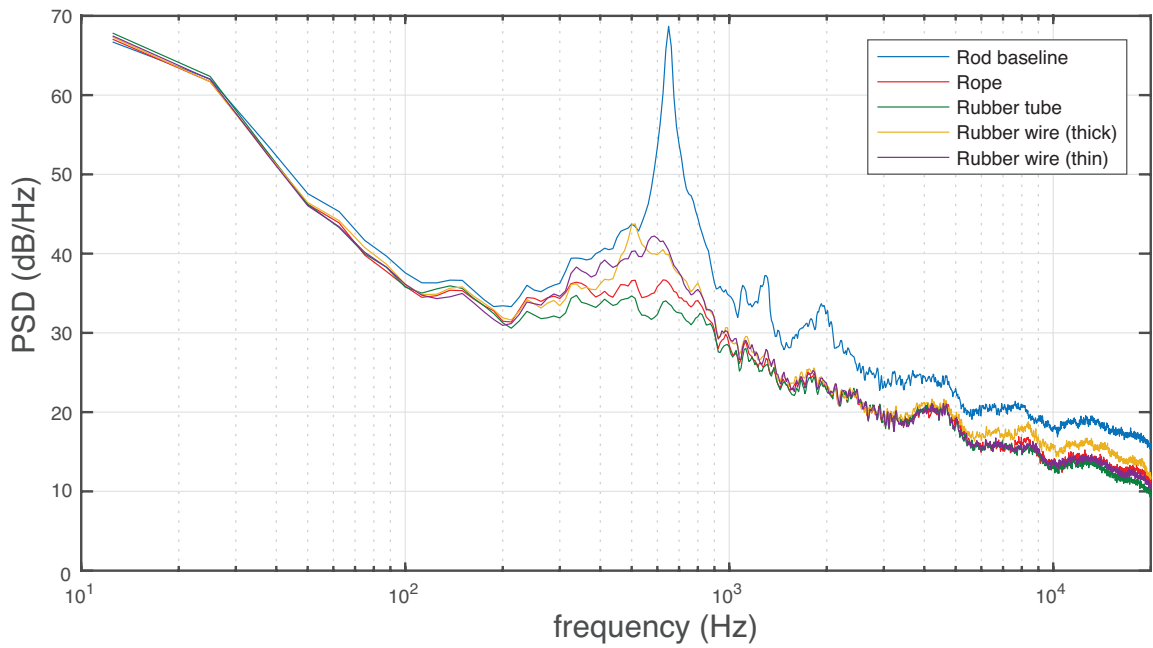


Figure C.6: Noise produced by rod for various types of helical wires.

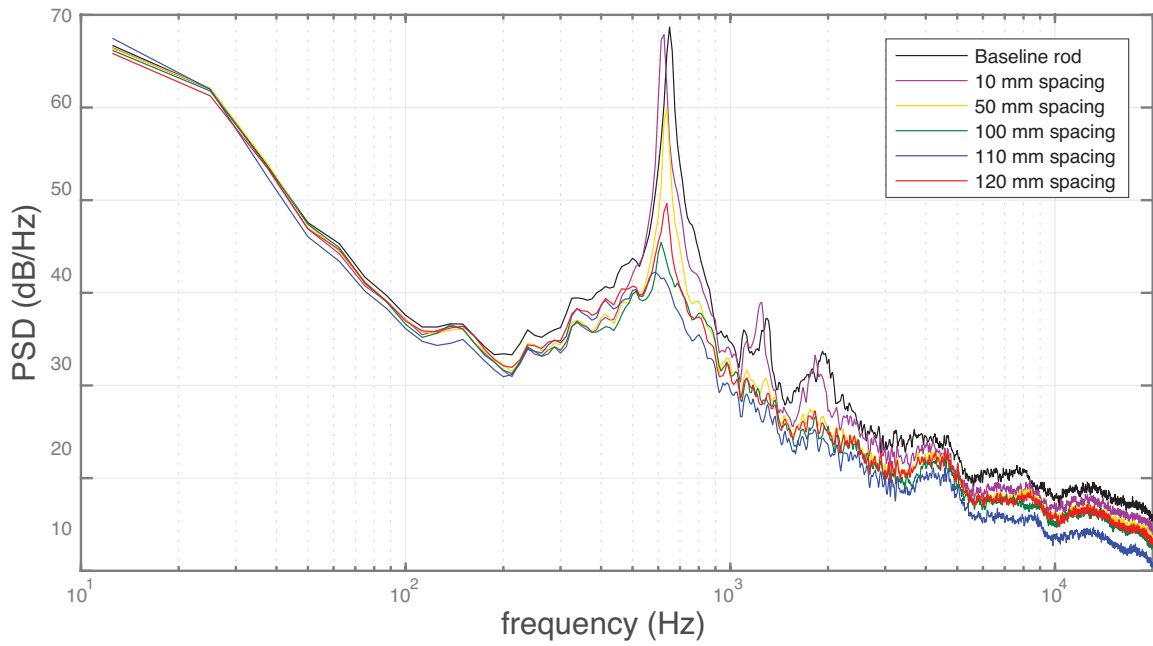


Figure C.7: Noise produced by rod for various wire spacings.

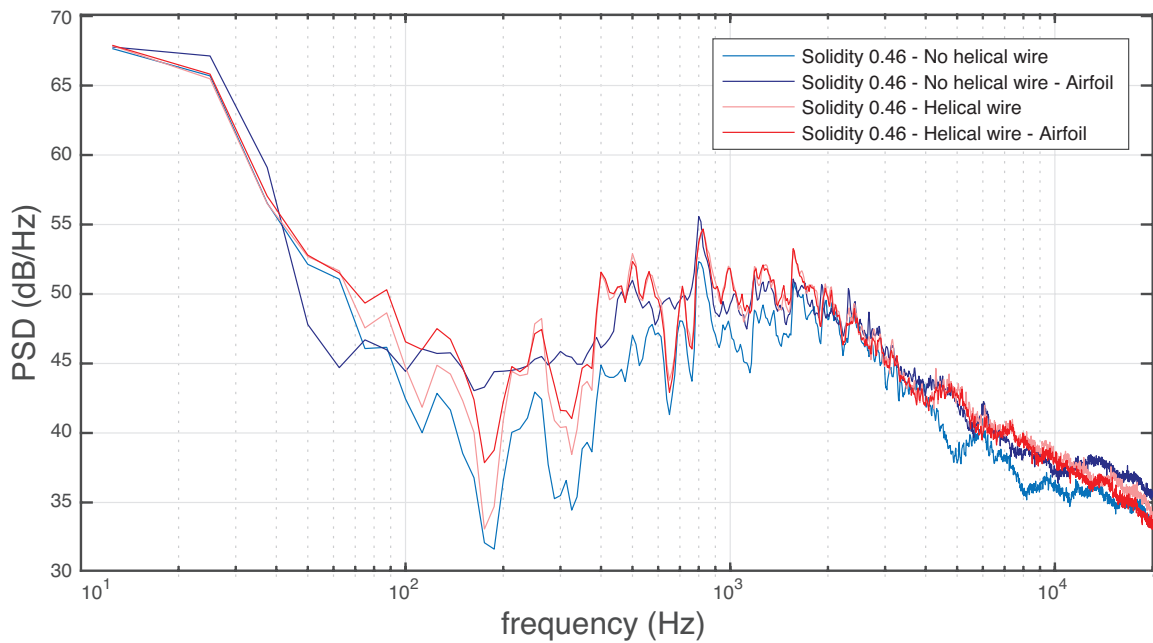


Figure C.8: Influence of the wires on the acoustic performance of the grid and the resulting signal to noise ratio.

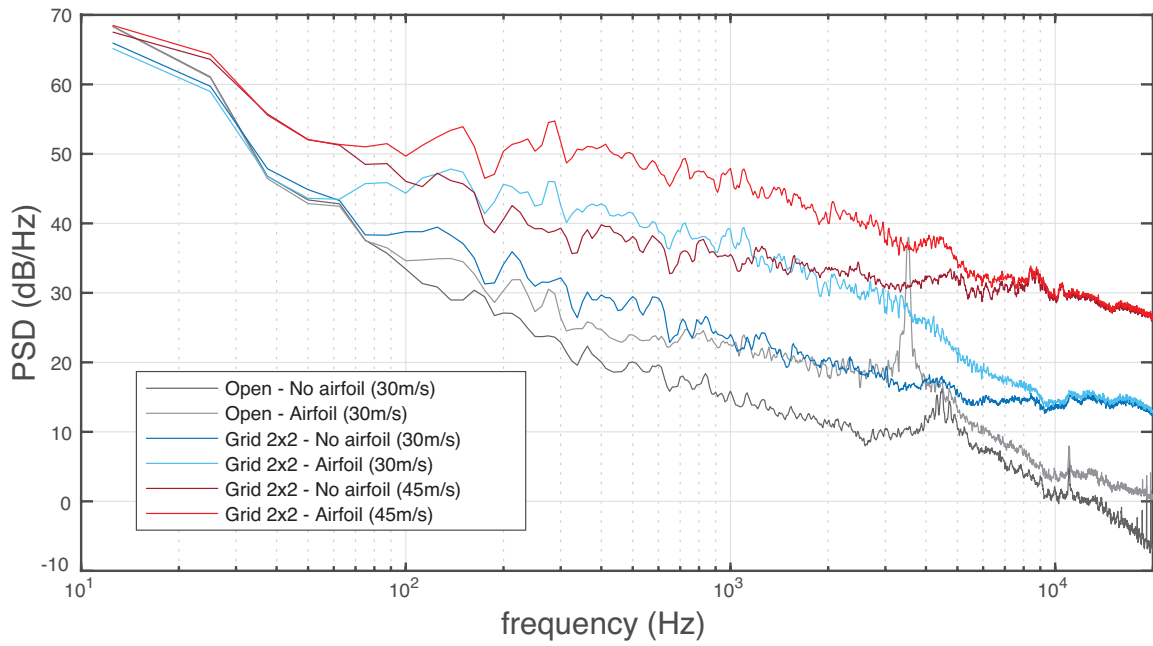


Figure C.9: Signal to noise ratio of the wooden grid of 2x2 rods.

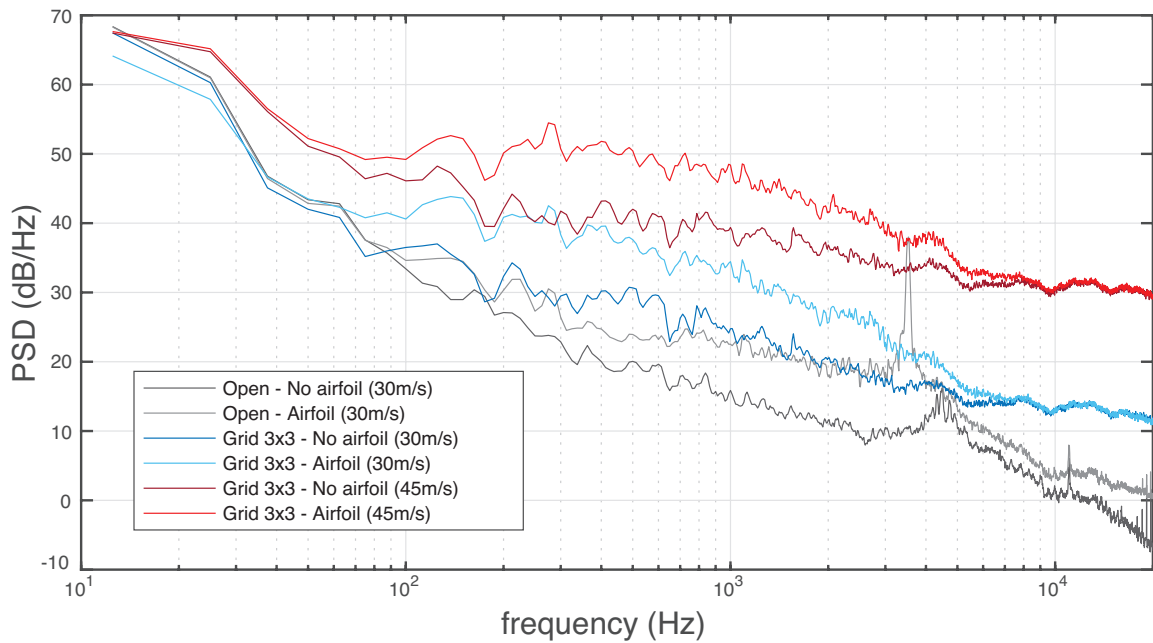


Figure C.10: Signal to noise ratio of the wooden grid of 3x3 rods.

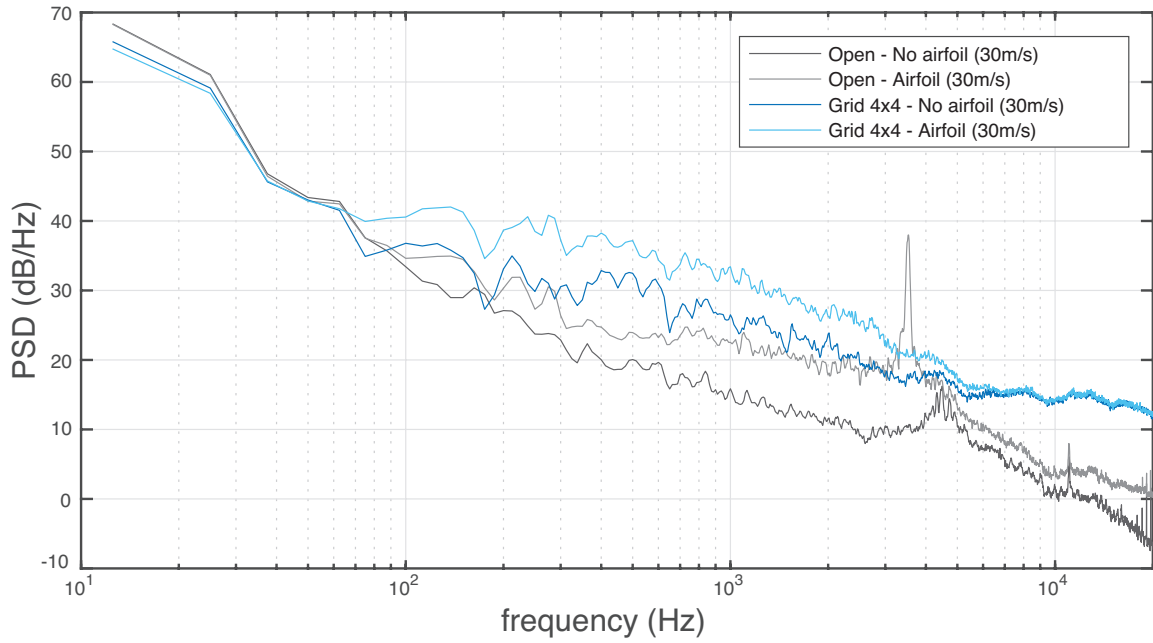


Figure C.11: Signal to noise ratio of the wooden grid of 4x4 rods.

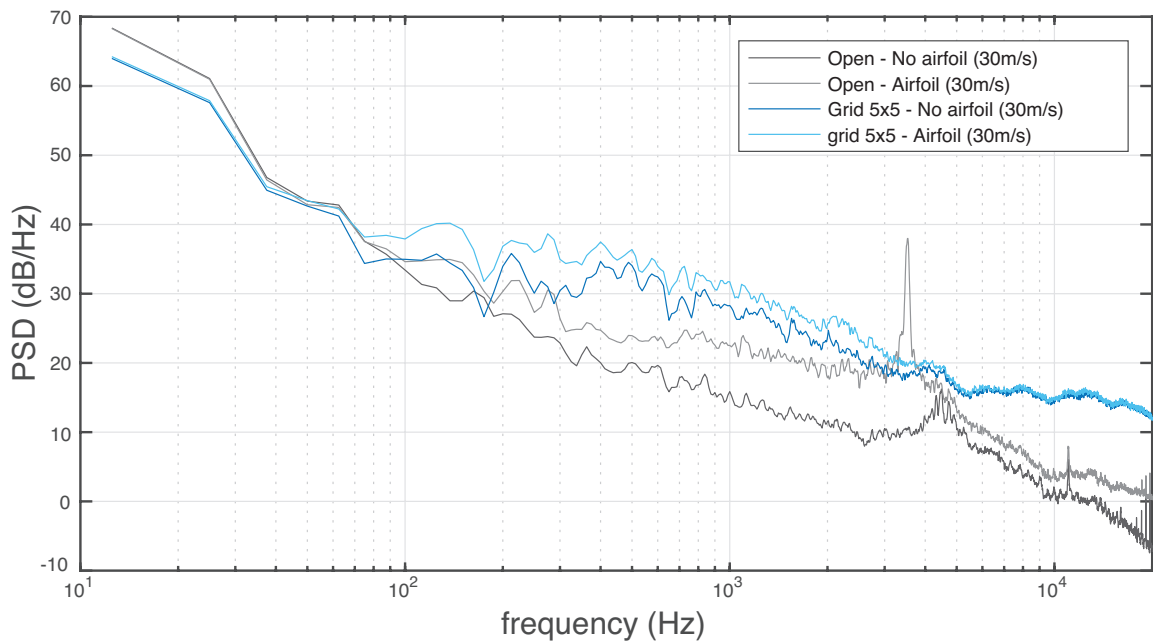


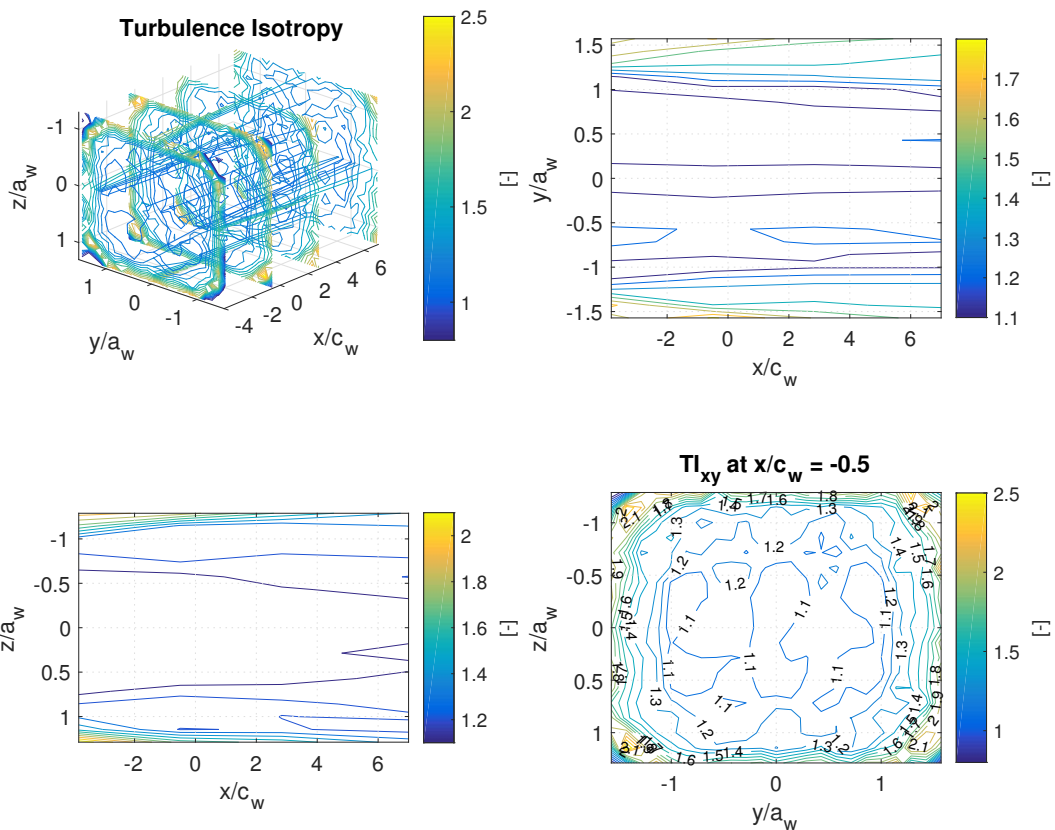
Figure C.12: Signal to noise ratio of the wooden grid of 5x5 rods.

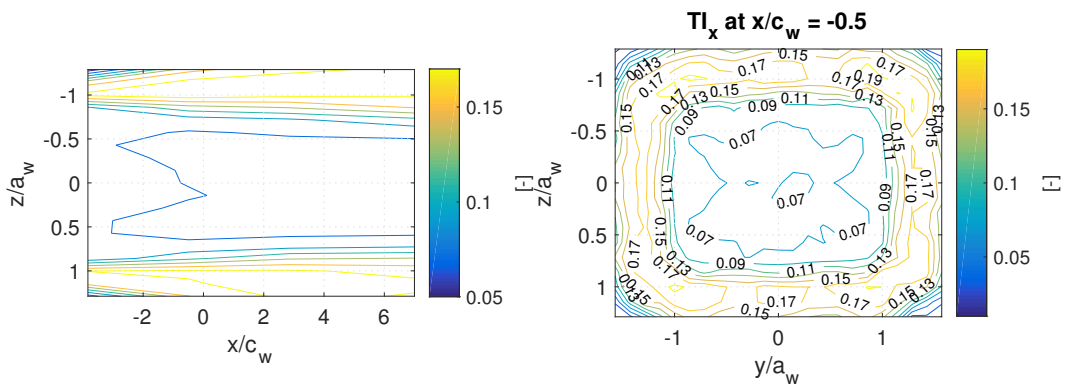
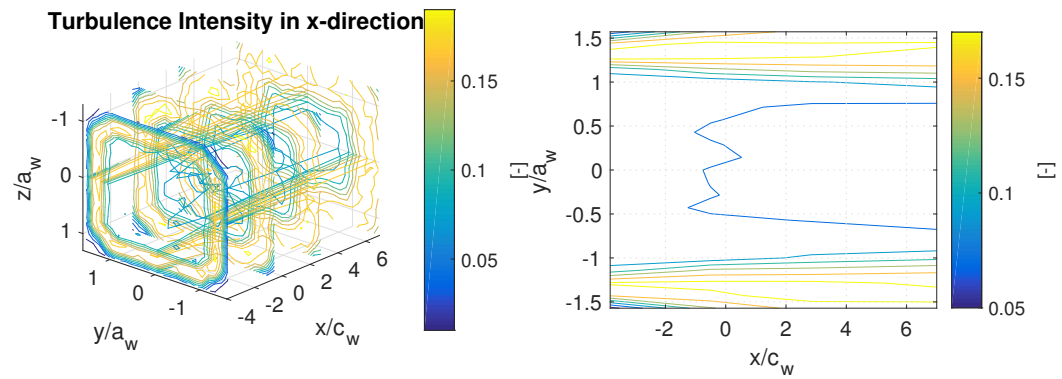
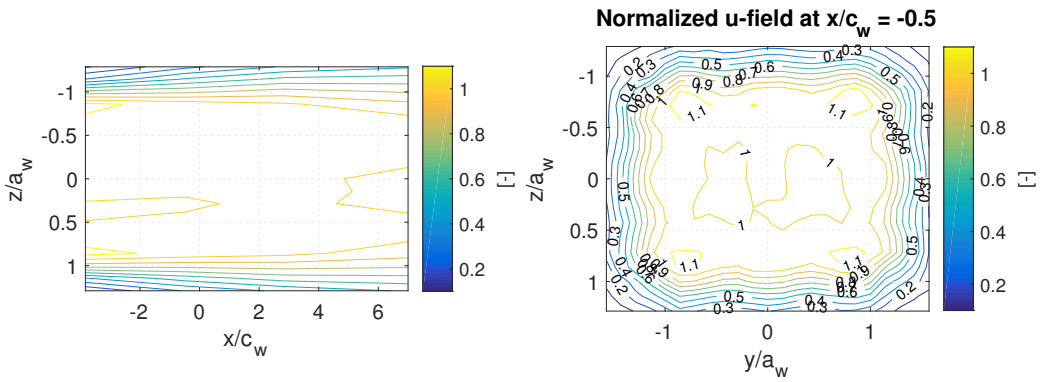
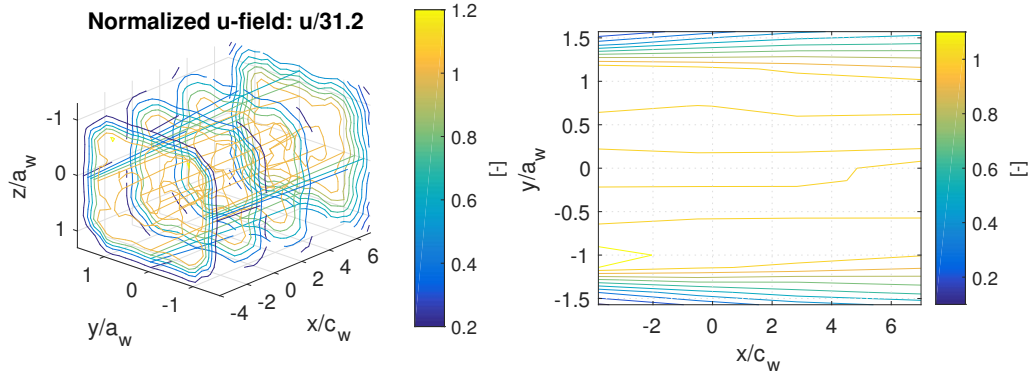
# Appendix D

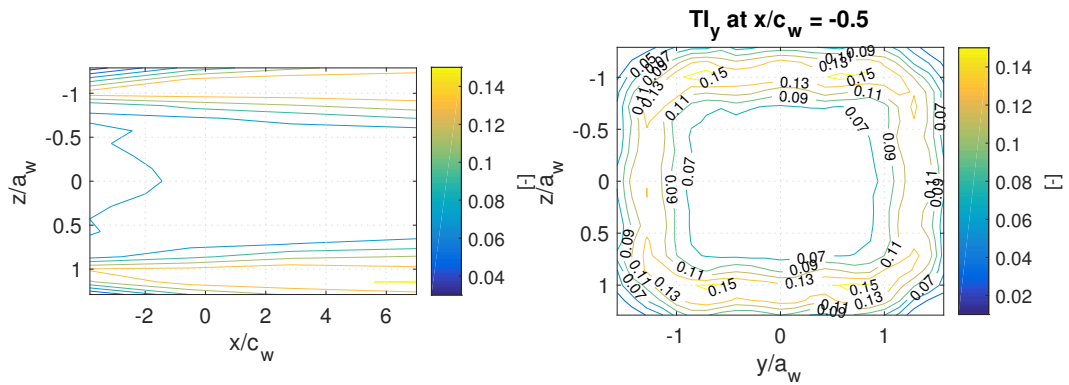
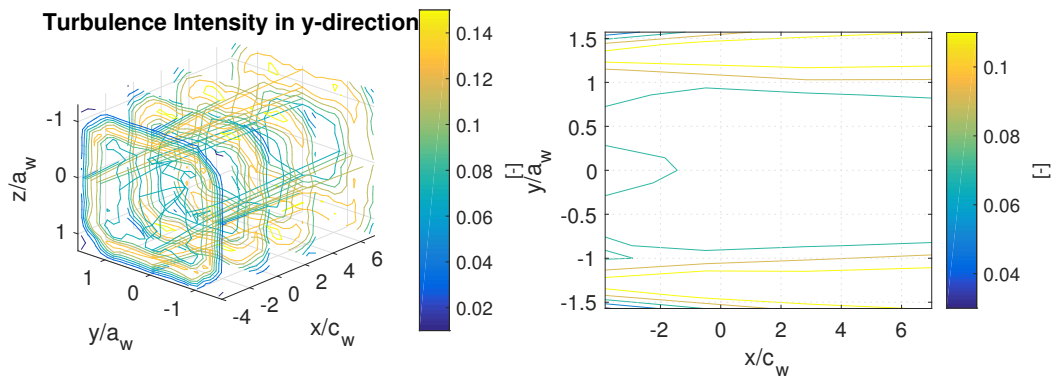
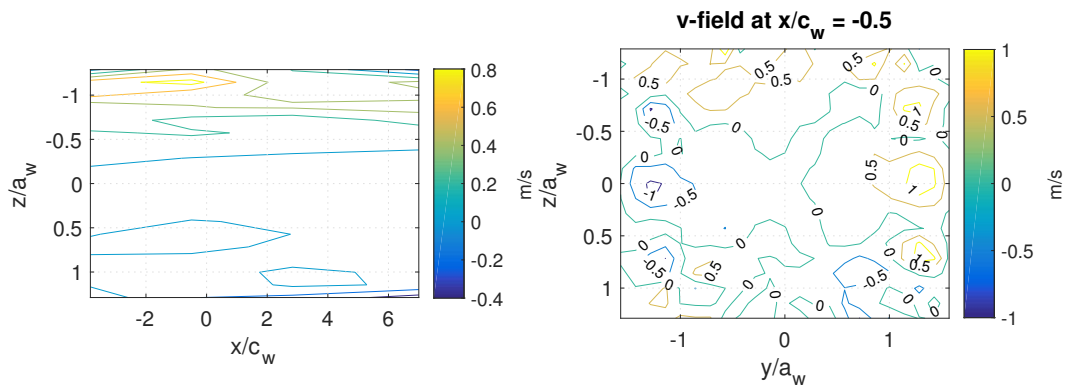
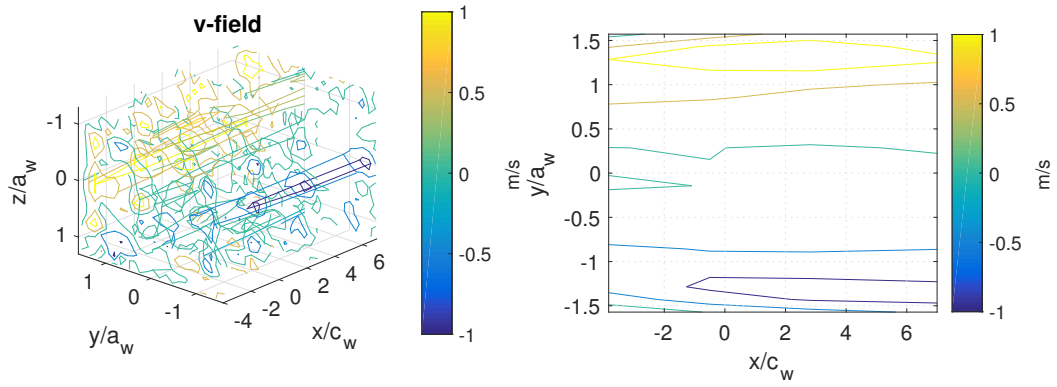
## Measurement results CTA: turbulence measurements

### D.1 Velocity and Turbulence fields

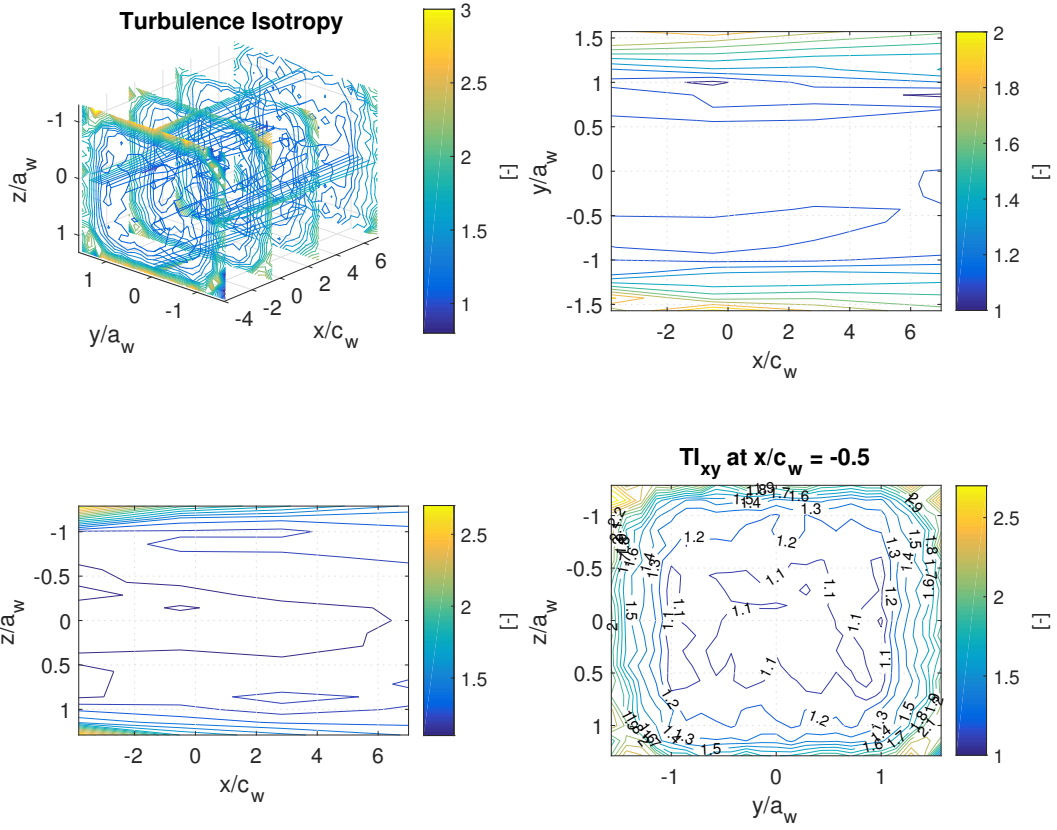
Grid 1 (2x2) - 30m/s

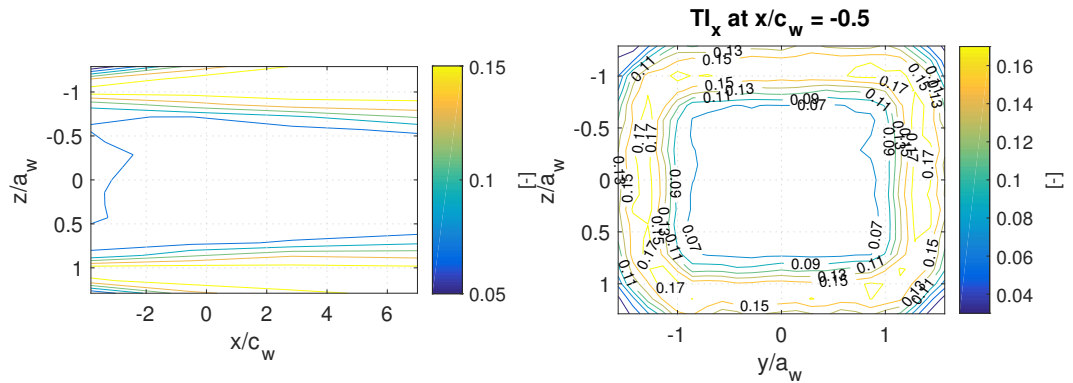
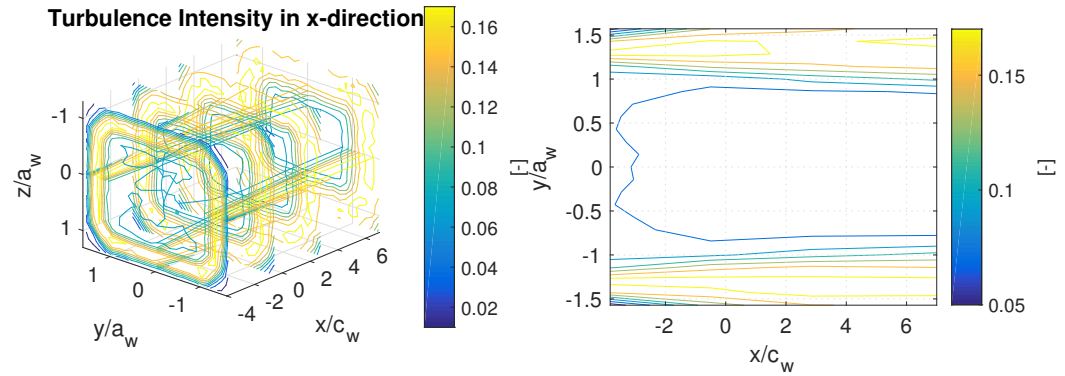
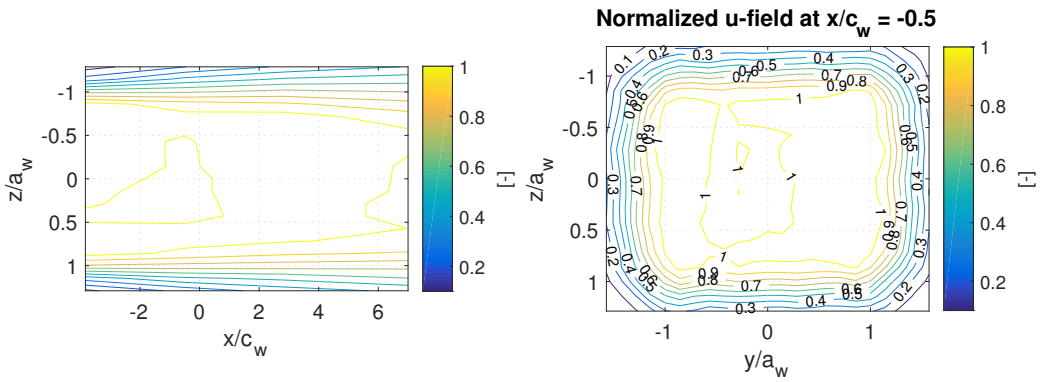
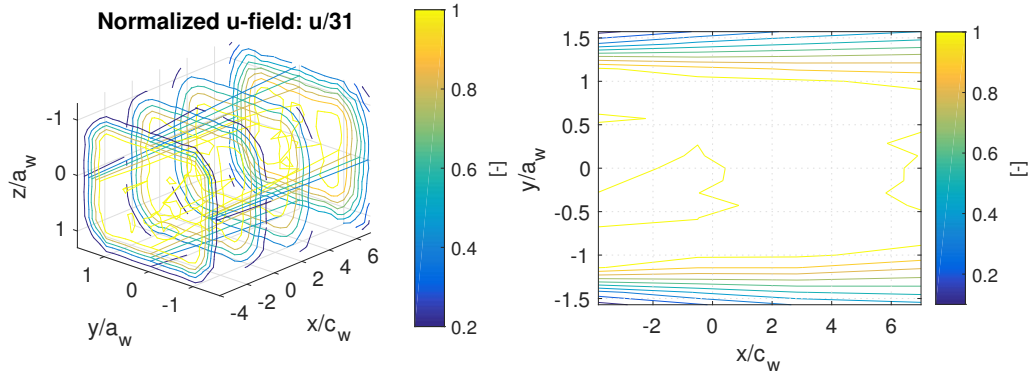


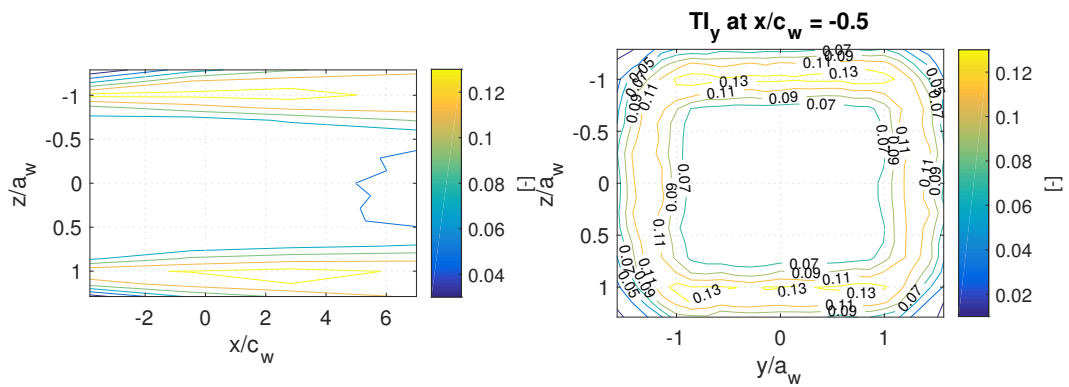
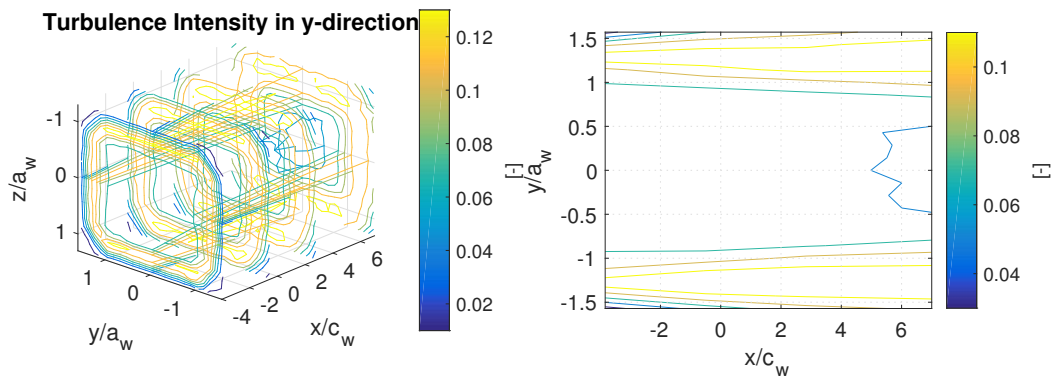
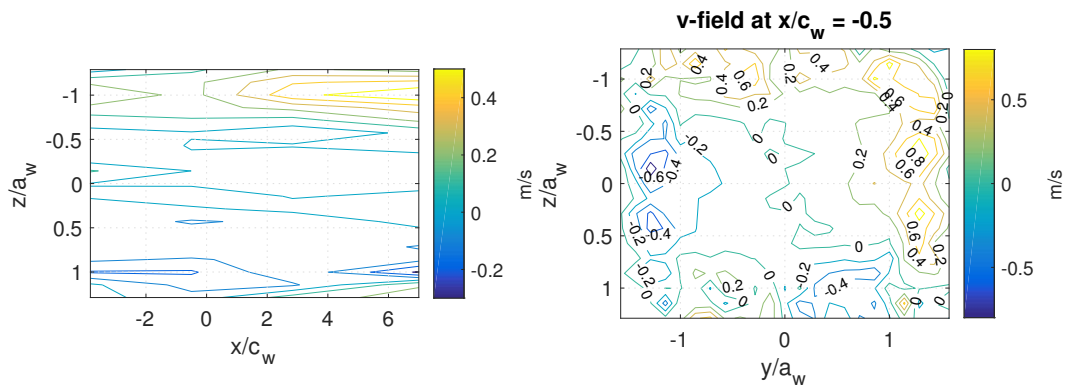
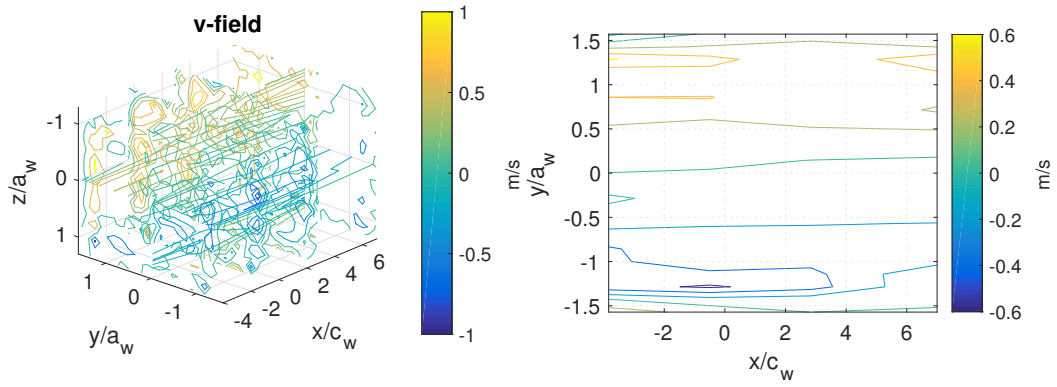




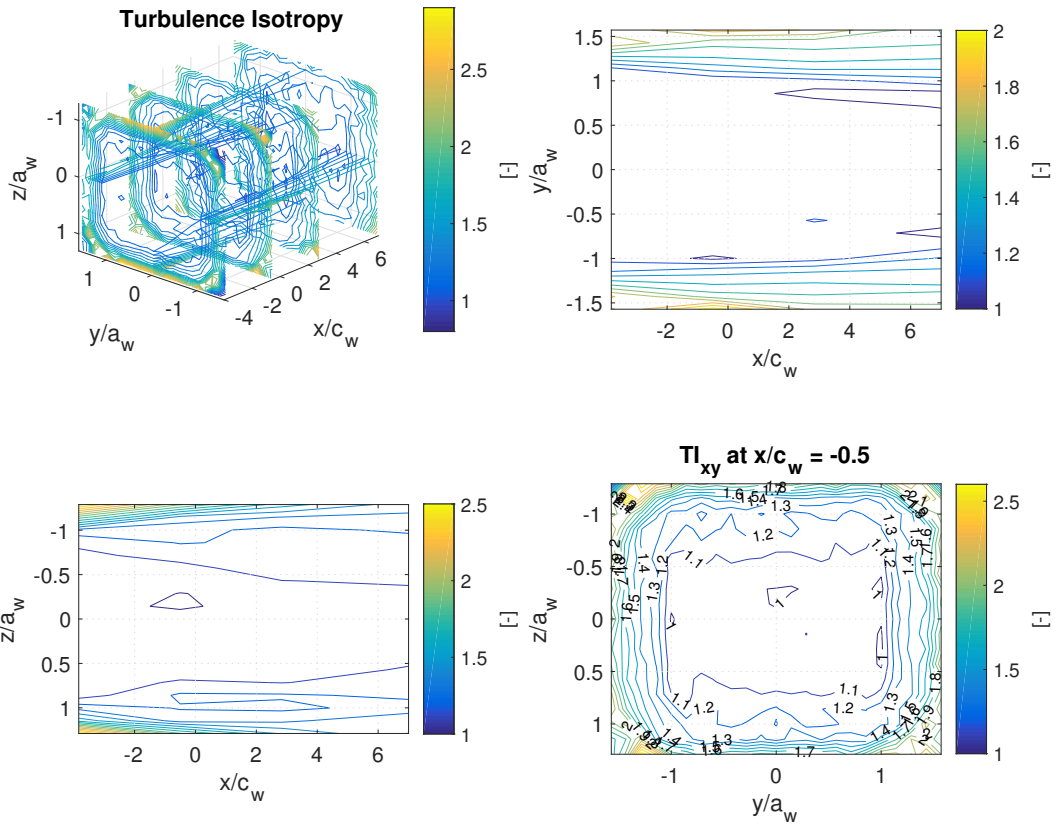
# Grid 2 (3x3) - 30m/s

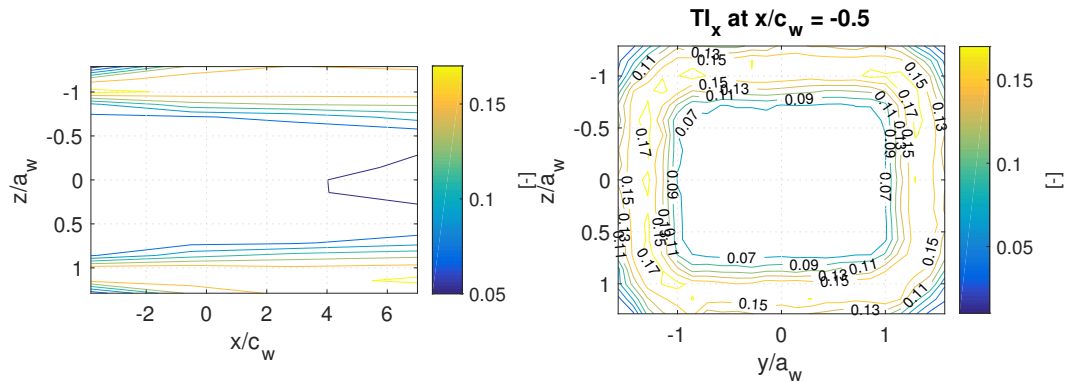
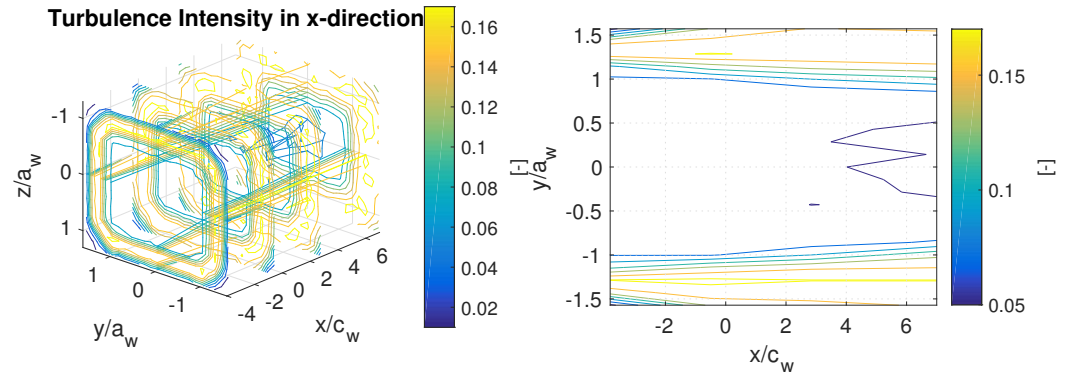
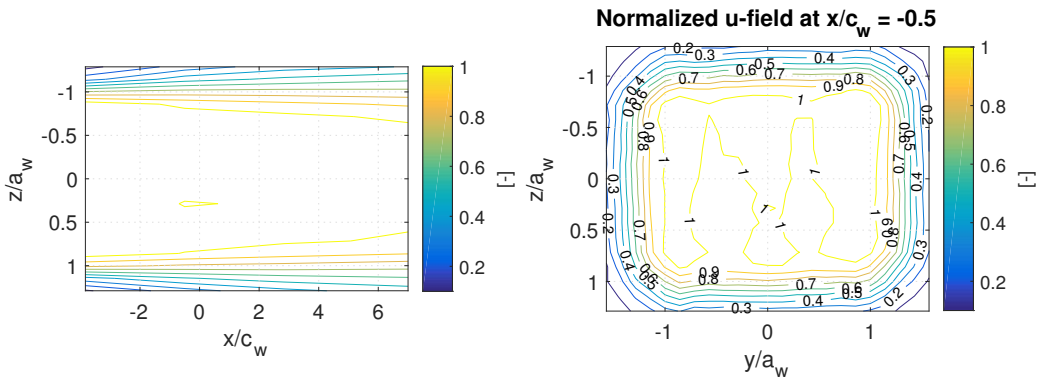
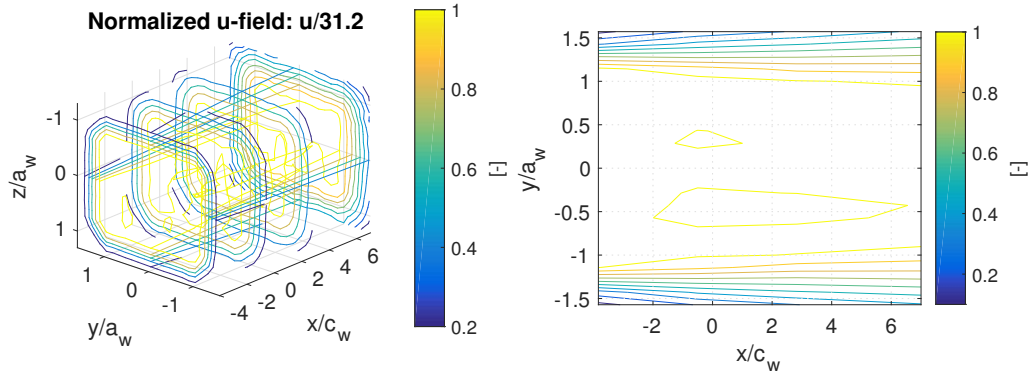


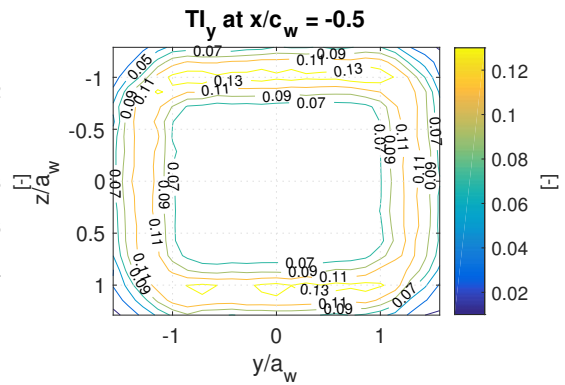
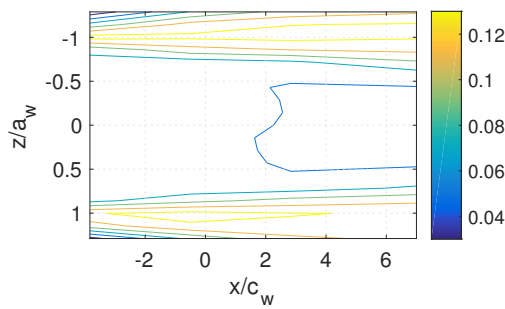
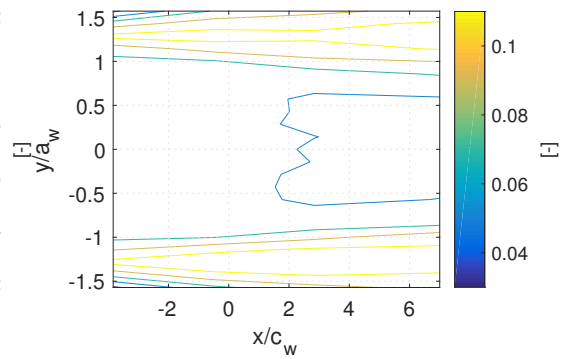
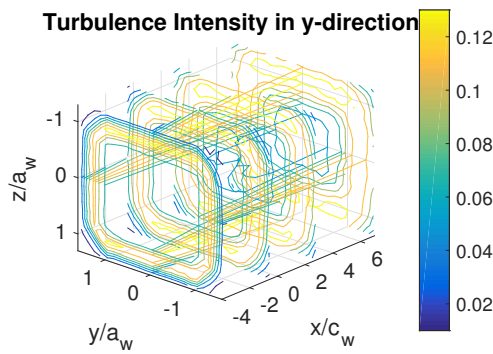
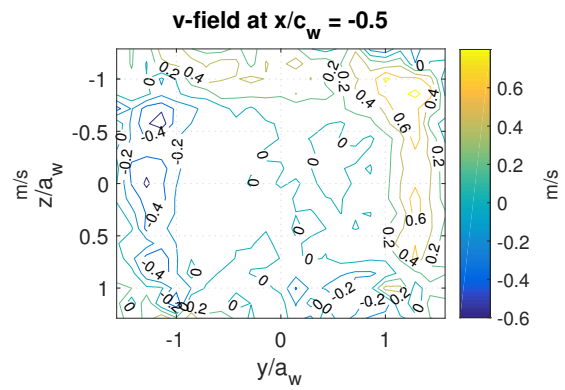
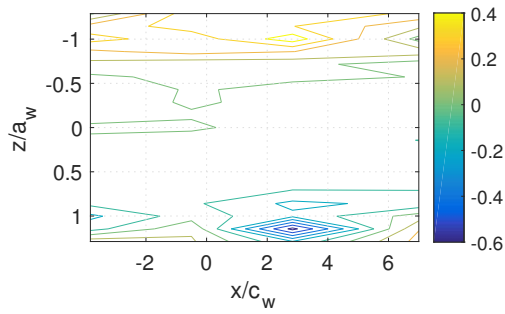
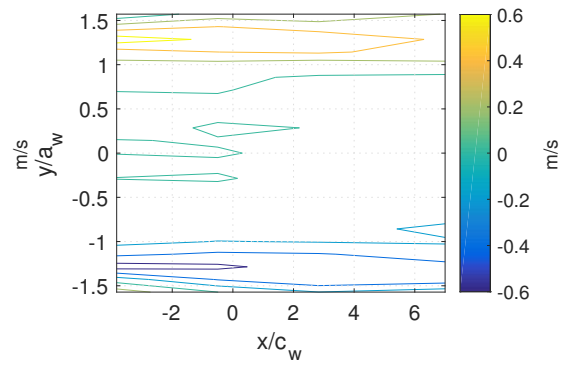
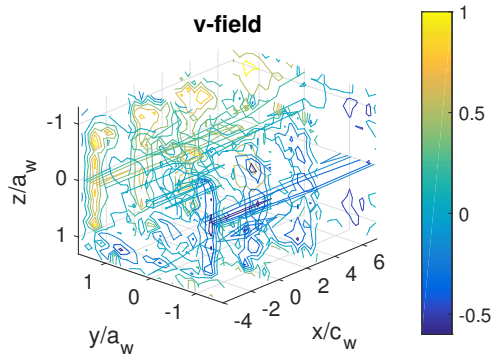




### Grid 3 (4x4) - 30m/s







## D.2 Leading edge turbulence characterization

### D.2.1 Velocity and turbulence intensities

Results Grid 0 (0x0):  $x/c_w = -0.5$

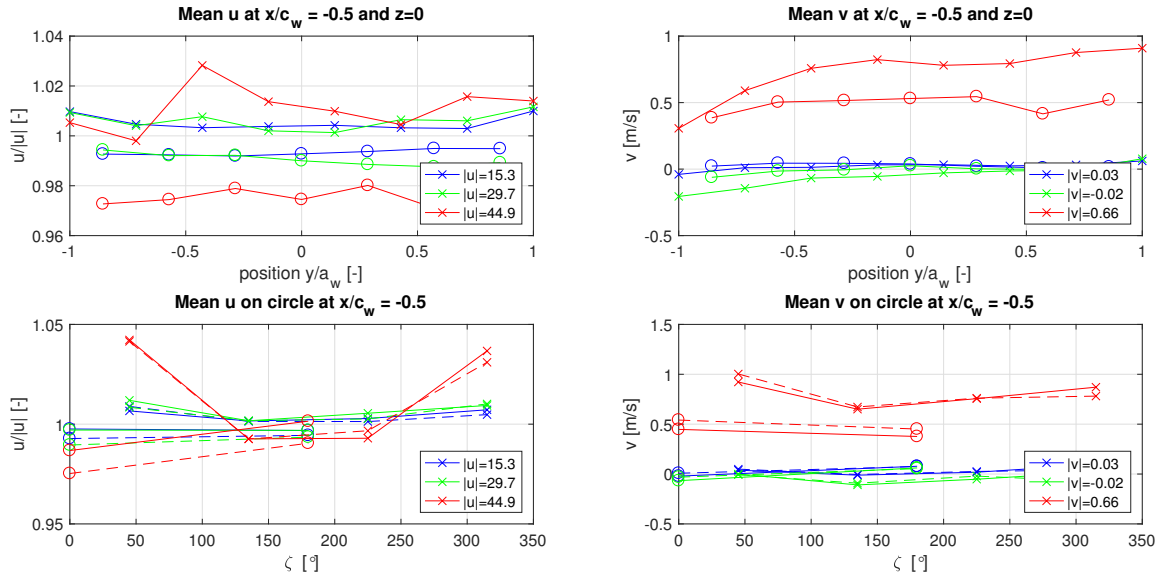


Figure D.1: Normalized flow velocity for the  $x$ - and  $y$ -directions in the plane located at the leading edge of the airfoils.

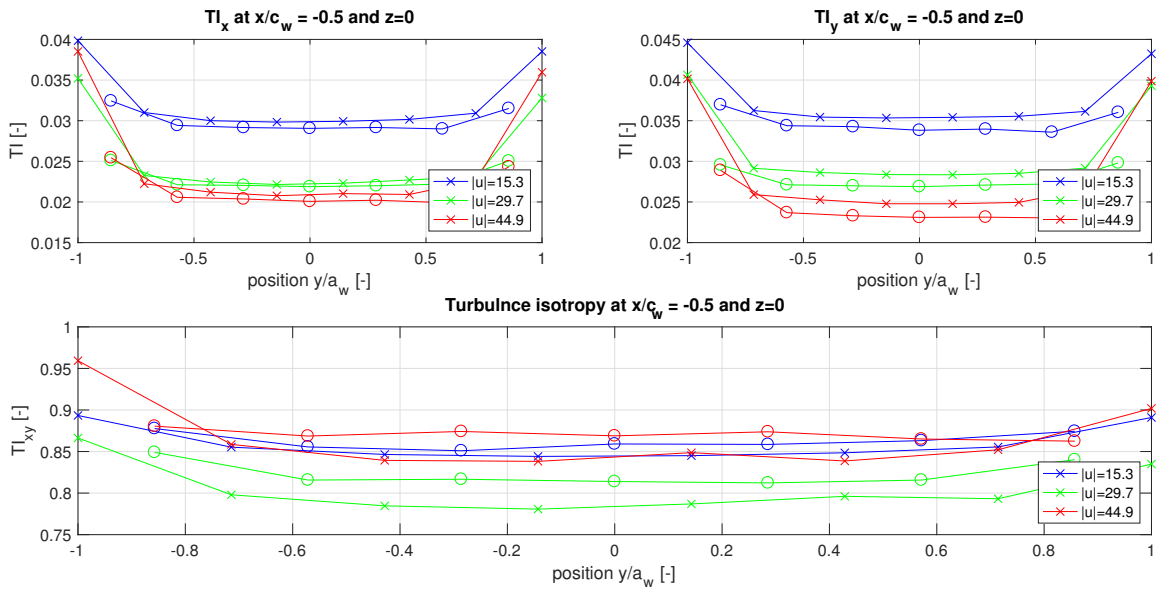


Figure D.2: Top: Turbulence intensities in  $x$ - and  $y$ -directions. Bottom: Turbulence isotropy parameter. Results for the plane at the airfoils leading edge.

### Results Grid 0 (0x0): $x/c_w = 2.833$

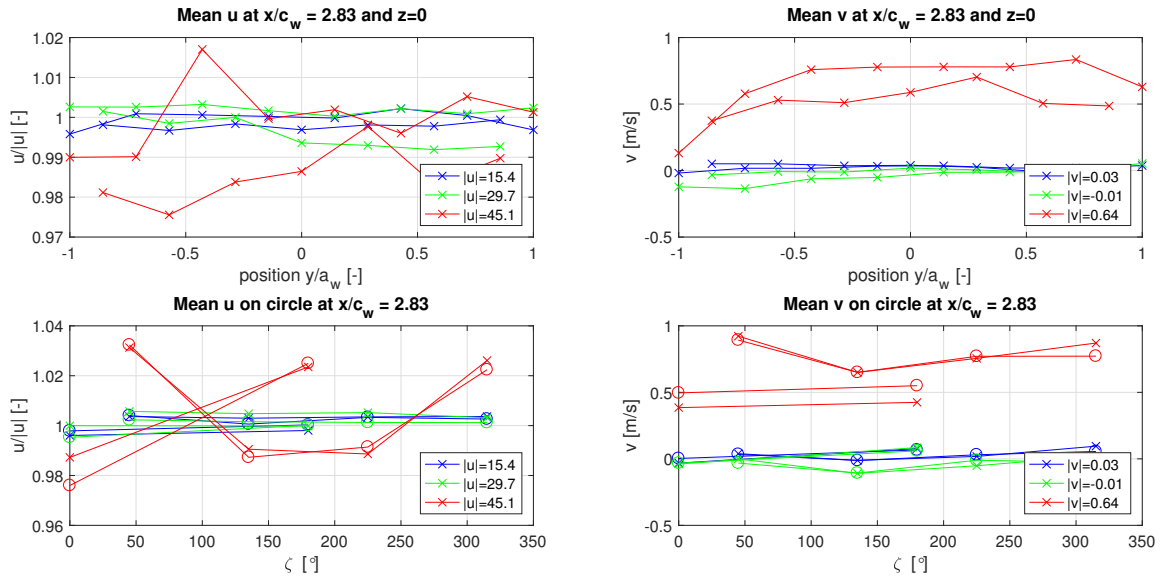


Figure D.3: Normalized flow velocity for the  $x$ - and  $y$ -directions in the plane located behind the airfoil.

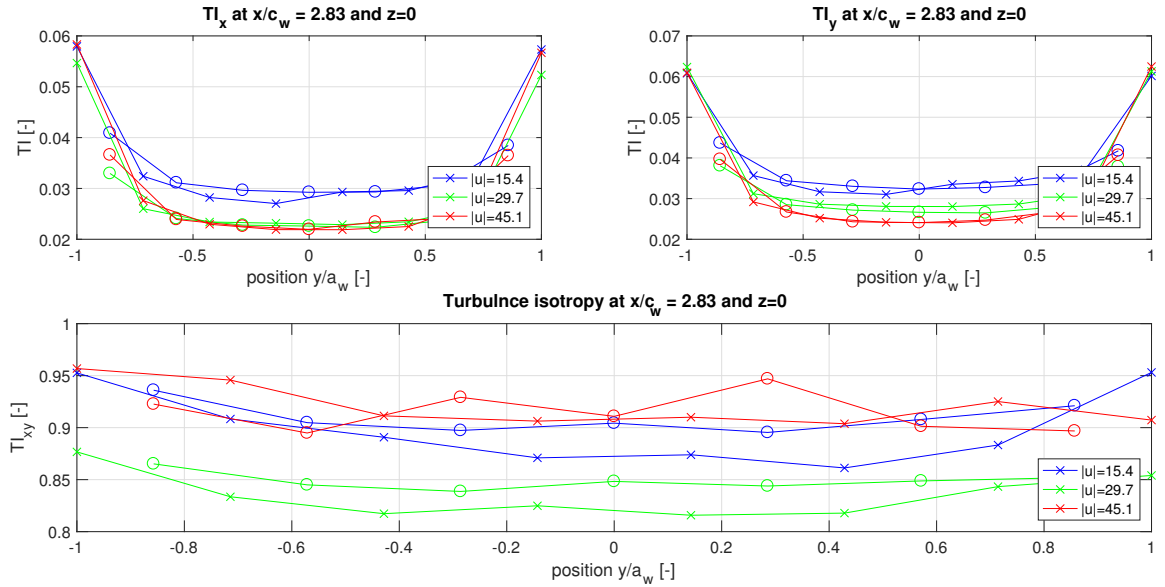


Figure D.4: Top: Turbulence intensities in  $x$ - and  $y$ -directions. Bottom: Turbulence isotropy parameter. Results for the plane behind the airfoils.

## Results Grid 1 (2x2): $x/c_w = -0.5$

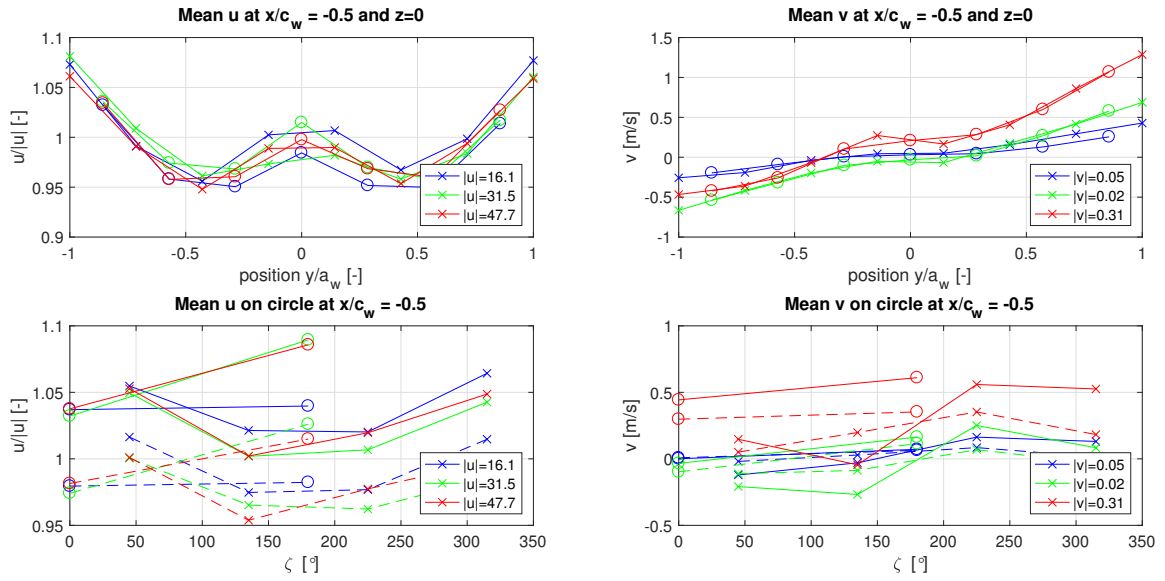


Figure D.5: Normalized flow velocity for the  $x$ - and  $y$ -directions in the plane located at the leading edge of the airfoils.

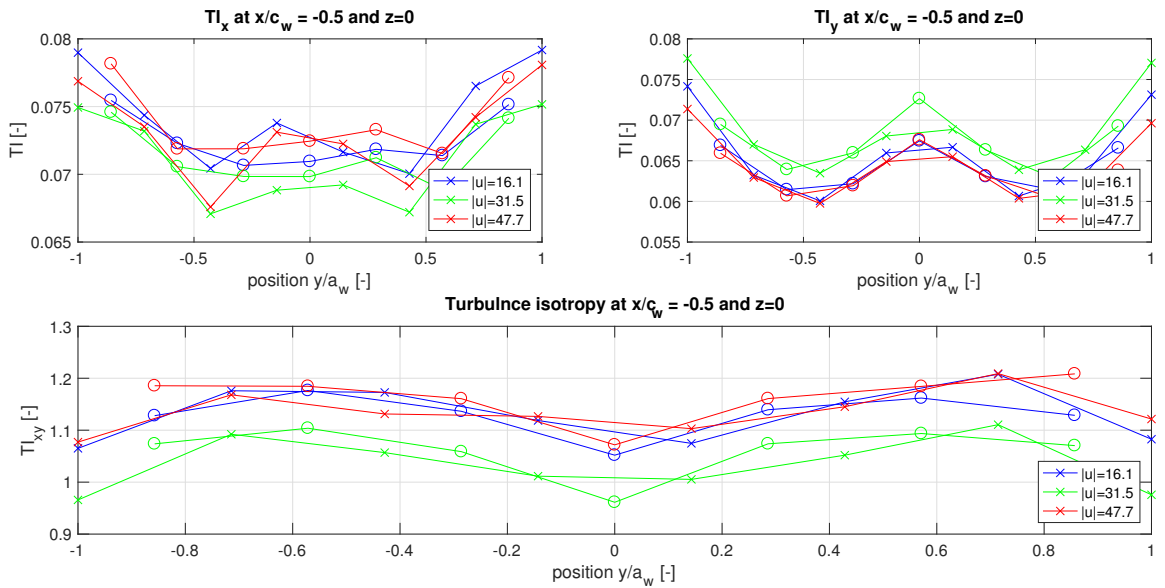


Figure D.6: Top: Turbulence intensities in  $x$ - and  $y$ -directions. Bottom: Turbulence isotropy parameter. Results for the plane at the airfoils leading edge.

## Results Grid 1 (2x2): $x/c_w = 2.833$

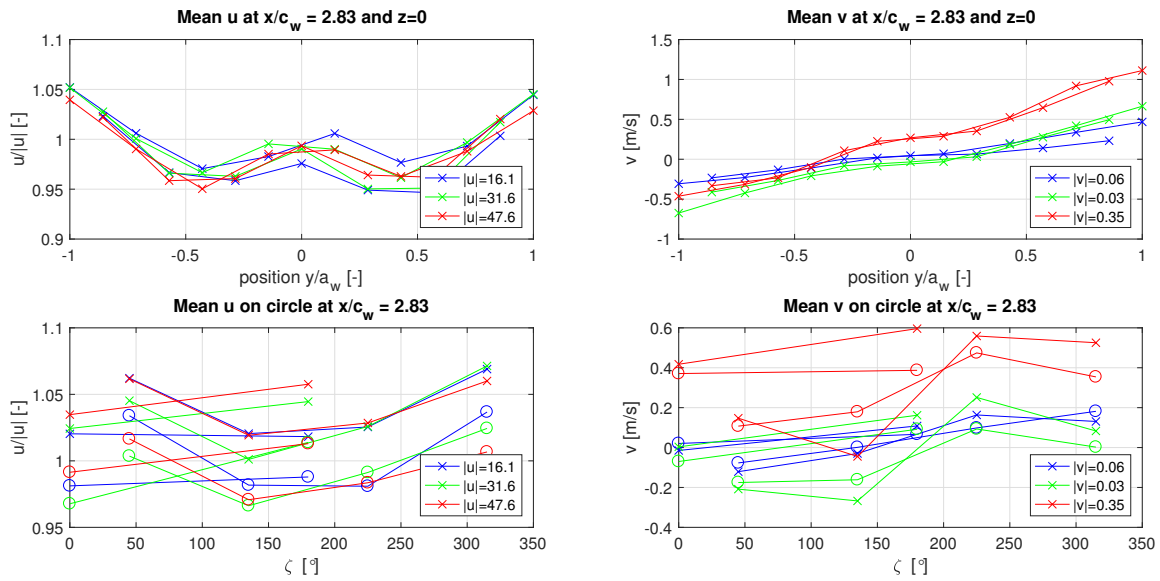


Figure D.7: Normalized flow velocity for the  $x$ - and  $y$ -directions in the plane located behind the airfoil.

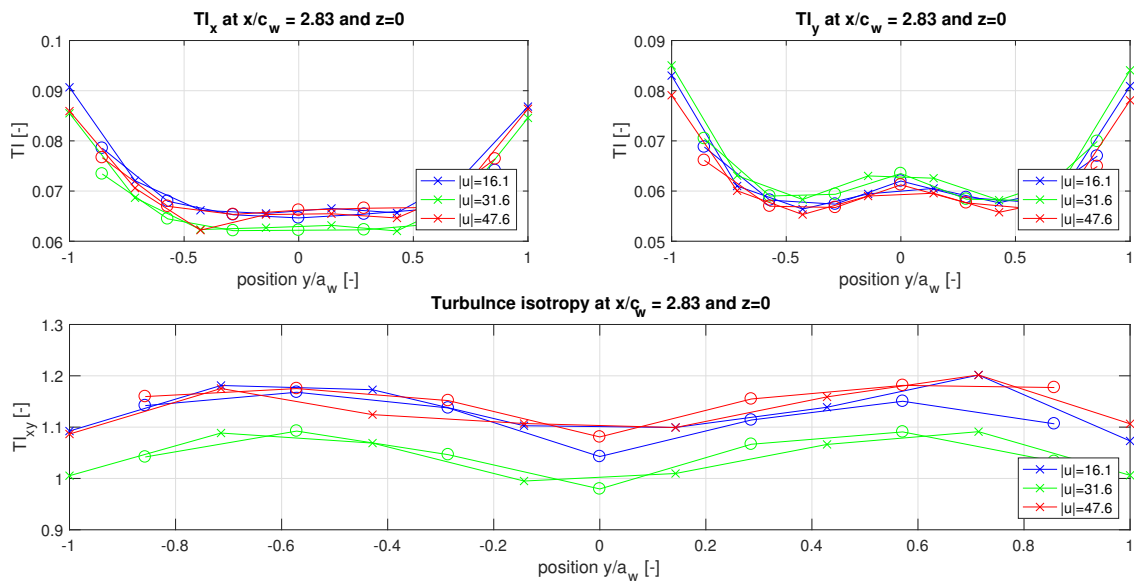


Figure D.8: Top: Turbulence intensities in  $x$ - and  $y$ -directions. Bottom: Turbulence isotropy parameter. Results for the plane behind the airfoils.

## Results Grid 2 (3x3): $x/c_w = -0.5$

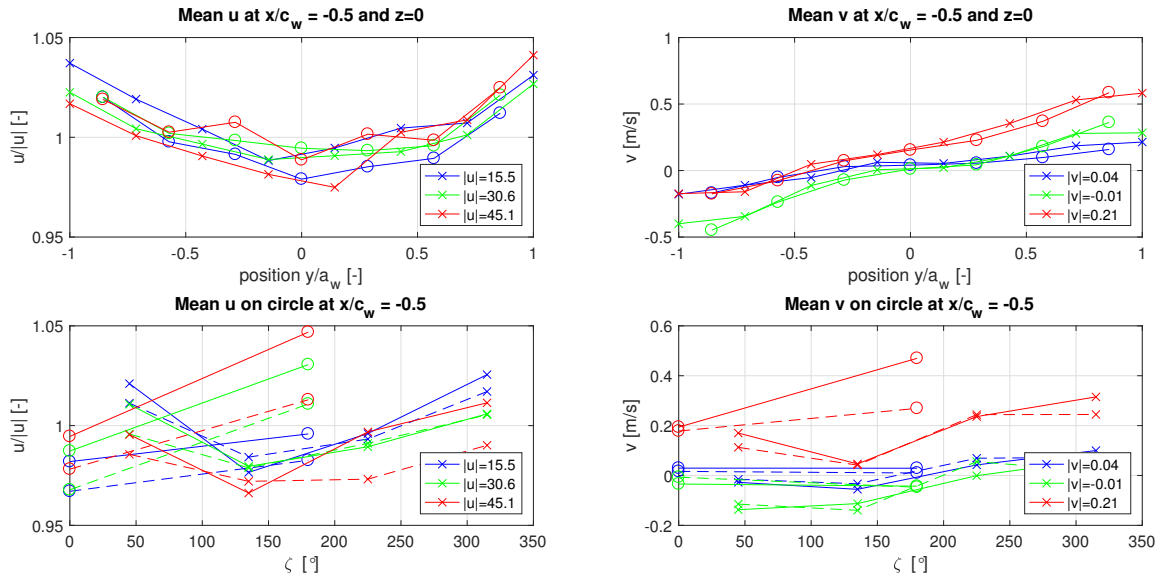


Figure D.9: Normalized flow velocity for the  $x$ - and  $y$ -directions in the plane located at the leading edge of the airfoils.

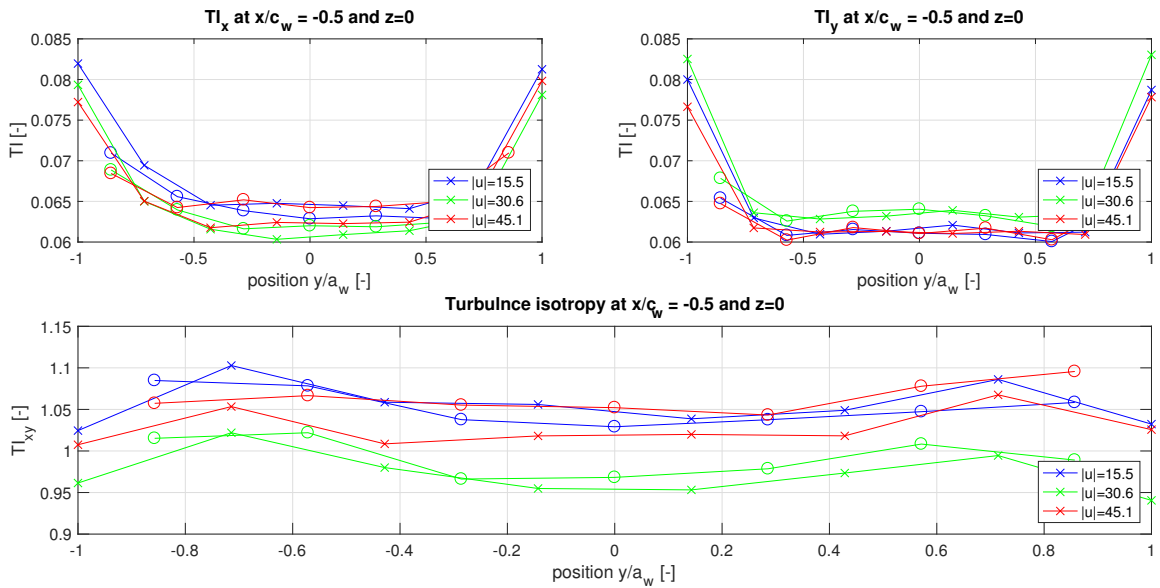


Figure D.10: Top: Turbulence intensities in  $x$ - and  $y$ -directions. Bottom: Turbulence isotropy parameter. Results for the plane at the airfoils leading edge.

## Results Grid 2 (3x3): $x/c_w = 2.833$

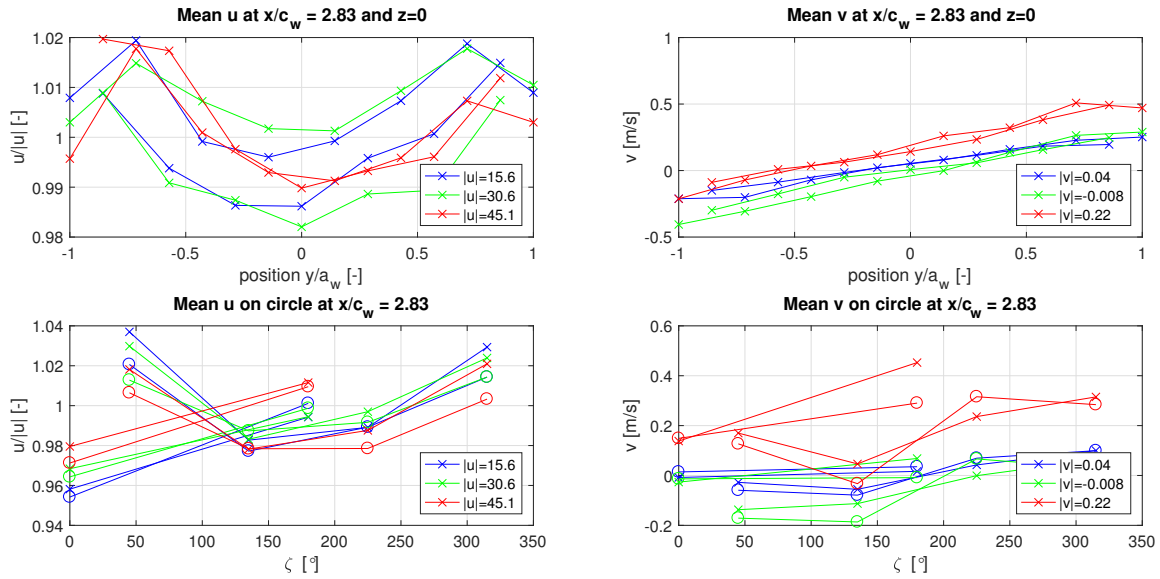


Figure D.11: Normalized flow velocity for the  $x$ - and  $y$ -directions in the plane located behind the airfoil.

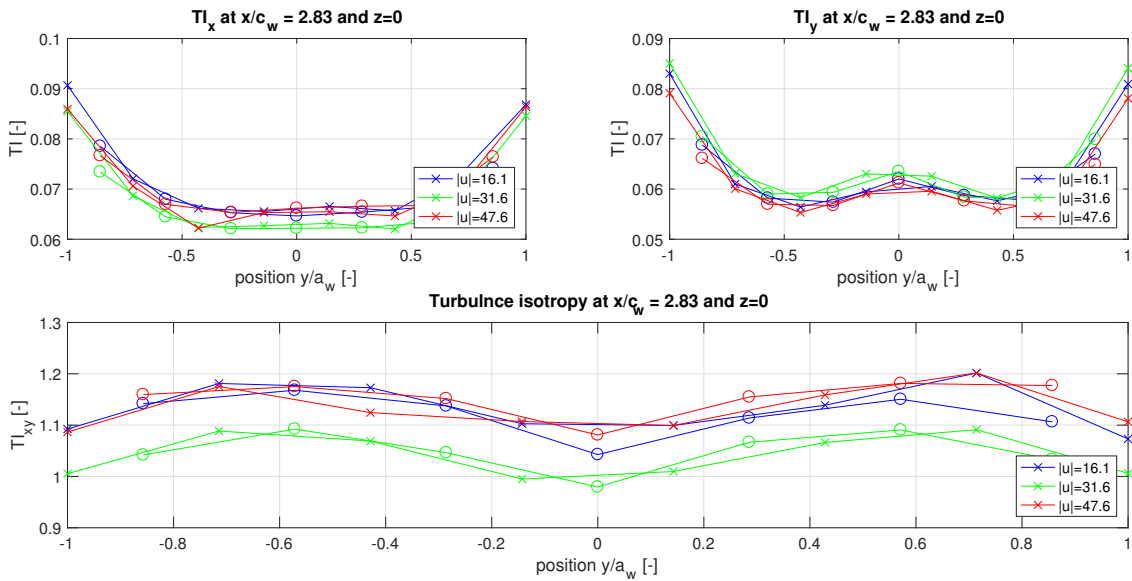


Figure D.12: Top: Turbulence intensities in  $x$ - and  $y$ -directions. Bottom: Turbulence isotropy parameter. Results for the plane behind the airfoils.

### Results Grid 3 (4x4): $x/c_w = -0.5$

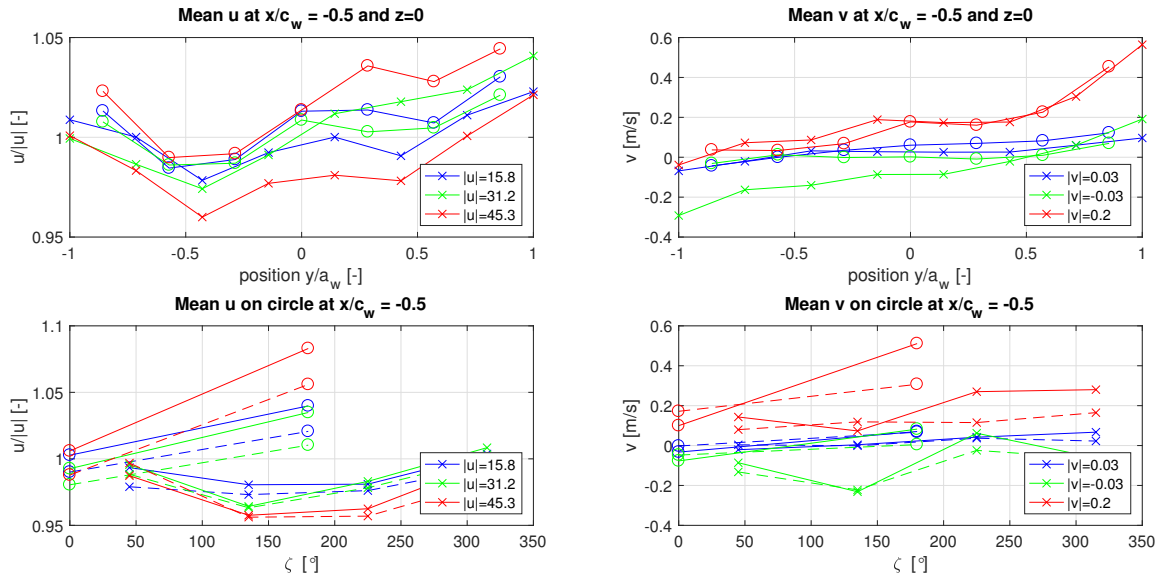


Figure D.13: Normalized flow velocity for the  $x$ - and  $y$ -directions in the plane located at the leading edge of the airfoils.

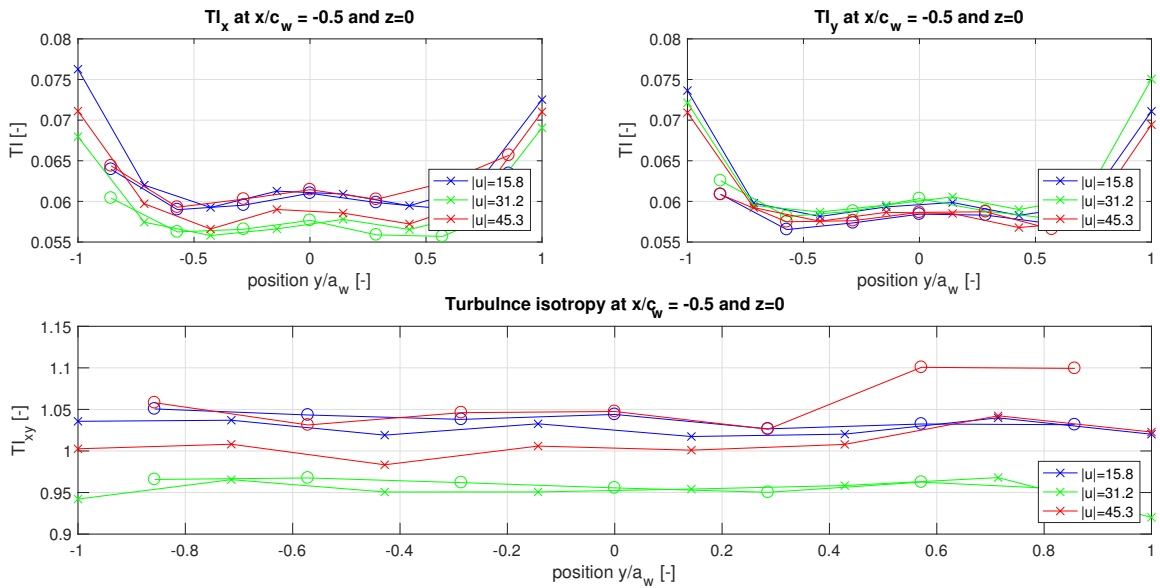


Figure D.14: Top: Turbulence intensities in  $x$ - and  $y$ -directions. Bottom: Turbulence isotropy parameter. Results for the plane at the airfoils leading edge.

### Results Grid 3 (4x4): $x/c_w = 2.833$

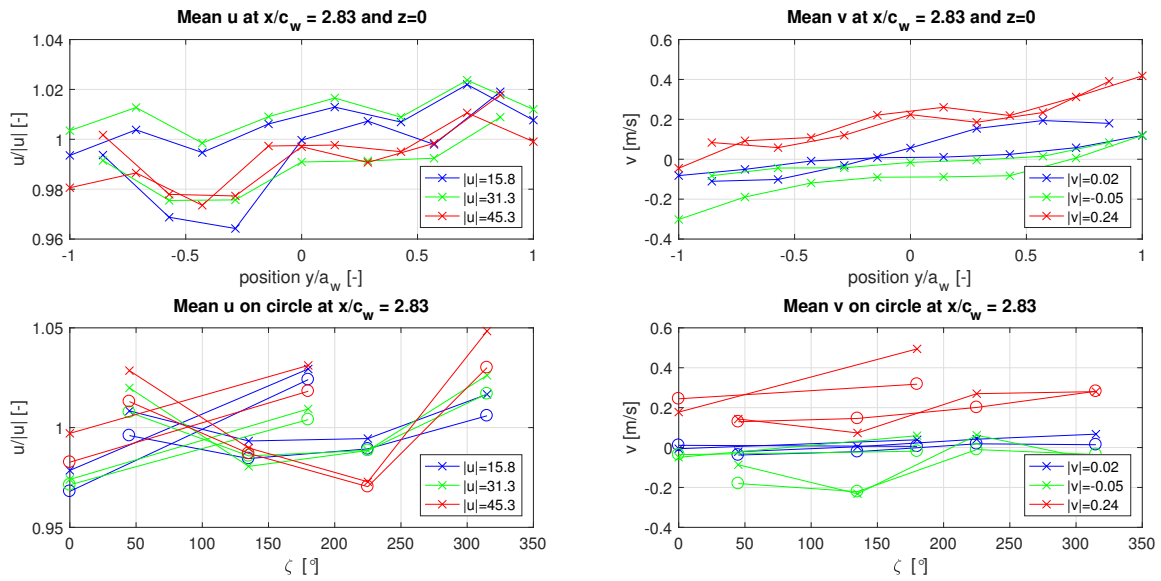


Figure D.15: Normalized flow velocity for the  $x$ - and  $y$ -directions in the plane located behind the airfoil.

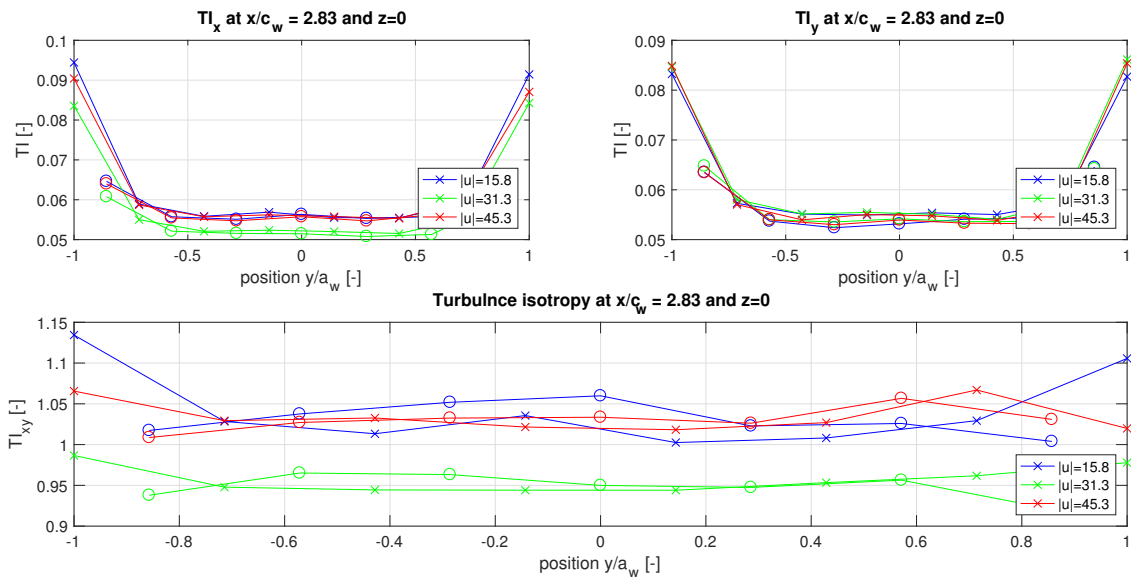


Figure D.16: Top: Turbulence intensities in  $x$ - and  $y$ -directions. Bottom: Turbulence isotropy parameter. Results for the plane behind the airfoils.

## D.2.2 Turbulence spectra

This section concerns the turbulence spectra measured at positions along the leading edge of the wing profiles. In the intensive (longer duration) CTA measurements performed the flow is examined along horizontal positions along the flat plate wing and in several stations for the circular wings.

The hot-wire data contained non-natural intensity swings in the high frequency domain. It was attempted to combat this during the measurements by maximizing the response time of the system using amplifier-gain and -filter settings and checking the square-wave response function. However it was impossible to obtain a response time higher than 10kHz without introducing constant high frequency oscillations. If the high frequency intensity swings are left uncontrolled it resulted in poorly converging results for the integral length scale which is highly undesirable. Therefore a digital low-pass filter was also implemented at 10kHz, 16kHz, and 24kHz for the respective free stream velocities: 15, 30, and 45  $m/s$ , unfortunately not allowing us to determine the Kolmogorov length scale from the data.

**Grid 1 (2x2):**  $x/c_w = -0.5$

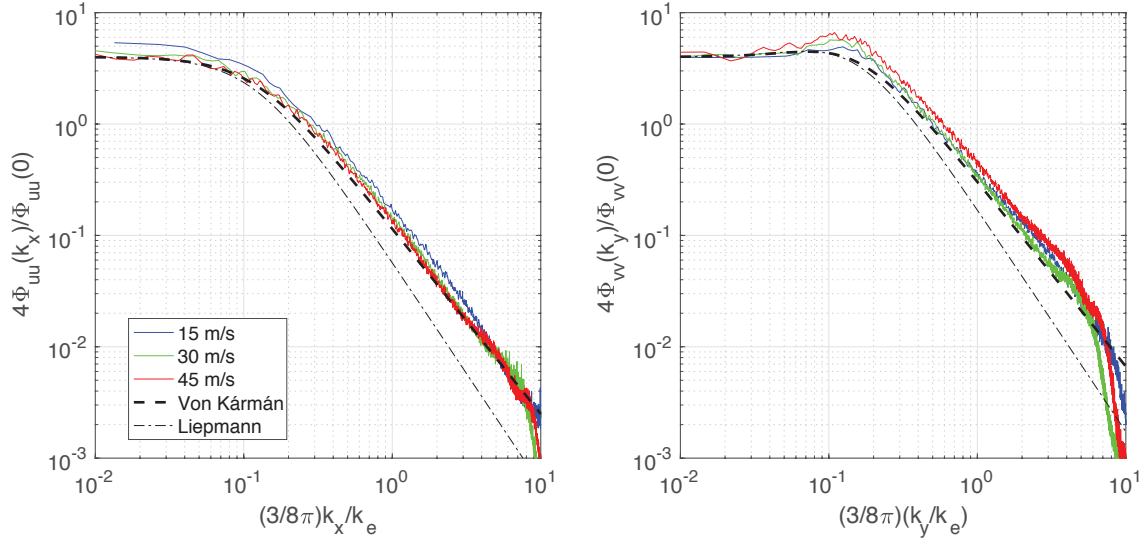


Figure D.17: Normalized turbulence spectrum for turbulence grid 1 (2x2) at the three measurement velocities of 15, 30, and 45  $m/s$ .

**Grid 2 (3x3):**  $x/c_w = -0.5$

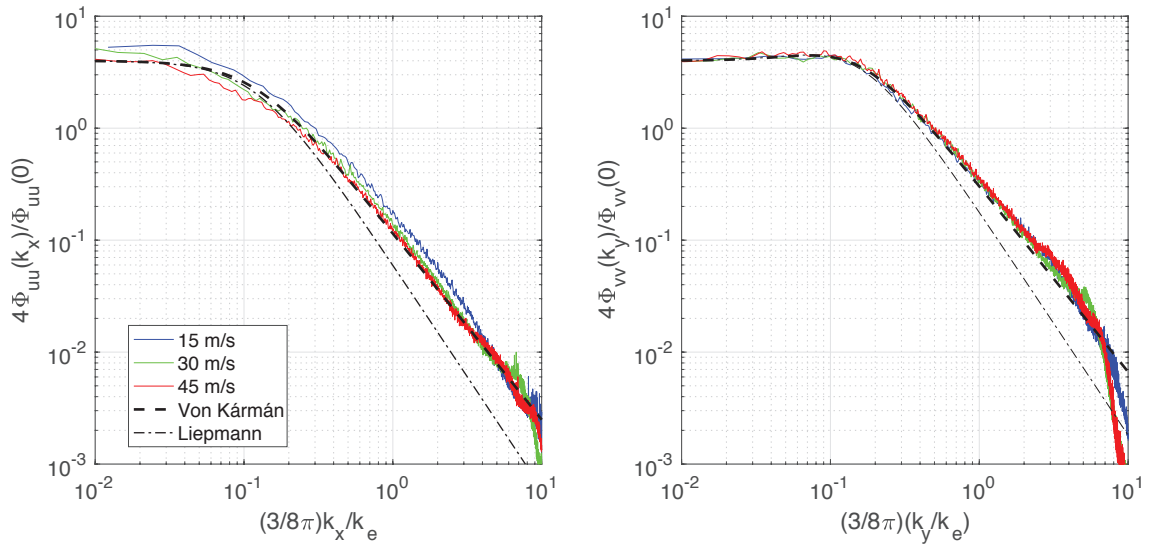


Figure D.18: Normalized turbulence spectrum for turbulence grid 2 (3x3) at the three measurement velocities of 15, 30, and 45  $m/s$ .

**Grid 3 (4x4):**  $x/c_w = -0.5$

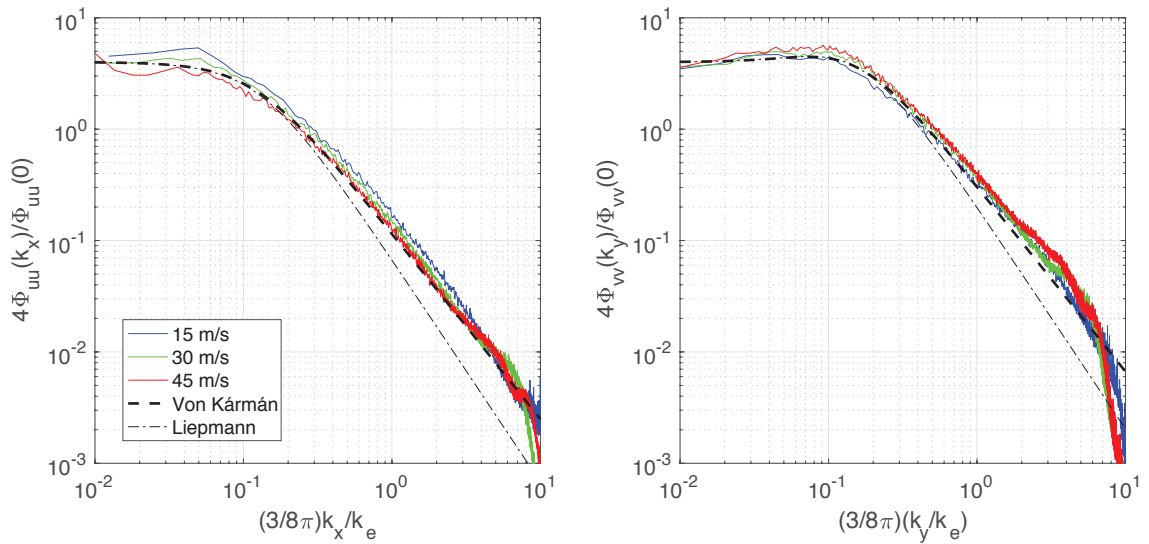


Figure D.19: Normalized turbulence spectrum for turbulence grid 3 (4x4) at the three measurement velocities of 15, 30, and 45  $m/s$ .

### D.2.3 Turbulence length scales

Results Grid 1 (2x2):  $x/c_w = -0.5$

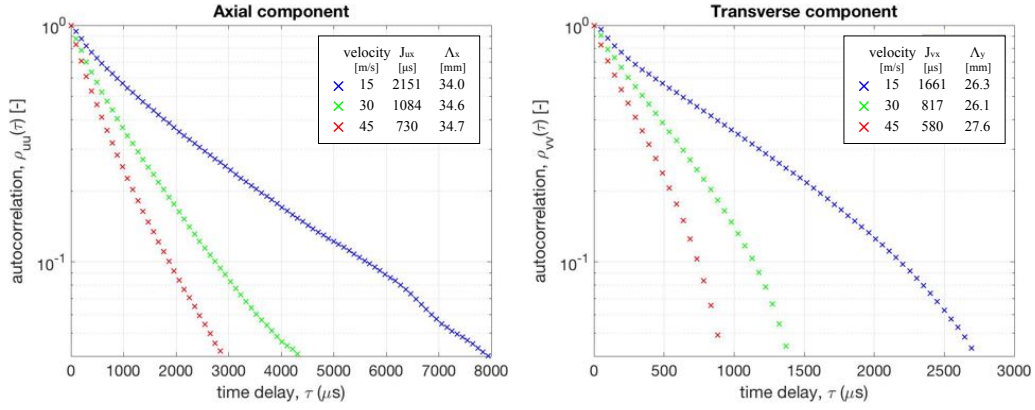


Figure D.20: Turbulence autocorrelations in both axial and transversal directions. Axial: one in ten data points is plotted. Transversal: one in five is shown.

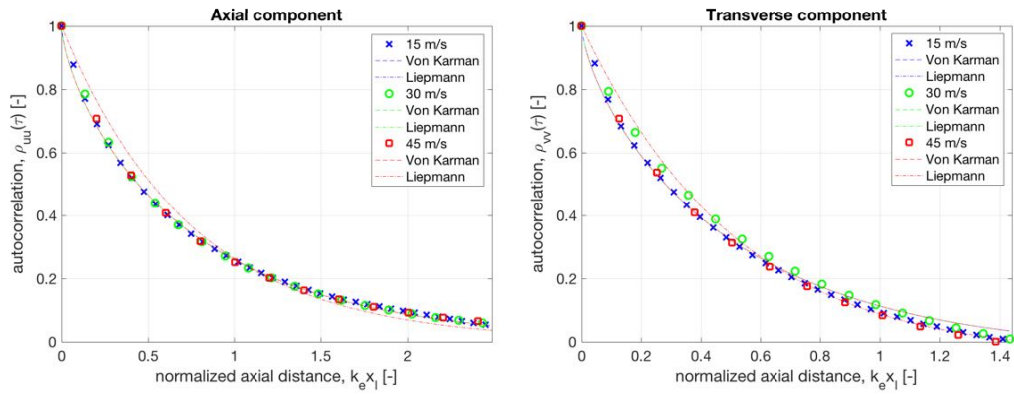


Figure D.21: Axial and transverse autocorrelation measurement data fitted according to Kármán and Liepmann correlations.

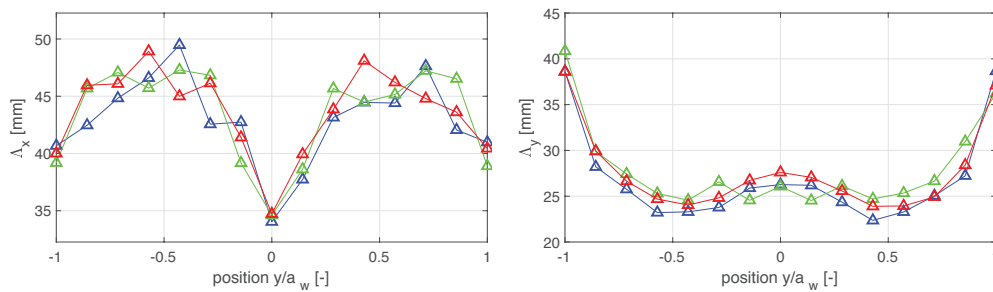


Figure D.22: Integral length scale results plotted for positions along the airfoils leading edge. Results obtained using the von Kármán model.

## Results Grid 2 (3x3): $x/c_w = -0.5$

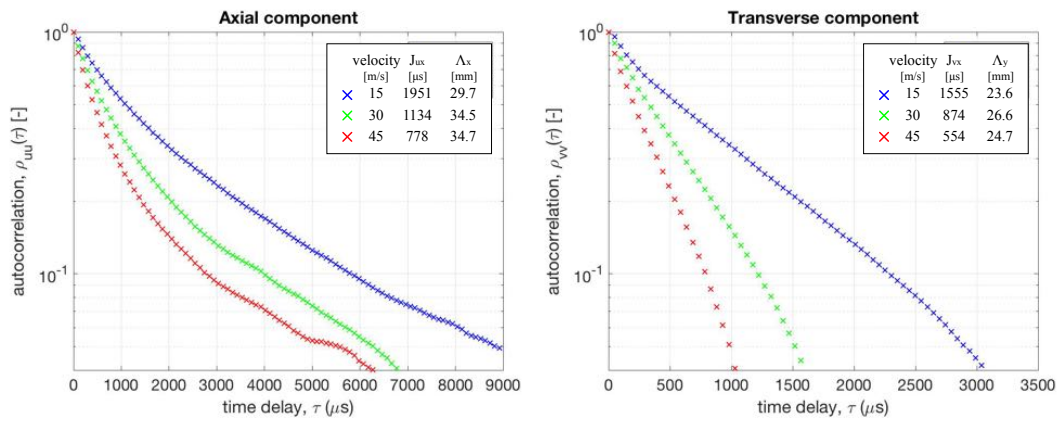


Figure D.23: Normalized flow velocity for the  $x$ - and  $y$ -directions in the plane located behind the airfoil.

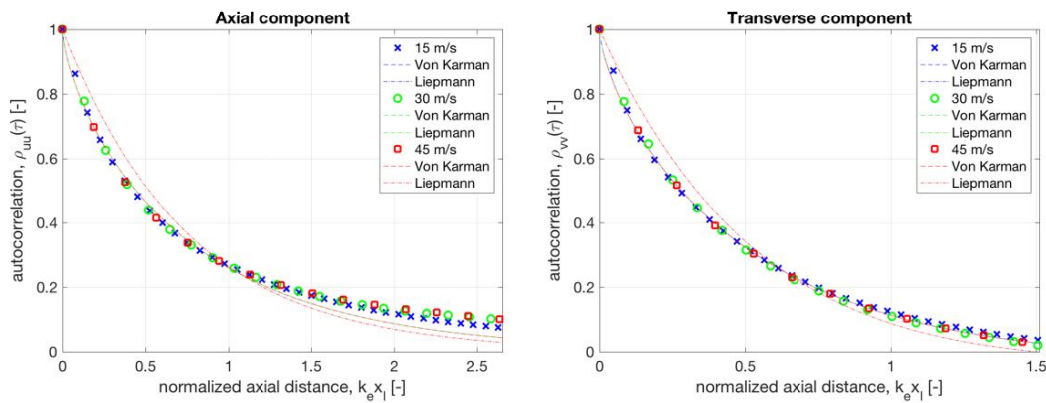


Figure D.24: Axial and transverse autocorrelation measurement data fitted according to von Kármán and Liepmann correlations.

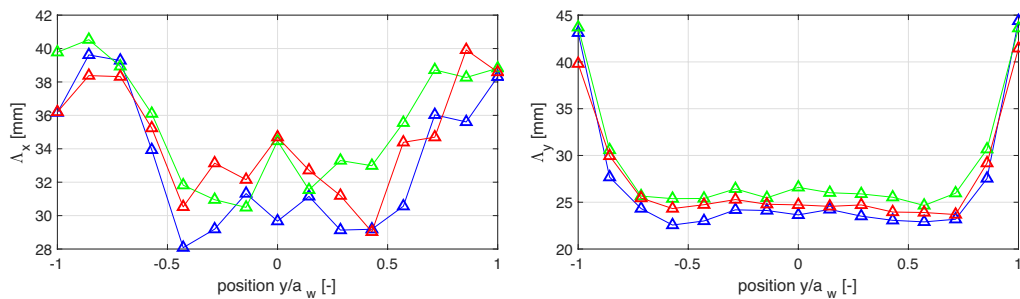


Figure D.25: Integral length scale results plotted for positions along the airfoils leading edge. Results obtained using the von Kármán model.

## Results Grid 3 (4x4): $x/c_w = -0.5$

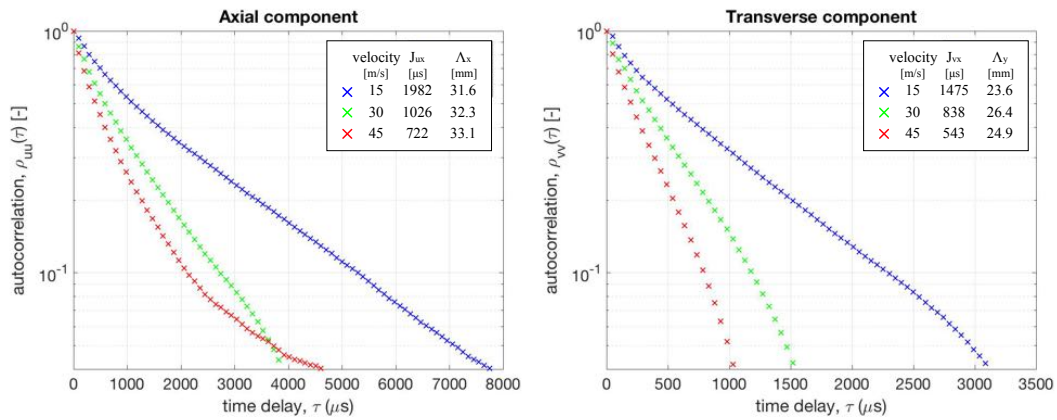


Figure D.26: Normalized flow velocity for the  $x$ - and  $y$ -directions in the plane located behind the airfoil.

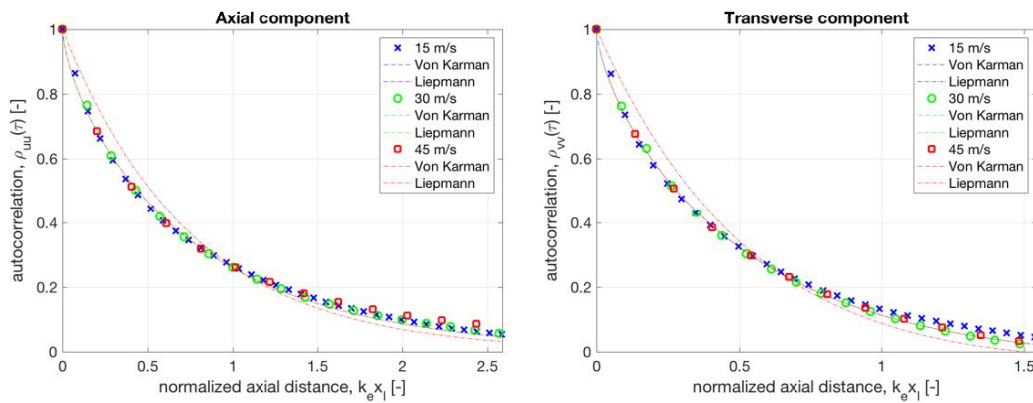


Figure D.27: Axial and transverse autocorrelation measurement data fitted according to von Karman and Liepmann correlations.

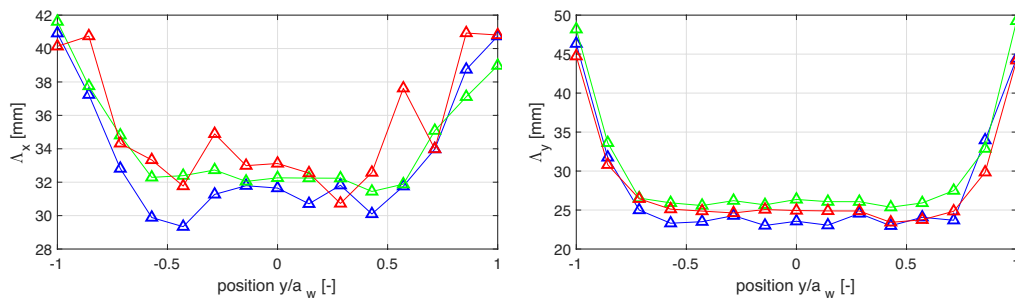


Figure D.28: Integral length scale results plotted for positions along the airfoils leading edge. Results obtained using the von Kármán model.

# Bibliography

- [1] R.K. Amiet. Compressibility effects in unsteady thin-airfoil theory. *AIAA Journal*, 12(2):252–255, 1974.
- [2] R.K. Amiet. Acoustic radiation from an airfoil in a turbulent stream. *Journal of Sound and vibration*, 41(4):407–420, 1975.
- [3] R.K. Amiet. High frequency thin-airfoil theory for subsonic flow. *AIAA journal*, 14(8):1076–1082, 1976.
- [4] T. Aufderheide, C. Bode, J. Friedrichs, and C. Kožulović. The generation of higher levels of turbulence in a low-speed cascade wind tunnel by pressurized tubes. July 2014.
- [5] A.B. Basset. *Treatise on Hydrodynamics*, volume vol. II. Bell & Co, London: Deighton, 1888.
- [6] H.H. Bruun. *Hot-wire anemometry: principles and signal analysis*. Oxford science publications, 1st edition edition, June 1995.
- [7] B.-T. Chu and L. S. G. Kovásznyai. Non-linear interactions in a viscous heat-conducting compressible gas. *Journal of Fluid Mechanics*, 3-5:494–514, 1957.
- [8] G. Comte-Bellot and S. Corrsin. The use of a contraction to improve the isotropy of rid-generated turbulence. *Journal of Fluid Mechanics*, 25(4):657–682, 1966.
- [9] G. Comte-Bellot and S. Corrsin. Simple eulerian time correlation of full-and narrow-band velocity signals in grid-generated, isotropic turbulence. *Journal of Fluid Mechanics*, 48(02):273–337, 1971.
- [10] N. Curle. The influence of solid boundaries upon aerodynamic sound. In *Proceedings of the Royal Society of London A: Mathematical, Physical and Engineering Sciences*, volume 231, pages 505–514. The Royal Society, 1955.
- [11] L. D. de Santana. *Semi-analytical methodologies for airfoil noise prediction*. PhD thesis, von Karman Institute for Fluid Dynamics, 2015.
- [12] U. Fey, M. König, and H. Eckelmann. A new strouhal-reynolds-number relationship for the circular cylinder in the range  $47 < re < 2 \cdot 10^5$ . *Physics of Fluids*, 10:1547–1549, July 1998.
- [13] M. Gad-el Hak and S. Corrsin. Measurements of the nearly isotropic turbulence behind a uniform jet grid. *Journal of Fluid Mechanics*, 62(1):115–143, 1973.

- [14] J.O. Hinze. *Turbulence*. Mcgraw-Hill College, 2nd edition edition, May 1975.
- [15] J.V. Larssen. *Large scale homogeneous turbulence and interactions with flat-plate cascade*. PhD thesis, Virginia Polytechnic Institute and State University, January 2005.
- [16] A. Melling. Tracer particles and seeding for particle image velocimetry. *Measurement Science and Technology*, 8(12):1406, 1997.
- [17] R. W. Paterson and R.K. Amiet. Acoustic radiation and surface pressure characteristics of an airfoil due to incident turbulence.
- [18] S.B. Pope. *Turbulent flows*. Cambridge University Press, 1st edition edition, August 2000.
- [19] M. Raffel, C.E. Willert, S.T. Wereley, and J. Kompenhans. *Particle Image Velocimetry - a practical guide*. Springer, 2nd edition edition, 2007.
- [20] S.W. Rienstra and A. Hirschberg. An introduction to acoustics. *Eindhoven University of Technology*, 18:19, 2003.
- [21] P.E. Roach. The generation of nearly isotropic turbulence by means of grids. *International journal of heat and fluid flow*, 8(2):82–92, June 1987.
- [22] M. Roger. On broadband jet–ring interaction noise and aerofoil turbulence–interaction noise predictions. *Journal of Fluid Mechanics*, 653:337–364, 2010.
- [23] K. Schwarzschild. Die beugung und polarisation des lichts durch einen spalt. i. *Mathematische Annalen*, 55(2):177–247, 1901.
- [24] M.J. Sytsma and L. Ukeiley. Wind tunnel generated turbulence. <http://enu.kz/repository/2011/AIAA-2011-1159.pdf>, Januari 2011.

